Finding the Optimal Detector for Linear Quantum Measurements

By

Joe Bentley

A thesis submitted to
the University of Birmingham
for the degree of
DOCTOR OF PHILOSOPHY

Institute for Gravitational Wave Astronomy
School of Physics and Astronomy
College of Engineering and Physical Sciences
University of Birmingham
April 2021

ABSTRACT

Our knowledge of Physics is fundamentally bound by the sensitivity of our detectors to the quantity that we are attempting to measure. For current and future gravitational wave detectors we are now predominantly limited by the Quantum noise, which is due to the fundamental Quantum fluctuations of the vacuum. This hinders our detection of gravitational waves from high-frequency astronomical sources such as neutron star mergers, while also impacting proposed searches for new physics such as axion detection and Quantum gravity experiments. Many techniques have been introduced for reducing the effect of the Quantum noise such as negative dispersion, variational readout, and frequency-dependent squeezing. However, from the outset all of these techniques are inferred via a process of trial and error combined with prior experience, and also often only target specific frequency regimes. Therefore it is not obvious how to systematically engineer a specific desired response for a detector without a large amount of unguided research and development. However, using new techniques for the network synthesis of quantum systems from the quantum control community, I show how it is possible to reproduce a desired quantum filter. This is then used to develop a totally new framework for designing optimal detectors that saturate the Heisenberg limit, culminating in a general and intuitive approach to developing new breakthroughs in detector design. This approach then leads to the proposal of an all-optical PT symmetric amplifier, which is both stable and has infinite DC response.

ACKNOWLEDGMENTS

First and foremost, I would like to thank my wife Chloé Marie Taylor, who has been an incredible support along this entire journey. There has not been a moment where she has been impatient and she has always been there for me. I also thank both my parents, Vina Eyre and Ron Bentley, who have believed in me for my entire life, and have given me tremendous love and freedom. Finally, I am so grateful for my grandma and granddad, who have inspired me so much in my life and have always been there to bring joy to my life.

I will also give my incredible thanks to my supervisor Haixing Miao, who has not only shaped my career and been an excellent continuous help in my work, but has also been an incredible emotional support for the more difficult times during this project. He has been an excellent role-model to aspire to.

I will also give my thanks to other staff members of our experimental group: Denis Martynov, Conor Mow-Lowry, and Andreas Freise, who provided an excellent and wide-ranging knowledge basis of the gravitational wave instrumentation community.

Next I would like to thank all of my fellow ifolab PhD students and postdocs: Amit Ubhi, George Smetana, Chiara Di Fronzo, Phil Jones, Sam Rowlinson, Sam Cooper, Aaron Jones; and Artemiy Dmitriev, Leonid Prokhorov, and Kazuhiro Agatsuma, who have all provided a great environment for open research and development, as well as a huge amount of enthusiasm.

Also I will thank David Stops for being indispensable in helping with technical issues, and Jo Cox for sorting out many of my administrative troubles.

Finally, I would like to thank our pet bunnies, Simba and Chai for lending their peaceful, calming energy to our house and infusing our lives with innocent joy.

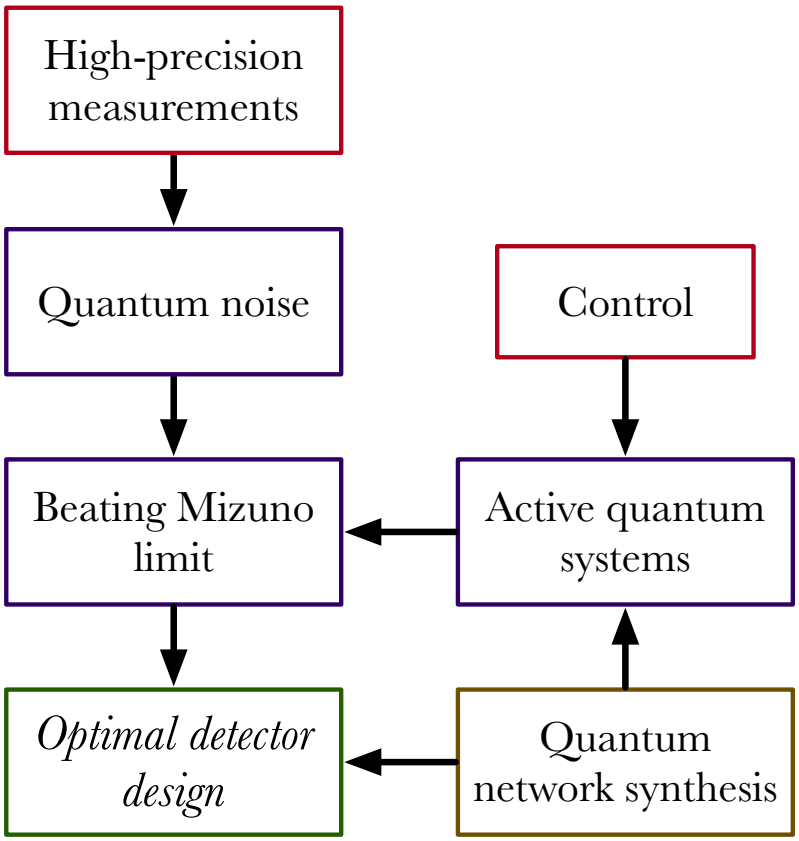
High-precision measurements
Quantum noise
Control
Beating Mizuno limit
Active quantum systems
Optimal detector design
Quantum network synthesis

List of Papers

The following first author papers are incorporated into this thesis:

- J. Bentley, P. Jones, D. Martynov, A. Freise, and H. Miao. Converting the signal-recycling cavity into an unstable optomechanical filter to enhance the detection bandwidth of gravitational-wave detectors. *Phys. Rev. D* 99, 102001 (2019)
  Used in Chapter. 3.

- J. Bentley, H. Nurdin, Y. Chen, and H. Miao. Direct approach to realizing quantum filters for high-precision measurements. *Phys. Rev. A* 103, 013707 (2021)
  Used in Chapter. 5.

- J. Bentley, H. Nurdin, X. Li, Y. Chen, and H. Miao. Designing Heisenberg-limited linear detectors—a bottom-up approach. (In preparation)
  Used in Chapters. 6 and 7.

- J. Bentley, X. Li, M. Korobko, R. Schnabel, Y. Chen, and H. Miao. An all-optical PT-symmetric amplifier. (In preparation)
  Used in Chapter. 8.

The following papers on which I am an author are not included in this thesis:

- X. Li, J. Smetana, A. Ubhi, J. Bentley, Y. Chen, Y. Ma, H. Miao, and D. Martynov. Enhancing interferometer sensitivity without sacrificing bandwidth and stability: beyond single-mode and resolved-sideband approximation. (In preparation)

- T. Zhang, J. Bentley, and H. Miao. A Broadband Signal Recycling Scheme for Approaching the Quantum Limit from Optical Losses. *Galaxies 2021*, 9(1), 3 (2020)

- T. Zhang, J. Smetana, Y. Chen, J. Bentley, D. Martynov, H. Miao, W. E. East, and H. Yang. Toward observing neutron star collapse with gravitational wave detectors. *Phys. Rev. D* 103, 044063 (2021)

Table of Contents

Notations

Notation/Phrase	**Meaning**
$f(\omega) = \int_{-\infty}^{+\infty} dt\, e^{i\omega t} f(t)$	Fourier transform
$f(t) = \frac{1}{2\pi} \int_{-\infty}^{+\infty} d\omega\, e^{-i\omega t} f(\omega)$	Inverse Fourier transform
$f(s) = \int_{0^-}^{+\infty} dt\, e^{st} f(t)$	Laplace transform
$\frac{dA(t)}{dt} = \frac{i}{\hbar}[H, A(t)]$	Heisenberg equation of motion
A^T	Matrix transpose
$A^\dagger$	Conjugate transpose or adjoint
$A^\#$	Element-wise complex conjugate or adjoint (no transpose)
ω_0	Laser carrier frequency
Ω	Gravitational wave sideband frequency
$S_{FF}(\Omega)$	Double-sided power spectral density

Chapter One

Introduction

Incredibly, we have arrived at a moment where the most limiting form of noise in high-precision measurements is the quantum noise, i.e. the fundamental fluctuations of the quantum vacuum. As we can see in Figure. 1.1, it is the highest broadband noise source in current-generation advanced gravitational-wave detectors, limiting the detection of high-frequency sources such as binary neutron star mergers and pulsars. It is also a limiting noise factor in searches for new physics using interferometers [1, 2].

The root of the quantum noise is the Heisenberg uncertainty principle which states that two incompatible (i.e. non-commuting) observables cannot be measured simultaneously. This leads intuitively to a non-zero minimum energy for a harmonic oscillator. Consider a particle in a known harmonic potential. Since Heisenberg tells us that we cannot simultaneously know both its momentum and position precisely, the particle *cannot stop moving* as then we could deduce both its momentum and position, so therefore there exists is a non-zero minimum energy for the particle. Since the particle is confined in space, i.e. its position wavefunction goes to zero at infinity, it can only take

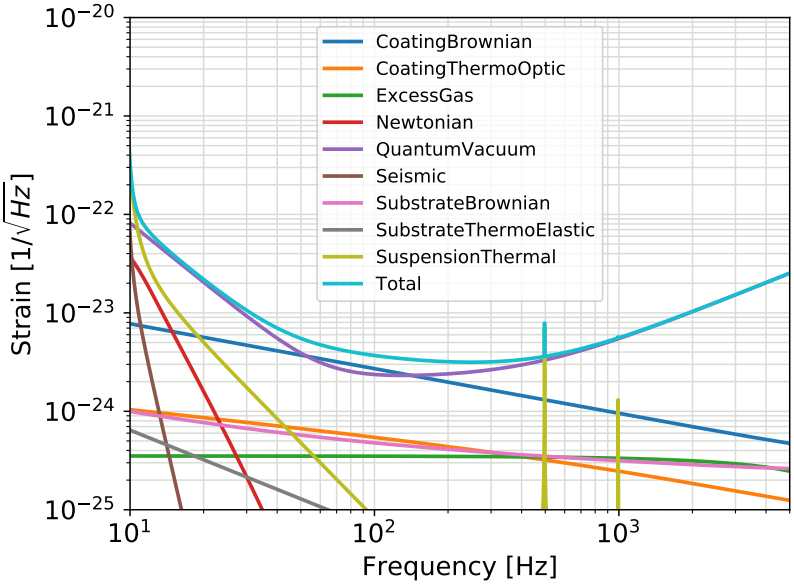

Figure 1.1 The theoretical noise budget for advanced LIGO [3] showing both classical and quantum noise sources. At frequencies above $\sim 100\,\mathrm{Hz}$ the sensitivity is limited entirely by the quantum shot noise.

certain discrete energies, with each unit of energy being called a "quanta". If we de-dimensionalise the position and momentum via $\hat{x} \to \hat{x}\sqrt{\hbar/(2m\omega)}$ and $\hat{p} \to \hat{p}\sqrt{\hbar m\omega/2}$ where m is the particle mass and ω is the oscillator frequency, it can be shown that in this state of minimum energy—called the vacuum state, as it is devoid of quanta—the dimensionless position and momentum have equal variance. It turns out that each mode of the electro-magnetic field is exactly equivalent to a harmonic oscillator if we call the position the "electric field" and the momentum the "magnetic field". Therefore we see an intrinsic uncertainty in the vacuum electro-magnetic field arises known as the *quantum noise*, which is superimposed on all measurements and thus obscures the value of the signal we are interested in measuring. This effect is very tiny, how-

ever as shown in Figure. 1.1 the quantum noise is actually the most limiting noise source at high frequencies, greater than any classical source of noise. As we shall discuss in Section. 2.1 the electric and magnetic field can be written as real quadrature operators that describe the amplitude and phase fluctuations of the field respectively. In the context of high-precision measurements, particularly gravitational wave detectors, the phase quadrature uncertainty manifests at the output as *shot noise*, while the amplitude quadrature uncertainty pushes the suspended optics with a stochastic force which couples back into the measurement output, a process called *measurement back-action*.

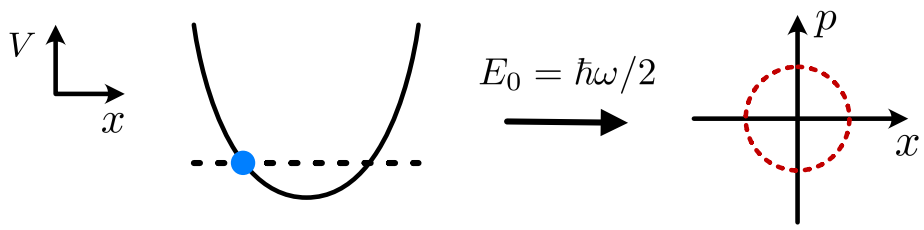

Figure 1.2 A particle in a harmonic potential $V(x)$ cannot have zero kinetic energy as then both its position and momentum would be known precisely. The minimum energy is given by $\frac{1}{2}\hbar\omega$, which is the eigenvalue of the energy eigenstate known as the vacuum state. The right-hand plot shows an equiprobability contour of the phase-space joint quasi-probability distribution $W(x, p)$ known as the Wigner function. In this case the Wigner function is a 2-D Gaussian distribution and so the variances are equal $\Delta x = \Delta p$.

In recent years there have been massive theoretical and experimental efforts to reduce the impact of quantum noise on high-precision measurements, owing to the extreme sensitivities reached by modern advanced gravitational-wave detectors. One of the most important milestones was Kimble's paper detailing setups for converting gravitational wave detectors into quantum non-demolition

(QND) detectors [4]. In that paper various approaches were explored for surpassing the *standard quantum limit*—the quantum noise limit arising from the balance between the shot noise and measurement back-action—specifically by taking advantage of the ponderomotive squeezing of the output light to reduce the quantum noise over a broadband magnitude. Another technique which shall be a main focus throughout this thesis is to use an all-pass quantum filter exhibiting negative dispersion known as an "unstable filter" to directly broaden the detection bandwidth without sacrificing the peak sensitivity [5].

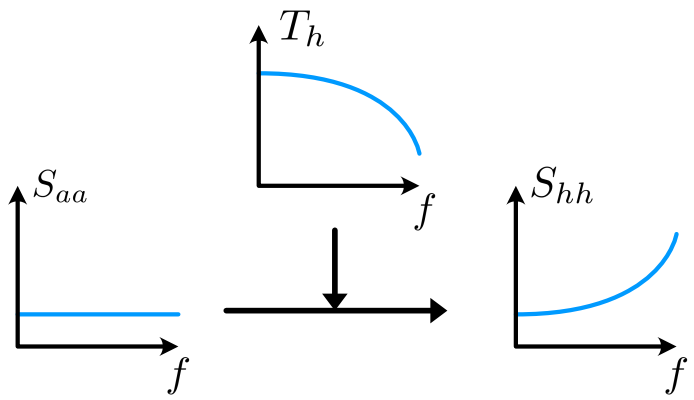

Figure 1.3 The shot noise spectrum at the input S_{aa} has a white-noise spectrum when the input port is in the vacuum state. Often the transfer function from the input to the output has a unity spectrum[1], and so the signal-referred spectrum S_{hh} is shaped only by the detector's signal response T_h. Therefore we are interested in how to shape the signal response of the detector.

Before we begin, let us make clear the problem we want to tackle. For measurements of high-frequency sources, such as binary neutron star (BNS)

[1]In the most general case it obeys Eq. (5.13), which means that the transfer function must have unity gain at all frequencies unless the state-space is augmented to add additional lossy noise channels.

mergers, we are entirely limited by the quantum shot noise [6, 7]. Therefore this will be our main focus and we will generally neglect consideration of the low-frequency radiation pressure noise. Equivalently, we can say that we are limited by the coupling of the signal to the output, since the quantum shot noise takes a flat white-noise spectrum at the input.[2] In general then, we are simply interested in the frequency response of the detector, and can equate quantum shot noise reduction to the design of quantum filters. So it is my aim in this work to deduce a general framework for the design of optimal quantum filters for high-precision measurements. The core is two important observations arising from the quantum control community. First, the observation that the conservation of the commutation relations among all modes of the system places a strong constraint on whether a quantum filter is realisable [8, 9], and if not whether any additional noise channels need to be added to make it so. Second, a method for realising an arbitrarily complicated physically realisable linear quantum system [10]. Combining these methods with the fundamental limit on the measurement of the signal, the quantum Cramér-Rao bound, we can directly infer the optimal detector for a given number of degrees of freedom.

The outline of this thesis is as follows. In Chapter. 2 I give an overview of the quantitative origins of quantum noise and the techniques used to analyse the frequency-domain behaviour of quantum systems throughout this work. In Chapter. 3 I then discuss the Mizuno limit, an important theorem limiting the total integrated sensitivity of resonant measurement devices. I then discuss

[2] In fact, as we shall discuss in Section. 6.2.2, the fundamental limiting factor is actually the fluctuations in the degree-of-freedom dispersively coupled to the signal of interest.

how bandwidth broadening techniques such as the unstable filter can be used to surpass this limit, giving an example of a new setup implementing bandwidth broadening known as the transmission-readout setup. In Chapter. 4 I briefly review the control theory ideas required throughout the thesis, discussing the use of local control and optimal combination to locally stabilise unstable degrees of freedom without sacrificing sensitivity after post-processing. In Chapter. 5 I introduce the general framework for realising physical quantum systems directly from their frequency-domain dynamics and show how it can be applied to high-precision measurements. The framework is demonstrated by creating an all-optical realisation of the aforementioned unstable filter as an example, reproducing the well-known internal squeezing setup. I then detail how the approach can be extended to n degrees of freedom. In Chapter. 6 I then discuss how this framework can be used to design optimal detectors via two approaches: first by designing coherent feedback filters for integration in currently existing setups, and secondly by designing entire detectors from the bottom up giving three instructive examples. In Chapter. 8 I introduce the PT-symmetric quantum amplifier and an all-optical realisation in a LIGO-like setup as well as a tabletop experiment proposal. Finally, in Chapter. 9 I discuss a software package I have created known as SImBA which allows the automatic application of the framework discussed previously, for example generating a graphical representation of the physical realisation from the transfer matrix.

Chapter Two

Analysing quantum noise

In this chapter we briefly discuss the methods used throughout this thesis for the analysis of quantum systems, specifically detailing the approach used for computing optical transfer functions based on the Heisenberg equations of motion of the system. First, we start with a brief quantitive overview of the origins of quantum noise, and then we construct the Hamiltonian for a tuned cavity with an open port and suspended mass and show how the equations of motions and thus the transfer functions can be derived.

2.1 Fundamental fluctuations of the quantum vacuum

The starting point of quantum optics is the quantisation of the freely propagating electromagnetic field Hamiltonian density in terms of a continuum of independent quantum harmonic oscillators modes [11, 12]. Instead of focussing on the free-space continuum modes we will restrict ourselves to the much sim-

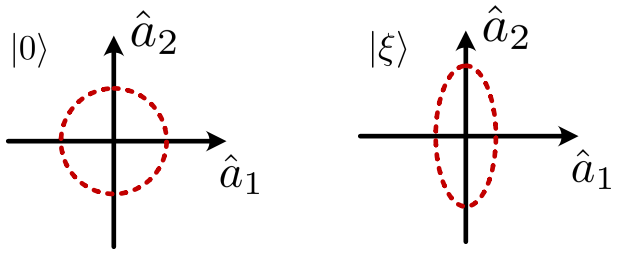

Figure 2.1 Noise ellipses (equiprobability contours) for the vacuum state and amplitude squeezed state. The latter has a reduced variance in the amplitude quadrature, and so an increased variance in the phase quadrature.

pler case of cavity eigenmodes with discrete spectra, later bringing back the continuum modes via the Langevin equation. Annihilation and creation of quanta in a single mode is performed by the operators $\hat{a}$ and $\hat{a}^\dagger$ respectively, with commutator $[\hat{a}, \hat{a}^\dagger] = 1$. Of course, since these operators are not Hermitian they cannot be observed. Instead we can observe Hermitian quadrature operators,

$$\hat{a}_1 = \frac{\hat{a} + \hat{a}^\dagger}{\sqrt{2}}, \quad \hat{a}_2 = \frac{\hat{a} - \hat{a}^\dagger}{\sqrt{2}i}, \tag{2.1}$$

called the amplitude and phase quadratures respectively, which correspond to the position and momentum of the harmonic oscillator mode. They can also be shown to correspond to amplitude and phase modulations of the electric field in the limit of high photon number [13]. The commutator is $[\hat{a}_1, \hat{a}_2] = i$ and so they are incompatible observables. In both the vacuum state $|0\rangle$ and

the coherent state $|\alpha\rangle$[1], both quadratures have equal variance,

$$(\Delta a_1)^2 = \frac{1}{2}, \quad (\Delta a_2)^2 = \frac{1}{2}, \tag{2.2}$$

and so are minimum uncertainty states since they satisfy,

$$(\Delta a_1)^2 (\Delta a_2)^2 \geq \frac{1}{4}, \tag{2.3}$$

with equality. States where $\Delta a_1 \neq \Delta a_2$, i.e. where $\hat{a}_1$ and $\hat{a}_2$ are correlated, are known as squeezed states.

Generally we work in the Heisenberg picture where the operators have time-dependance rather than the states as in the Schrödinger picture, however we factor out the fast oscillations of the field at the carrier frequency ω_0. Therefore we focus on the slowly varying amplitude $\hat{a}(\Omega)$ of the field at absolute frequency $\omega_0 + \Omega$.

The formulation of the coupling of the cavity mode $\hat{a}$ to an external input continuum mode $\hat{a}_{\text{in}}$ was first derived by Gardiner and Collett [15] and is given by the quantum Langevin equation,

$$\dot{\hat{a}}(t) = -\gamma \hat{a}(t) + \sqrt{2\gamma}\hat{a}_{\text{in}}(t), \tag{2.4}$$

where $\gamma = Tc/(4L)$ is the cavity bandwidth/decay rate where T is the mirror transmissivity and L is the cavity length. This is a quantum stochastic differential equation since $\hat{a}_{\text{in}}(t)$ is a stochastic variable. Such equations were developed rigorously by the formalism of quantum stochastic calculus [16].

[1]The coherent state $|\alpha\rangle$, also known as the displaced vacuum state, is the state most closely corresponding to a classical electric field, and is the state produced by a laser. In comparison the number state $|n\rangle$ is considered highly non-classical [14, Ch.15].

In this interpretation $\hat{a}_{\text{in}}$ is sourced by an external thermal heat bath with a continuous spectrum which determines the operator's statistics. Appendix. B considers a situation where this heat bath is not in a vacuum state but rather a finite temperature thermal state.

Taking the Fourier transform of Eq. (2.1) and noting that $\mathcal{F}\{f^\dagger(t)\} = f^\dagger(-\Omega)$ we find,

$$\hat{a}_1(\Omega) = \frac{\hat{a}(\Omega) + \hat{a}^\dagger(-\Omega)}{\sqrt{2}}, \quad \hat{a}_2(\Omega) = \frac{\hat{a}(\Omega) - \hat{a}^\dagger(-\Omega)}{\sqrt{2}i}, \tag{2.5}$$

and so in the frequency-domain the quadrature operators represent a mixture of the upper and lower sidebands $\omega_0 \pm \Omega$ about the carrier frequency ω_0.

2.2 Hamiltonian approach to computing optical transfer functions

In general we can use classical methods to analyse the quantum noise for a system. The reason for this is that for a quadratic Hamiltonian, after applying canonical quantisation by replacing the Poisson brackets with commutators, the Heisenberg equations of motion of the system are formally identical to the classical equations of motion. Therefore the classical field propagation formalism can still be used. However it is often easier to start with the Hamiltonian itself, directly calculating the Heisenberg-picture equations of motion from the Hamiltonian and then solving them in the frequency domain. In this formalism, each cavity is described by a single mode, a restriction known as the single-mode approximation. Here time delays are neglected, so that the phase

gained across the cavity is considered negligible. More specifically, for a cavity tuned to frequency ω_0, we consider only fields at frequencies $\omega_0 + \Omega$ where $\Omega \ll \mathrm{FSR}$ where $\mathrm{FSR} \equiv c/(2L)$ is the free spectral range of the cavity. In most cases we are interested in frequencies and lengths such that this approximation holds, however in future long-baseline interferometers this approximation must be lifted. Nevertheless, the analysis of many systems becomes more straightforward.

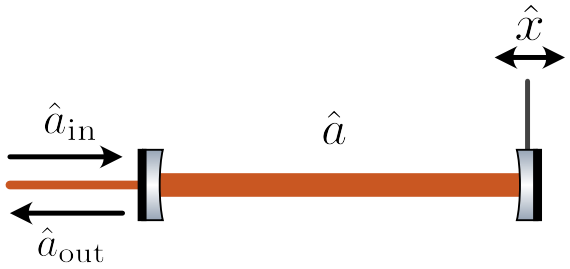

Figure 2.2 Diagram of a detuned cavity with a suspended end mirror as described by Eq. (2.6).

To achieve this, we follow the approach taken in [17], which we will summarise here. As an instructive example we consider a detuned cavity with a mechanically suspended end mirror, shown in Figure. 2.2. First we will consider the case where the input mirror is fully reflective, so there is no light entering the cavity. In this case both the cavity mode and the mirror mode can be quantised using discrete modes due to the boundary conditions of the cavity. Specifically we have the Hamiltonian,

$$\hat{H} = \hbar\omega_m \hat{b}^\dagger \hat{b} - F\hat{x} + \hbar\Delta \hat{a}^\dagger \hat{a} - \hbar\frac{\omega_0}{L}\hat{x}\hat{a}^\dagger \hat{a}, \tag{2.6}$$

which we have written in the rotating frame at a chosen laser carrier frequency

ω_0. Here F is some external classical force on the mirror, $\hat{x} = x_q(\hat{b}e^{-i\omega_m t} + \hat{b}^\dagger e^{i\omega_m t})$ is the mirror position where $x_q = \sqrt{\hbar/(2m\omega_m)}$ is the ground-state position uncertainty of the mirror and ω_m is the resonant frequency of the mirror, L is the length of the cavity, and finally Δ is the detuning of the cavity relative to the laser carrier frequency ω_0.

Note that the last term—the radiation pressure between the mirror and the cavity mode—leads to non-linear dynamics. To linearise the system we assume that there are a large number of photons inside the cavity and then let $\hat{a} \to \bar{a} + \delta\hat{a}$ where $\bar{a}^2$ is the mean number of photons (which we choose to be real and positive) and $\delta\hat{a}$ is some small fluctuation with zero mean. The mean photon number is related to the intracavity power P by $\bar{a} = \sqrt{2PL/(\hbar\omega_0 c)}$ where L is the cavity length. Substituting this in, we see that the mean part leads to a DC radiation pressure on the mirror which we assume is compensated, and the cross term between $\delta\hat{a}^\dagger\delta\hat{a}$ is taken to be negligible compared to the mean photon number. We also get an additional DC force $\hbar(\omega_0/L)\bar{a}^2\hat{x}$ which we can compensate experimentally and thus ignore. For convenience we then redefine $\hat{a}$ to be $\delta\hat{a}$ itself and obtain the linearised Hamiltonian,

$$\hat{H} = \hbar\omega_m\hat{b}^\dagger\hat{b} - F\hat{x} + \hbar\Delta\hat{a}^\dagger\hat{a} - \hbar\frac{\omega_0}{L}\hat{x}\bar{a}(\hat{a} + \hat{a}^\dagger). \tag{2.7}$$

Lifting the restriction that the input mirror is fully reflective so that freely propagating continuous light enters the cavity is difficult because it entails an overlap integral over an infinite number of continuous modes rather than the coupling of discrete oscillator modes. As shown in [18, 19, 11, 17], the result

is given by a Langevin equation and an input-output equation,

$$\dot{\hat{a}} = -\gamma\hat{a} + \sqrt{2\gamma}\hat{a}_{\text{in}} + \ldots, \quad \hat{a}_{\text{out}} = \hat{a}_{\text{in}} - \sqrt{2\gamma}\hat{a}, \tag{2.8}$$

where $\gamma \equiv Tc/(4L)$ is the cavity half-bandwidth where T is the input mirror power transmissivity, c is the speed of light, and L is the length of the cavity; $\hat{a}_{\text{in}}$ and $\hat{a}_{\text{out}}$ are the continuum fields entering and exiting the cavity respectively, and $\ldots$ are the other terms in the equation of motion for $\hat{a}$ generated by the Heisenberg equation of motion. These equations of motion are expressed in the Hamiltonian via the term,

$$-i\hbar\sqrt{\gamma}(\hat{a}\hat{c}^{\dagger}_{\text{ext}} - \hat{a}^{\dagger}\hat{c}_{\text{ext}}), \tag{2.9}$$

where $\hat{c}_{\text{ext}}(t = 0_{-}) \equiv \hat{a}_{\text{in}}$ and $\hat{c}_{\text{ext}}(t = 0_{+}) \equiv \hat{a}_{\text{out}}$.

Now looking at the last term in Eq. (2.7), we can again write the displacement $\hat{x}$ in terms of the ladder operators $\hat{b}, \hat{b}^{\dagger}$. In the rotating frame at ω_0 we can ignore the $\omega_0 + 2\omega_m$ sideband by invoking the rotating wave approximation, i.e. that ω_m is greater than any frequency of interest. The interaction Hamiltonian can then be written as,

$$-\hbar g(\hat{a}\hat{b} + \hat{a}^{\dagger}\hat{b}^{\dagger}), \tag{2.10}$$

where $g = \omega_0 \bar{a} x_q/L$. Often we call this kind of interaction a "non-linear crystal" or just "non-linear" interaction, as this same interaction Hamiltonian exists for two modes in two-mode squeezing, which uses a non-linear crystal to produce the quantum correlations.

In systems such as gravitational wave detectors we often have two cavities, e.g. an arm cavity and a signal recycling cavity. To demonstrate this we can

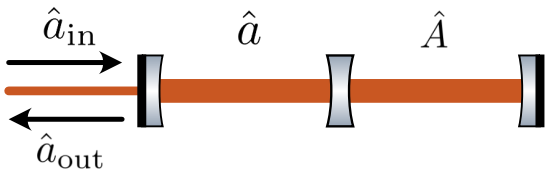

Figure 2.3 Diagram of a coupled cavity system with the coupled cavity interaction described by Eq. (2.11).

also add an extra cavity mode $\hat{A}$ as in Figure. 2.3. The interaction between two cavities described by $\hat{a}$ and $\hat{A}$ is given by the Hamiltonian,

$$i\hbar\omega_s(\hat{a}\hat{A}^\dagger - \hat{a}^\dagger\hat{A}), \tag{2.11}$$

where $\omega_s \approx \sqrt{c\gamma_A/L_a}$ where γ_A is the bandwidth of the $\hat{A}$-mode cavity and L_a is the length of the $\hat{a}$-mode cavity. Naturally, we call such a Hamiltonian a "beamsplitter-like" interaction.

Since everything is linear, to calculate transfer functions of the system we can simply calculate the first-order Heisenberg equations of motion and then solve them in the frequency-domain.

2.3 Example: Tuned Fabry-Perot Michelson Interferometer

As a concrete example we consider a FP (Fabry-Perot) Michelson interferometer with arm cavities tuned to the laser carrier frequency ω_0 shown in Figure. 2.4. As shown in [4, 13] only the differential motion of the arm cavities $\delta L = L_y - L_x$ is observed at the dark port (labelled $\hat{a}_{\text{in}}, \hat{a}_{\text{out}}$) of the inter-

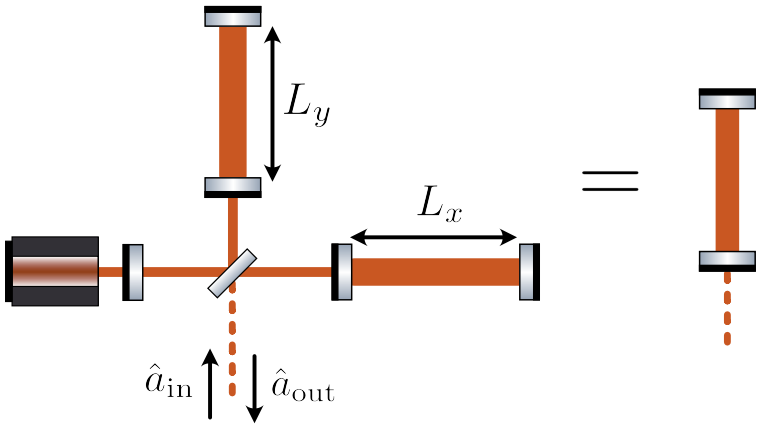

Figure 2.4 As shown in [4, 13], for small arm-length modulations $\delta L = L_y - L_x$, where $|\delta L| \ll L_y, L_x$, the tuned FP (Fabry-Perot) Michelson interferometer can be mapped directly to a tuned cavity with a suspended end mirror, such as is shown in Figure. 2.2.

ferometer for small modulations, with the differential arm cavity mode being described by $\hat{a}$. The common optical mode coupled to the common mode of the arms' motion is reflected back toward the power recycling mirror to the left of the beamsplitter, which acts only to increase the effective input power to the interferometer and hence the power in the arm cavities. On the other hand, the differential optical mode coupled to the differential arm motion is sent to the dark port. Therefore, a tuned FP (Fabry-Perot) Michelson interferometer can be mapped directly onto the cavity shown in Figure. 2.2. The Hamiltonian of the entire system is then,

$$\hat{H} = \frac{\hat{p}}{2M} - F\hat{x} - \hbar(\omega_0/L)\bar{a}\,\hat{x}(\hat{a} + \hat{a}^\dagger) - i\hbar\sqrt{\gamma}(\hat{a}\hat{c}^\dagger_{\rm ext} - \hat{a}^\dagger\hat{c}_{\rm ext}), \tag{2.12}$$

where $\hat{x}$ is the differential motion of the test masses (and $\hat{p}$ being the canonical momentum conjugate to this quantity) with effective mass $M = m_{\rm test}/4$ with

m_{test} being the actual mass of the each test-mass (see [20, 21]), L is the length of the arm cavity, $\gamma = Tc/(4L)$ where T is the transmissivity of the ITM (input test-mass). For a gravitational-wave (GW) the strain can be modelled as an applied signal force (a GW tidal force) $F = ML\ddot{h}$.

Using Heisenberg's equation of motion and the usual canonical commutation relations between each mode, the full set of equations of motion are given by,

$$\hat{a}_{\text{out}} = \hat{a}_{\text{in}} - \sqrt{2\gamma}\hat{a}, \tag{2.13}$$

$$\dot{\hat{a}} = -\gamma\hat{a} + \sqrt{2\gamma}\hat{a}_{\text{in}} + i\bar{a}(\omega_0/L)\hat{x}, \tag{2.14}$$

$$\dot{\hat{x}} = \hat{p}/M, \tag{2.15}$$

$$\dot{\hat{p}} = -ML\ddot{h} + \hbar\bar{a}(\omega_0/L)(\hat{a} + \hat{a}^\dagger). \tag{2.16}$$

For simplicity we will only calculate the shot noise transfer function by letting the test mass m_{test} (and hence effective mass M) go to infinity. In this case we obtain the following frequency-domain equations after eliminating $\hat{p}$,

$$\hat{a}_{\text{out}} = \hat{a}_{\text{in}} - \sqrt{2\gamma}\hat{a} \quad \text{(unchanged)}, \tag{2.17}$$

$$-i\Omega\hat{a} = -\gamma\hat{a} + \sqrt{2\gamma}\hat{a}_{\text{in}} + i\bar{a}\omega_0/L\hat{x}, \tag{2.18}$$

$$\hat{x} = -Lh, \tag{2.19}$$

where Ω is the sideband frequency of interest relative to the carrier ω_0.

The output field is then given by,

$$\begin{aligned}\hat{a}_{\text{out}} &= G(\Omega)\,\hat{a}_{\text{in}} + T_{h\to\hat{a}_{\text{out}}}(\Omega)\,h \\ &= \frac{\Omega - i\gamma}{\Omega + i\gamma}\hat{a}_{\text{in}} - \frac{\sqrt{2\gamma}\bar{a}\omega_0}{\Omega + i\gamma}h.\end{aligned} \tag{2.20}$$

One interesting thing to note is that if we compute the amplitude and phase quadratures for the output field, defined in Eq. (2.5), the signal is coupled only into the output phase quadrature. Intuitively this means that in a tuned FP (Fabry-Perot) Michelson interferometer the GW strain signal purely manifests as phase modulation of the measured output signal. Since a photodiode measures the power of the electric field (i.e. $\sim |E(t)|^2$) both the amplitude and phase quadratures are measured; the signal strength is greater if instead we measure just the phase quadrature via homodyne measurement [4].

The system is lossless and so $|G(\Omega)| = 1$ as expected. We are interested in the power spectral density of the noise relative to the signal strength, thus we define the strain-referred power spectral density,

$$S_{hh}(\Omega) \equiv \frac{S_{\hat{a}_{\rm out}\hat{a}_{\rm out}}(\Omega)}{|T_{h\to\hat{a}_{\rm out}}(\Omega)|^2}. \tag{2.21}$$

Because the input-output gain is unity and the input shot noise spectrum is white noise, $S_{\hat{a}_{\rm in}\hat{a}_{\rm in}} = 1$, the strain-referred power spectral density of the quantum noise is simply given by the inverse modulus squared of the strain transfer function,

$$S_{hh}(\Omega) = \frac{1}{|T_{h\to\hat{a}_{\rm out}}(\Omega)|^2} = \frac{\Omega^2 + \gamma^2}{2\gamma\bar{a}^2\omega_0^2}. \tag{2.22}$$

We see that we get a peak sensitivity of $\gamma/(2\bar{a}^2\omega_0^2)$ at $\Omega = 0$ i.e. at the arm cavity resonance, with the signal power reducing to half at the arm cavity bandwidth $\Omega = \gamma$. As discussed in Sections. 3.1 and 3.2 this is due to the positive dispersion of the arm cavities, specifically that not all frequencies are simultaneously resonant within the arm cavities. Note that the spectrum can be broadened by increasing γ, however the peak sensitivity gets worse (i.e. the

noise spectral density increases) linearly with γ. As we will discuss, this is actually a general property of passive resonant detectors, and as discussed in Section. 6.2.2 maybe even a property of a more general class of *active* resonant detectors.

Chapter Three

Bandwidth broadening via negative dispersion

This chapter contains content from the first paper listed at the beginning of the thesis and is published at Phys. Rev. D **99**, 102001 [22], the entirety of which was written by the first author Joe Bentley.

In this chapter we will discuss methods of surpassing the so-called "Mizuno limit" of passive resonant quantum measurement devices which states that the peak strain-referred power spectral density and detector bandwidth are proportional. First we will overview this limit and its origins and then explore methods of surpassing this limit. Specifically we will consider setups incorporating the concept of negative dispersion to directly broaden the detector bandwidth without sacrificing peak sensitivity.

3.1 Mizuno limit

Recall the tuned cavity transfer function given in Eq. (2.20), specifically the strain transfer function. Since the vacuum shot noise has a white noise spectrum, the signal-to-noise ratio (SNR) can be described by the integral of the squared magnitude of the strain transfer function over all frequencies,

$$\int_{-\infty}^{\infty} \mathrm{d}\Omega \; |T_h(\Omega)|^2 = \bar{a}^2\omega_0^2 \int_{-\infty}^{\infty} \mathrm{d}\Omega \; \frac{2\gamma}{\Omega^2+\gamma^2}. \tag{3.1}$$

We can evaluate this integral using Jordan's lemma and Cauchy's Residue theorem by enclosing the simple pole at $\Omega = i\gamma$ and letting the contour to go infinity, giving,

$$\int_{-\infty}^{\infty} \mathrm{d}\Omega \; |T_h(\Omega)|^2 = \bar{a}^2\omega_0^2, \tag{3.2}$$

and so the signal sensitivity is constrained entirely by the energy stored in the system and the carrier frequency, and not by any optical parameter of the system itself. Approximately we can state this as saying that the detector bandwidth (equal to γ in this case, but often not well defined) multiplied by the peak sensitivity is a constant. This is often called the "Mizuno limit" owing to Jun Mizuno, who showed that all passive optical systems with finite stored energy obey this fundamental limit [23]. In this case it occurs due to the positive dispersion of the arm cavities: when the sideband frequency is near zero the light is resonantly enhanced by constructive interference, however as the sideband frequency is increased the light begins to destructively interfere. The arm cavities serve to repeatedly reflect the light, effectively increasing the path length travelled by the light and amplifying the effect of the GW strain on its phase. The arm cavities also resonantly enhance the carrier and

increase the intracavity intensity, thereby reducing the relative photon number uncertainty and thus the shot noise.

Amazingly, modern advanced GW detectors are actually coming up against the shot-noise limit, and so this is becoming a major limiting factor, especially in regards to high-frequency signals such as binary neutron star (BNS) mergers. We can take three approaches to reducing the quantum noise:

1. Directly altering the quantum noise entering the system, for example by using non-classical states of light such as via frequency-dependent squeezing [4], which in the optimal case leads to a broadband reduction of quantum noise across a wide frequency range, or generating squeezed states internally in the setup as in [24].

2. Increasing the magnitude of the strain transfer function, e.g. by increasing the energy stored in the system by increasing the input power, however it turns out that another major limiting noise source is the thermal noise of the mirror coatings which increases with the input power.

3. Finally, modifying the shape of the strain transfer function using active elements such as negative dispersion to broaden the bandwidth directly.

In this section we will focus on this last method. Specifically we will focus on increasing the high-frequency sensitivity of gravitational-wave detectors, owing to recent detections of binary black hole (BBH) and binary neutron star (BNS) mergers [25]. Current ground-based gravitational-wave (GW) detectors such as Advanced LIGO and VIRGO, as well as future proposed detectors such as Cosmic Explorer and Einstein Telescope are all limited by the quantum shot

noise at high frequencies and so are blind to the higher frequencies of the BNS inspiral waveform, the measurement of which would allow the determination of the currently unknown neutron star equation of state [6, 7]. Improving the broadband sensitivity would also increase the SNR of currently visible events, also increasing the range of the detector.

3.2 Unstable filter

To broaden the detection bandwidth without decreasing the peak sensitivity we will consider introducing a medium with negative dispersion to compensate for the phase gained in the arm cavity, creating a so-called white light cavity [26, 27, 28, 29]. Previously, atomic systems have been used to classically demonstrate bandwidth broadening via negative dispersion [30, 31, 32, 33]. Another approach, which we will take, is to use optomechanical coupling such as the unstable optomechanical filter first described in [5] as well as more recent work using optomechanical resonators [34]. After the bandwidth is broadened, the Mizuno limit itself can be used to increase the peak sensitivity by decreasing the broadened bandwidth, i.e. it allows us to surpass the Mizuno limit. In this section we will justify and describe the unstable filter as a negative dispersion device.

As discussed in Section. 2.3, in a tuned Michelson interferometer the arm cavities are tuned to be resonant with the carrier light at frequency ω_0 so that $2\omega_0 L_{\rm arm}/c = 2\pi N$ where N is an integer, $L_{\rm arm}$ is the arm cavity length, and ω_0 is the laser carrier frequency. A GW will induce a change in path length

between the ITM (input test mass) and ETM (end test mass) oppositely for both arms, modulating the carrier light resulting in signal sidebands at $\omega_0 \pm \Omega$, with Ω being the GW signal frequency. Since the arm cavities are tuned to the carrier light these signal sidebands will not be resonant in the arm cavities, as they obtain an extra round-trip phase of $2\Omega L_{\rm arm}/c$ away from the perfect resonant condition which will therefore accrue destructively. As the GW frequency Ω increases, as does this extra round-trip phase, leading to more destructive interference and further reducing the signal strength. Therefore the arm cavities lead to decreasing sensitivity at higher frequencies. We therefore envisage a negative dispersion device that gives a round-trip phase exactly cancelling that gained in a round-trip through the arm cavity, so that the round-trip phase gained through this device is $-2\Omega L_{\rm arm}/c$. This will cancel the attenuation of the signal due to positive dispersion and effectively turn the detector into a "white-light cavity"—a cavity resonant on all frequencies—however we will only consider first-order cancellation resulting in a finite broadening of the bandwidth.

The unstable filter, highlighted in Fig. 3.1, is just one such realization of a negative dispersion device, another is discussed in section. 5.1.2. It is an optomechanical device consisting of a cavity with resonant frequency ω_0 with a fixed input mirror and a mechanically suspended end mirror as a mechanical oscillator with mechanical resonant frequency ω_m and quality factor Q_m, and with the cavity pumped by a pumping laser at frequency $\omega_0 + \omega_m$. Signal sidebands at frequency $\omega_0 \pm \Omega$ enter the unstable filter and beat with the pump field at $\omega_0 + \omega_m$, producing a radiation pressure force of frequency $\omega_m \pm \Omega$

at the mechanically suspended mirror. This force moves the mirror which modulates the cavity field to further modify the sidebands at $\omega_0 \pm \Omega$, and also modify the mirror's mechanical motion at frequency ω_m. This process is analogous to difference frequency generation, also known as optical parametric amplification, in non-linear optics, see for example p. 9 of [35]. It can be shown that assuming the so-called resolved sideband regime, where the GW sideband frequency $\Omega \ll \gamma_f \ll \omega_m$, and γ_f is the bandwidth of the filter cavity, and also assuming the system is in the unstable regime where the mechanical damping rate $\gamma_m \equiv \omega_m/Q_m$ is much less than negative damping rate due to the optomechanical interaction $\gamma_{\rm opt}$, the optical transfer function of the filter cavity takes the form,

$$\frac{\Omega + i\gamma_{\rm opt}}{\Omega - i\gamma_{\rm opt}} \approx \exp\left(-\frac{2i\Omega}{\gamma_{\rm opt}}\right), \tag{3.3}$$

where $\gamma_{\rm opt} \equiv g^2/\gamma_f$ is the negative optomechanical damping rate with g—the optomechanical coupling strength—as defined later in Eq. (3.6). In the second approximation we assumed that $\gamma_{\rm opt} \gg \Omega$, giving a first-order cancellation of the phase. The condition to exactly cancel the phase gained in the arm cavities is therefore given by, $\gamma_{\rm opt} = c/L_{\rm arm}$. Note that the system has one imaginary pole at $\Omega = i\gamma_{\rm opt}$, and so is dynamically unstable.

Previous detector designs including the unstable filter (for example [5, 36]) have considered so-called "reflection-readout" based designs, owing to the fact that we measure the signal reflected from the unstable filter. Generally in these designs, the unstable filter is externally coupled to the main interferometer as shown in Fig. 3.1 (a). Here the mechanism of broadening is intuitive, since the signal is recycled with a negative phase shift and re-injected into the arm cavity

to cancel the positive phase gained. However in the transmission-readout setup discussed in the next section the mechanism is less intuitive since the unstable filter cannot be isolated as a separate system within the entire setup. Regardless, we will show that bandwidth broadening is still achieved.

3.3 Transmission-readout setup

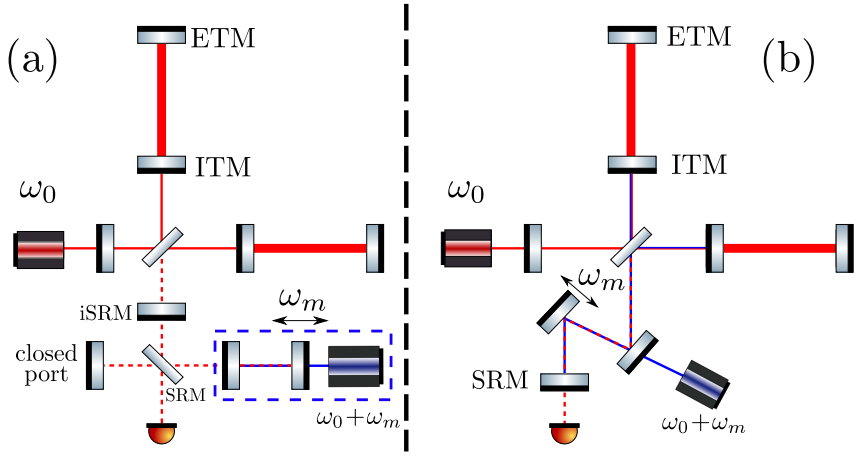

Figure 3.1 Figure (a) shows a reflection-readout design such as in [36]. The unstable filter alone is highlighted by the blue dashed box. Figure (b) shows the new transmission-readout setup proposed in this chapter. The SRC (signal recycling cavity) is pumped with laser light at $\omega_0 + \omega_m$, and the mirror above the signal recycling mirror is mechanically suspended with mechanical resonance frequency ω_m. ETM: End Test Mass, ITM: Input Test Mass, SRM: Signal Recycling Mirror, iSRM: Internal SRM (to form an impedance-matched cavity with the ITM)

The reflection-readout designs mentioned above and shown in Fig. 3.1 (a) require drastic alterations of the detector topology, for example the conversion of the SRM (signal recycling mirror) to a beamsplitter and also the addition of a low-loss closed port. In this section, we introduce a simpler "transmission-

readout" based design shown in Fig. 3.1 (b), instead requiring only the conversion of a steering mirror into a high-frequency mechanical oscillator in the signal recycling cavity, and the presence of a pump laser at $\omega_0 + \omega_m$. As an example we apply the design to an example 4km interferometer whose parameters are described in Fig. 3.2, showing that for a detector bandwidth of 1.8 kHz the shot noise can be reduced by 10 decibels as shown in Fig. 3.2 (b), however the bandwidth improvement is limited compared to reflection-readout designs as discussed toward the end of Sec. 3.3.1. We also use a mirror mass of $m = 10\,\mathrm{mg}$, and so for a fused silica (density $\rho = 2.17\,\mathrm{Mg\,m^{-3}}$) and assuming a depth of 5 mm leads to a mirror diameter of 5 cm which is greater than the beam waist in the signal recycling cavity. Additionally the mirror eigenfrequency is given by $\omega_m = 2\pi \times 10^5\,\mathrm{Hz}$. The enhancement factor over a tuned Michelson as a function of final detector bandwidth is shown in Fig. 3.2 (a).

3.3.1 Analysis

In this section we outline the analysis of the transmission-readout setup—a simplified version of which is shown in Fig. 3.3 by focusing on the differential mode only. In comparison to the reflection-readout setup in Fig. 3.1 (a) the arm cavity is no longer coupled directly to the dark port. Instead the arm cavity and filter cavity form an effective three-mirror cavity similar to the twin signal-recycling scheme studied in [37, 38], except with one cavity replaced with the optomechanical filter cavity.

To analyse the system we use a Hamiltonian-based approach as in section. 2.3, which was also used to analyse the reflection-readout setup in [5].

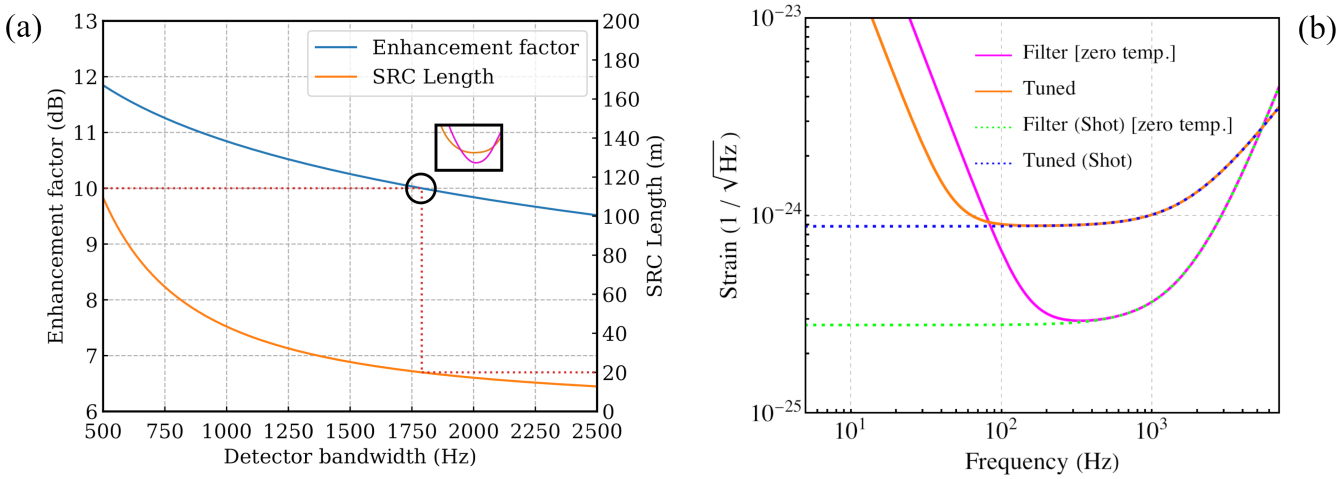

Figure 3.2 Figure (a) shows the peak sensitivity improvement ratio of the transmission-readout setup to a tuned signal-recycled Michelson interferometer as a function of broadened detector bandwidth Γ_{detector} as given in Eq. (3.35). Here advanced LIGO parameters are used (4 km arm length, 40 kg test mass, 800 kW arm power), and additionally an ITM transmissivity of 0.045 and SRM transmissivity of 0.0003 are used. The SRC length solved for the detector bandwidth is also plotted to show how it could be varied to improve the peak sensitivity with these transmissivities. The dotted line is plotted for our chosen SRC length of 20 m, giving a detector bandwidth of around 1790 Hz, and therefore an enhancement factor of 10 dB. The circled value and inset highlights the chosen values used in figure (b), which shows the total quantum noise with the unstable filter mirror at zero temperature. The tuned Michelson bandwidth set to the effective bandwidth of the new transmission readout setup as discussed at the end of Sec. 3.3.1. We also assume 10 dB frequency-dependent squeezing over the entire frequency range as outlined in [4].

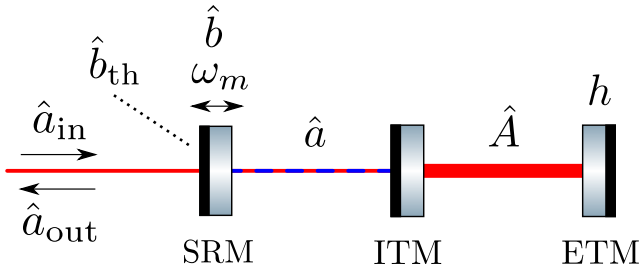

Figure 3.3 Figure showing the setup analysed in Sec. 3.3.1, which is a simplified version of Fig. 3.1 (b). $\hat{a}$ describes the unstable filter cavity mode, $\hat{A}$ describes the differential arm cavity mode, $\hat{b}$ is the mirror oscillation mode, h is the GW strain signal, and the mirror is coupled to an external heat bath described by the continuum field $\hat{b}_{\rm th}$, shown by the dotted line. The cavity field $\hat{a}$ is coupled to the external continuum fields $\hat{a}_{\rm in}, \hat{a}_{\rm out}$.

This approach is valid under the single-mode approximation where the GW sideband frequency $\Omega/(2\pi) \ll$ FSR where FSR is the free spectral range of either the SRC or arm cavities, i.e. only modes within one free spectral range are considered. This can be important for long-baseline facilities such as the 40 km Cosmic Explorer where the free spectral range is only 3.75 kHz.

The approach consists of first writing the Hamiltonian for the system, which, referring again to Fig. 3.3, consists of SRC mode $\hat{a}$ and differential arm cavity mode $\hat{A}$, as well as a mechanically suspended mirror which is modelled as a damped-driven harmonic oscillator with resonant frequency ω_m and mechanical damping rate γ_m which is described by mode $\hat{b}$. The mirror is additionally coupled to an external continuum of modes $\hat{b}_{\rm th}$ which represents an external heat bath. The equations of motion are then computed using Heisenberg's equations of motion which are then solved in the frequency-domain to give an equation for an output field at the dark port $\hat{a}_{\rm out}$ in terms of input fields $\hat{a}_{\rm in}$ and the GW strain h. The two-photon quadratures [39, 4] are then

computed, and hence the spectral density for the quadrature operators. The external fields $\hat{a}_{\rm in}$, $\hat{a}_{\rm out}$, and $\hat{b}_{\rm th}$ describe a freely propagating continuum of modes as in [18].

The total Hamiltonian is given by $\hat{H}_{\rm tot} = \hat{H}_0 + \hat{H}_{\rm int}^{\rm filter} + \hat{H}_{\rm int}^{\rm ETM} + \hat{H}_{\gamma_f} + \hat{H}_{\gamma_m} + \hat{H}_{\gamma_{\rm arm}}$. Here $\hat{H}_0$ is the free part, $\hat{H}_{\rm int}^{\rm filter}$ describes the interaction between the SRC mode and the mechanically suspended mirror, $\hat{H}_{\rm int}^{\rm ETM}$ describes the radiation pressure coupling between the ETM and arm cavity field as well as to the GW strain (we choose the ITM to be static without loss of generality), $\hat{H}_{\gamma_f}$ describes the coupling of the SRC to the external continuous vacuum field (the dark port) as discussed in [17][1] and $\gamma_f = T_{\rm SRM}c/(4L_{\rm SRC})$—where $T_{\rm SRM}$ is the SRM power transmissivity and $L_{\rm SRC}$ is the length of the signal recycling cavity—is the coupling constant of the SRC to the external field, $\hat{H}_{\gamma_m}$ describes the coupling of the mirror to the external heat bath $\hat{b}_{\rm th}$ with coupling constant $\gamma_m = \omega_m/Q_m$—where ω_m is the mirror eigenfrequency and Q_m is the mechanical quality factor—whose equation of motion will be the quantum Langevin equation [15] [19, p. 158], and finally $\hat{H}_{\gamma_{\rm arm}}$ describes the coupling between the SRC and the arm cavity [37, 38].

The free Hamiltonian $\hat{H}_0$ is given by,

$$\hat{H}_0 = \frac{\hat{p}^2}{2m} + \frac{1}{2}m\omega_m^2\hat{x}^2 + \hbar\omega_0\hat{a}^\dagger\hat{a} + \hbar\omega_0\hat{A}^\dagger\hat{A} + \frac{\hat{P}^2}{2M}, \tag{3.4}$$

[1]The method in [17] reproduces the quantum Langevin equation of [15] and [19, p. 158], and also [40, 41], in which the setup is known as input-output theory of open quantum systems [41]. Note that a simple cavity coupled to an external bosonic field is mechanically equivalent to a mechanical mass coupled to an external heat bath, as evident by comparing equations (3.10) and (3.11)

where $\hat{P}$ is the differential arm momentum, and $M = m_{\rm test}/4$ is the reduced mass of the differential mechanical mode $\hat{X}$, which is coupled to the differential arm cavity mode $\hat{A}$, and $m_{\rm test}$ being the actual mirror mass [20, 21]; ω_0 is the carrier frequency of the main interferometer laser and also the resonant frequency of the arm cavities; $\hat{p}$ is the momentum of the mechanically suspended mirror, $\hat{x}$ is its position, and m is its mass. The mirror pendulum frequency is assumed to be very low compared to any frequency of interest and thus we neglect it in the dynamics. The filter cavity field $\hat{a}$ is pumped by a laser at frequency $\omega_0 + \omega_m$ resulting in a mean photon number $\bar{a}$. The linearised (using the same process as in section. 2.2) filter interaction Hamiltonian is given by [17, 41, 5],

$$\hat{H}_{\rm int}^{\rm filter} = -\hbar g_0[\hat{a}e^{i(\omega_0+\omega_m)t} + \hat{a}^\dagger e^{-i(\omega_0+\omega_m)t}]\hat{x}, \tag{3.5}$$

where $g_0 = (\omega_0/L_f)\bar{a}$, $\bar{a} = [2P_f L_f/(\hbar\omega_0 c)]^{1/2}$, where P_f is the circulating power in the filter cavity and L_f is the length of the filter cavity. The mirror displacement can be written in the Heisenberg picture as $\hat{x} = x_q(\hat{b}e^{-i\omega_m t} + \hat{b}^\dagger e^{i\omega_m t})$, where x_q is the ground-state harmonic oscillator position uncertainty, $x_q = \sqrt{\hbar/(2m\omega_m)}$. We then move into the rotating frame at ω_0 and disregard the $\omega_0 + 2\omega_m$ sideband by invoking the rotating wave approximation (RWA), since $\gamma_f \ll \omega_m$ for any frequency of interest, however this approximation should be relaxed for a full analysis. The interaction Hamiltonian therefore becomes, [5]

$$\hat{H}_{\rm int}^{\rm filter} \approx -\hbar g(\hat{a}\hat{b} + \hat{a}^\dagger\hat{b}^\dagger), \tag{3.6}$$

where $g = g_0 x_q$.

For the ETM dynamics we have a term due to the effective GW interaction with the mirror, and another due to the linearised radiation pressure interaction between the mirror and arm cavity field,

$$\hat{H}_{\rm int}^{\rm ETM} = F_{\rm GW}\hat{X} - \hbar G_0(\hat{A} + \hat{A}^\dagger)\hat{X}, \tag{3.7}$$

where $F_{\rm GW} = ML_{\rm arm}\ddot{h}$ is the GW tidal force, $G_0 = \omega_0/L_{\rm arm}\bar{A}$, and $\bar{A} = [2P_{\rm arm}L_{\rm arm}/(\hbar\omega_0 c)]^{1/2}$, where $P_{\rm arm}$ is the arm cavity power, $L_{\rm arm}$ is the arm cavity length.

Finally as in Eq. (2.11) there is the transfer of excitation between the SRC and arm cavity [37, 38], which leads to the interaction term,

$$\hat{H}_{\gamma_{\rm arm}} = i\hbar\omega_S(\hat{a}\hat{A}^\dagger - \hat{a}^\dagger\hat{A}), \tag{3.8}$$

where $\omega_S \approx \sqrt{c\gamma_{\rm arm}/L_{\rm SRC}}$ is called the "sloshing frequency", with $L_{\rm SRC}$ being the length of the signal-recycling cavity, and $\gamma_{\rm arm} = T_{\rm ITM}c/(4L_{\rm arm})$ is the arm cavity bandwidth, with $T_{\rm ITM}$ being the power transmissivity of the ITM.

Therefore we obtain the full set of equations of motion,

$$\hat{a}_{\rm out} = \hat{a}_{\rm in} - \sqrt{2\gamma_f}\hat{a} \tag{3.9}$$

$$\dot{\hat{a}} + \gamma_f\hat{a} = ig\hat{b}^\dagger + \sqrt{2\gamma_f}\hat{a}_{\rm in} - \omega_S\hat{A} \tag{3.10}$$

$$\dot{\hat{b}} + \gamma_m\hat{b} = ig\hat{a}^\dagger + \sqrt{2\gamma_m}\hat{b}_{\rm th} \tag{3.11}$$

$$\dot{\hat{A}} = \omega_S\hat{a} + iG_0\hat{X} \tag{3.12}$$

$$\dot{\hat{X}} = \hat{P}/M \tag{3.13}$$

$$\dot{\hat{P}} = -ML\ddot{h} + \hbar G_0(\hat{A} + \hat{A}^\dagger), \tag{3.14}$$

where γ_f is the filter cavity bandwidth as defined above.

To analyse the stability of the system, the dynamical matrix can be read off of Eqs. (3.10)–(3.12) as,

$$A = \begin{bmatrix} -\gamma_f & ig & -\omega_s \\ -ig & -\gamma_m & 0 \\ \omega_s & 0 & 0 \end{bmatrix}, \tag{3.15}$$

where the state vector is $\mathbf{x} = (\hat{a}, \hat{b}^\dagger, \hat{A})^T$. Since $\gamma_m \ll \omega_s, \gamma_f, \omega_s$ we set γ_m to zero. The eigenvalues are then $\{0, \frac{1}{2}\left(-\gamma_f \pm \sqrt{\gamma_f^2 + 4g^2 - 4\omega_s^2}\right)\}$. For $g > \omega_s$, which is the regime that we use to achieve the improvement in this chapter, there is an eigenvalue with positive real part, and so the system is dynamically unstable. For $g \leq \omega_s$ the eigenvalues have a negative (or zero) real part and so the system is dynamically stable.

These equations are then transformed to the frequency domain, noting that the property of the Fourier transform $\mathcal{F}\left[\hat{a}^\dagger(t)\right] = (\hat{a}^\dagger)(-\Omega)$ which we will simply denote as $\hat{a}^\dagger(-\Omega)$, which represents the amplitude of the lower sideband. The equations are then solved to calculate the output field $\hat{a}_{\rm out}(\Omega)$ in terms of the input fields $\hat{a}_{\rm in}(\Omega)$, $\hat{a}^\dagger_{\rm in}(-\Omega)$ and the GW strain signal $h(\Omega)$. Note that since $h(t)$ is real, $h(\Omega) = h^*(-\Omega)$. From these transfer functions an input-output relation for the sidebands can be constructed of the form,

$$\begin{bmatrix} \hat{a}_{\rm out}(\Omega) \\ a^\dagger_{\rm out}(-\Omega) \end{bmatrix} \equiv \mathbb{M}_s \begin{bmatrix} \hat{a}_{\rm in}(\Omega) \\ \hat{a}^\dagger_{\rm in}(-\Omega) \end{bmatrix} + \mathbb{M}_s^{\rm th} \begin{bmatrix} \hat{b}_{\rm th}(\Omega) \\ \hat{b}^\dagger_{\rm th}(-\Omega) \end{bmatrix} + \vec{D}_s h(\Omega), \tag{3.16}$$

where $\mathbb{M}_s$ is the transfer matrix of the input field to the output field at the dark port for the single-photon (sideband) modes, representing the overall linearised dynamics of the system, similarly $\mathbb{M}_s^{\rm th}$ is the transfer matrix for the

thermal noise to the dark port output field, and $\vec{D}_s$ represents the linearised coupling of the GW strain signal into the upper and lower sidebands of the dark port output field.

There is another independent contribution to the quantum noise: the thermal noise arising from the coupling of the mechanically suspended mirror to the fluctuating environmental heat bath $\hat{b}_{\rm th}$ at temperature T. As shown in Appendix. B, the heat bath provides random thermal fluctuations whose statistics are determined by the Bose-Einstein distribution,

$$S_{\hat{b}_{\rm th}\hat{b}_{\rm th}}(\Omega) = 1 + \frac{2}{e^{\frac{\hbar\omega_0}{k_B T}} - 1}. \tag{3.17}$$

When the thermal occupation number is high, i.e. $k_B T \gg \hbar\omega_m$, this leads to a spectral density given approximately by [41, 5],

$$S_{\hat{b}_{\rm th}\hat{b}_{\rm th}}(\Omega) = \frac{2k_B T}{\hbar\omega_m}. \tag{3.18}$$

To calculate the power spectral density (PSD) due to the quantum noise we use the two-photon formalism using quadrature operators $\hat{a}_1, \hat{a}_2$—respectively called the amplitude and phase quadratures—with the input quadratures at the dark port having a flat spectral density equal to unity. These quadrature operators are related to the single-photon (sideband) operators by a unitary transformation,

$$\begin{bmatrix} \hat{a}_1 \\ \hat{a}_2 \end{bmatrix} = \frac{1}{\sqrt{2}} \begin{bmatrix} 1 & 1 \\ -i & i \end{bmatrix} \begin{bmatrix} \hat{a}(\Omega) \\ \hat{a}^\dagger(-\Omega) \end{bmatrix} \equiv \mathbb{U} \begin{bmatrix} \hat{a}(\Omega) \\ \hat{a}^\dagger(-\Omega) \end{bmatrix}. \tag{3.19}$$

We need to compute the transfer functions between the output quadratures

and the input quadratures and strain signal of the form,

$$\begin{bmatrix} \hat{a}_1^{\rm out} \\ \hat{a}_2^{\rm out} \end{bmatrix} = \mathbb{M}_q \begin{bmatrix} \hat{a}_1^{\rm in} \\ \hat{a}_2^{\rm in} \end{bmatrix} + \mathbb{M}_q^{\rm th} \begin{bmatrix} \hat{b}_1^{\rm th} \\ \hat{b}_2^{\rm th} \end{bmatrix} + \vec{D}_q h(\Omega), \tag{3.20}$$

where $\hat{a}_{1,2}^{\rm in}$ and $\hat{a}_{1,2}^{\rm out}$ are the quadratures at the optical input and output port respectively, and $\hat{b}_{1,2}^{\rm th}$ are the quadratures input from the thermal heat bath. As shown in Appendix. A, the relation between the quadrature transfer matrices and the sideband transfer matrices in Eq. (3.16) are given by,

$$\mathbb{M}_q = \mathbb{U}\,\mathbb{M}_s\mathbb{U}^\dagger, \quad \mathbb{M}_q^{\rm th} = \mathbb{U}\,\mathbb{M}_s^{\rm th}\,\mathbb{U}^\dagger, \quad \vec{D}_q = \mathbb{U}\,\vec{D}_s. \tag{3.21}$$

The output quadrature operator for a homodyne measurement with homodyne angle ζ is given by $\hat{a}_\zeta^{\rm out} = (\hat{a}_1^{\rm out}, \hat{a}_2^{\rm out}) \cdot (\cos\zeta, \sin\zeta)^T$. To calculate the spectral density we first separate the output quadrature into a zero-mean noise term and a mean signal term, $\hat{a}_\zeta^{\rm out} = \Delta\hat{a}_\zeta^{\rm out} + \langle \hat{a}_\zeta^{\rm out} \rangle$, where,

$$\Delta\hat{a}_\zeta^{\rm out} = \left(\left[\mathbb{M}_q \begin{pmatrix} \hat{a}_1^{\rm in} \\ \hat{a}_2^{\rm in} \end{pmatrix} \right]^T + \left[\mathbb{M}_q^{\rm th} \begin{pmatrix} \hat{b}_1^{\rm th} \\ \hat{b}_2^{\rm th} \end{pmatrix} \right]^T \right) \cdot \begin{pmatrix} \cos\zeta \\ \sin\zeta \end{pmatrix}, \tag{3.22}$$

$$|\langle \hat{a}_\zeta^{\rm out} \rangle|^2 = |\vec{D}_q^{(1)} \cos\zeta + \vec{D}_q^{(2)} \sin\zeta|^2 |h|^2 \tag{3.23}$$

where $\vec{D}_q^{(i)}$ is the i-th element of $\vec{D}_q$.

The single-sided PSD $S_{OO}(\Omega)$ of an operator $\hat{O}(\Omega)$ for an input vacuum state $|0\rangle$ is given by the symmetrised covariance, [4, 42, 40]

$$\langle 0|\hat{O}(\Omega)\hat{O}^\dagger(\Omega')|0\rangle_{\rm sym} = \pi\, S_{OO}(\Omega)\delta(\Omega - \Omega'). \tag{3.24}$$

First calculating the vacuum noise for $\hat{a}_\zeta^{\rm out}$, using that $\langle 0|\hat{a}_i^{\rm in}(\Omega)\,\hat{a}_j^{\rm in\,\dagger}(\Omega')|0\rangle_{\rm sym} = \pi\,\delta_{ij}\delta(\Omega - \Omega')$, and then dividing by the strain transfer function, we find the

PSD of the vacuum noise superimposed on the strain measurement is,

$$S_h^{\zeta}(\Omega) = \frac{(\cos\zeta, \sin\zeta)\mathbb{M}_q(\Omega)\,\mathbb{M}_q^{\dagger}(\Omega)(\cos\zeta, \sin\zeta)^T}{|\vec{D}_q^{(1)}\cos\zeta + \vec{D}_q^{(2)}\sin\zeta|^2}. \tag{3.25}$$

We will assume an ideal phase quadrature measurement ($\zeta = \pi/2$) at the photodiode, in which case we are only concerned about the output phase quadrature $\hat{a}_2^{\text{out}}$. In this case we have,

$$S_h(\Omega) = \frac{|\mathbb{M}_q^{(2,1)}(\Omega)|^2 + |\mathbb{M}_q^{(2,2)}(\Omega)|^2}{|\vec{D}_q^{(2)}|^2} \equiv S_{\text{vacuum}}^{\text{rp}}(\Omega) + S_{\text{vacuum}}^{\text{shot}}(\Omega), \tag{3.26}$$

where the first term is the noise contribution due to the radiation pressure while the latter is due to the shot noise.

We can follow the same process as above to find the thermal noise fluctuations arising from thermal noise quadrature operators $\hat{b}_{1,2}^{\text{th}}$, noting that the spectral density for the heat bath is given by Eq. (3.18).

For both the vacuum and thermal noise we define the shot-noise contributions $S_{\text{vacuum}}^{\text{shot}}(\Omega)$ and $S_{\text{thermal}}^{\text{shot}}(\Omega)$ as the spectral density contribution remaining when the mass $M \to \infty$, and the radiation-pressure contributions $S_{\text{vacuum}}^{\text{rp}}(\Omega)$ and $S_{\text{thermal}}^{\text{rp}}(\Omega)$ as the term remaining when the shot-noise contribution is subtracted from the total spectrum.

Assuming that $\gamma_m \ll \Omega$, we find that the strain-referred shot-noise limited PSD is given by,

$$S_h^{\text{shot}}(\Omega) = \frac{\Omega^2\gamma_f^2 + (g^2 - \omega_S^2 + \Omega^2)^2}{4G_0^2L_{\text{arm}}^2\gamma_f\omega_S^2} + \frac{g^2\gamma_m\left(\frac{2k_BT}{\hbar\omega_m} + 1\right)}{G_0^2L_{\text{arm}}^2\omega_S^2}, \tag{3.27}$$

and the radiation-pressure limited PSD is given by,

$$S_h^{\text{rp}}(\Omega) = \frac{4G_0^2\hbar^2\omega_S^2}{M^2\Omega^4L_{\text{arm}}^2\left[\Omega^2\gamma_f^2 + (g^2 - \omega_S^2 + \Omega^2)^2\right]}\left[\gamma_f + \frac{g^2\gamma_m}{\Omega^2}\left(\frac{2k_BT}{\hbar\omega_m} + 1\right)\right], \tag{3.28}$$

where in both cases the former term is the vacuum contribution and the latter term $\propto \gamma_m$ is the thermal contribution.

The total strain-referred vacuum-limited PSD can be written in the form,

$$S_{\rm vacuum}(\Omega) \equiv S_h(\Omega)|_{T=0} = \left(\frac{1}{\mathcal{K}} + \mathcal{K}\right)\frac{h_{\rm SQL}^2}{2} \geq h_{\rm SQL}^2. \tag{3.29}$$

Here $h_{\rm SQL}^2 \equiv 2\hbar/(M\Omega^2 L_{\rm arm}^2) = 8\hbar/(m_{\rm test}\Omega^2 L_{\rm arm}^2)$ is the standard quantum limit [42, 4, 13], and $\mathcal{K}$ is a dimensionless factor given by,

$$\mathcal{K} \equiv \frac{8P_{\rm arm}\omega_0}{ML_{\rm arm}c}\frac{\gamma_f\omega_S^2}{\Omega^2\left(\Omega^2\gamma_f^2 + (g^2+\Omega^2-\omega_S^2)^2\right)}, \tag{3.30}$$

where the radiation pressure coupling constant G_0 has been written out fully.

The transmission-readout shot noise spectral density (given by Eq. (3.27)) matches peak sensitivity (shot noise PSD at $\Omega = 0$) of a tuned signal-recycled Michelson interferometer if we have the condition,

$$g^2 = \omega_S^2 + \gamma_f\omega_S, \tag{3.31}$$

and we set the tuned signal-recycled Michelson detector bandwidth $\gamma_{\rm detector} = \gamma_f$. In this case the peak sensitivity for both the transmission readout setup and tuned Michelson is given by,

$$S_{\rm trans}^{\rm shot}(\Omega=0) = S_{\rm tuned}^{\rm shot}(\Omega=0) = \frac{\gamma_f}{4G_0^2L_{\rm arm}^2}. \tag{3.32}$$

The broadened effective detector bandwidth of the transmission readout setup can be shown to be on the order of $\sqrt{\gamma_f\omega_S}$, or in terms of optical parameters,

$$\Gamma_{\rm detector} \sim \frac{c}{2\sqrt{2}}\left[\frac{T_{\rm ITM}T_{\rm SRM}^2}{L_{\rm arm}L_{\rm SRC}^3}\right]^{1/4}. \tag{3.33}$$

To compare the shot noise limited sensitivity of our setup to a tuned signal-recycled Michelson interferometer, we set the tuned Michelson detector bandwidth to be equal to the effective bandwidth of the transmission readout setup, i.e. $\gamma_{\text{detector}} = \Gamma_{\text{detector}} \, (= \sqrt{\gamma_f \omega_S})$. In this case the improvement ratio of the peak power spectral densities, i.e. the power ratio of the tuned Michelson to transmission readout setup shot noise power spectral densities at low frequencies, is given by,

$$\eta \equiv \frac{S^{\text{shot}}_{\text{tuned}}(\Omega = 0)}{S^{\text{shot}}_{\text{trans}}(\Omega = 0)} = \frac{\sqrt{\gamma_f \omega_S}}{\gamma_f} = \sqrt{\frac{\omega_S}{\gamma_f}} \tag{3.34}$$

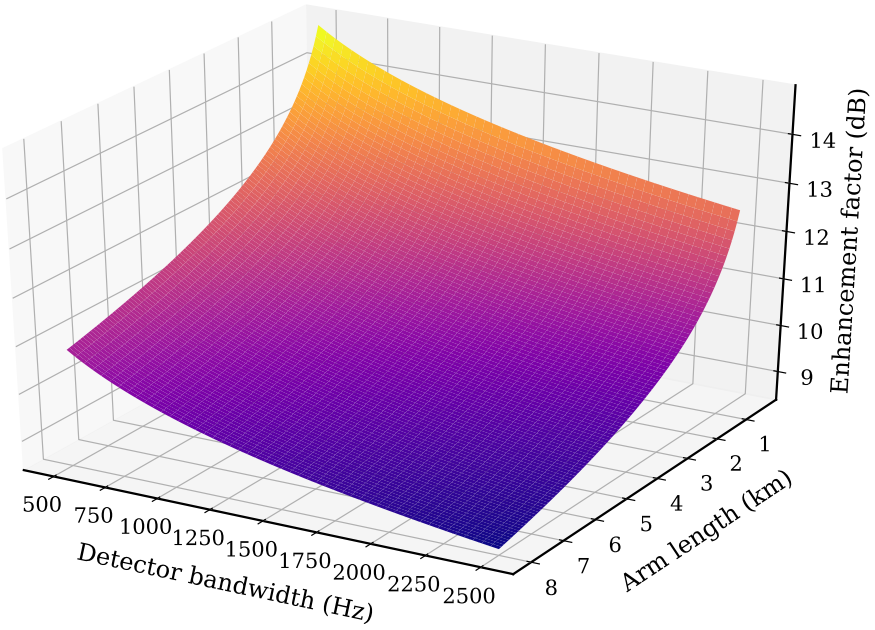

Figure 3.4 Surface plot showing the peak sensitivity improvement power ratio of the transmission-readout setup to a tuned Michelson as a function of both detector bandwidth Γ_{detector} and arm length, showing the (log) inverse cube-root dependence of the enhancement factor on the arm length. The parameters are as in Fig. 3.2.

By solving Eq. (3.33) for the SRC length, the above improvement factor

can be written in terms of the effective bandwidth, arm length, and SRM and ITM power transmissivities as,

$$\eta = \left(\frac{cT_{\mathrm{ITM}}}{\Gamma_{\mathrm{detector}} L_{\mathrm{arm}} T_{\mathrm{SRM}}} \right)^{1/3}. \tag{3.35}$$

This quantity is shown for various detector bandwidths in Fig. 3.2 (a), and a surface plot for various arm lengths is shown in Fig. 3.4. Note that it is proportional to $(T_{\mathrm{ITM}}/T_{\mathrm{SRM}})^{1/3}$, however if the ITM transmissivity T_{ITM} is increased then the arm cavity intracavity power will be decreased and hence the shot noise increased, thereby requiring a higher input power. Similarly if the SRM transmissivity T_{SRM} is very small then losses start to dominate. Finally, note that the enhancement factor for a given effective detector bandwidth decreases as the inverse cube root of the arm cavity length L_{arm}.

For both the shot noise and radiation pressure it was found that the ratio of the absolute value squared of the thermal fluctuation to the vacuum fluctuation noise has the form of a "low-pass filter". For the shot noise ratio we assume the resolved sideband regime, whereas for the radiation pressure ratio no approximation is made. For the shot noise the effective cutoff frequency is $(g^2 - \omega_S^2)/\gamma_f$. Note that when the replacement $g^2 = \omega_S^2 + \gamma_f \omega_S$ is performed, as described later, the cutoff frequency becomes ω_S. Therefore the thermal noise is suppressed relative to the vacuum noise at high frequencies where shot noise dominates, however for $\gamma_m \ll \Omega$ we find that the contribution is approximately flat as shown in Eq. (3.27). For the radiation pressure term, the cutoff frequency γ_m is very small compared to Ω, however the gain $g^2/(\gamma_f \gamma_m) \equiv \gamma_{\mathrm{opt}}/\gamma_m$ is very large, and so at low frequencies the thermal noise is much greater than the vacuum noise. Intuitively, at low frequencies the

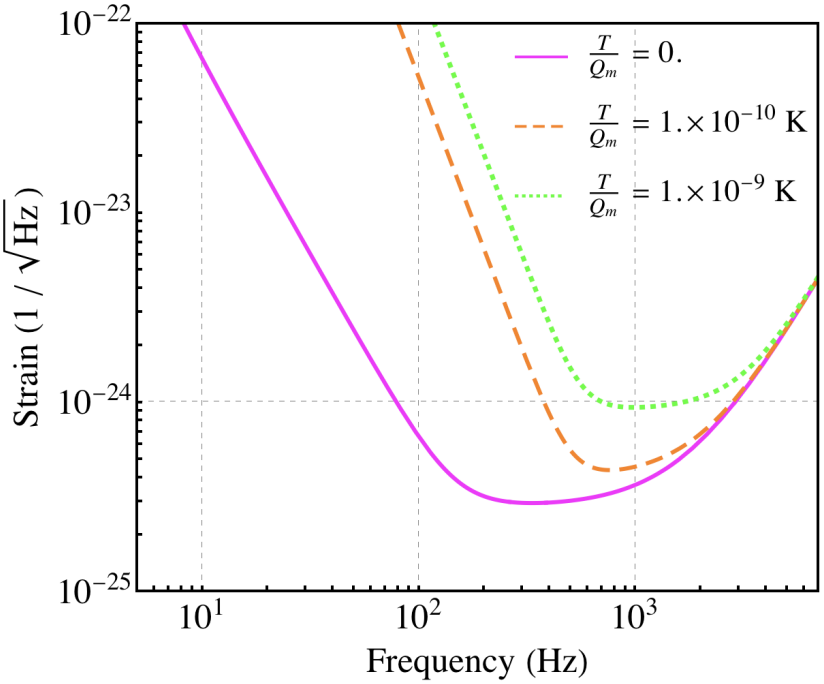

Figure 3.5 Figure showing the total quantum noise of the transmission-readout setup after including the thermal noise at various environmental temperatures, using the parameters in Fig. 3.2, including the detector bandwidth marked by the black circle ($\sim$ 1800 Hz). At low frequencies the thermal noise is amplified relative to the vacuum noise, while at high frequencies it has a flat spectrum.

thermal heat bath fluctuations are amplified by the response function of the mechanically suspended mirror in the filter cavity. The total quantum noise plot is shown in Fig. 3.5. Note that for $\gamma_m \ll \Omega$ the high-frequency thermal noise contribution is balanced by the diminishing strain response and has a flat spectrum as shown in Eq. (3.27).

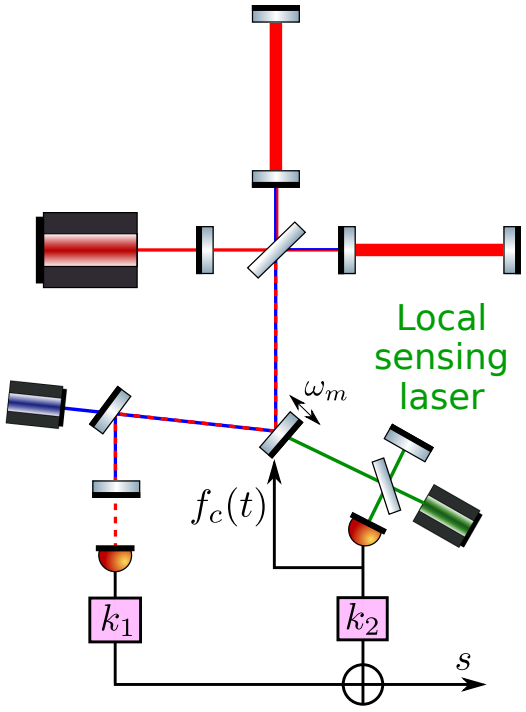

Figure 3.6 Figure showing an example of the local sensing control scheme applied to the transmission-readout setup. A control force $f_c(t)$ is applied to the mechanically suspended mirror, whose displacement is read out by the local sensing laser. The local sensing readout and main readout are optimally combined by coefficients k_1 and k_2 to recover the bandwidth broadened sensitivity.

3.3.2 Discussion

As shown above, the amplitude improvement goes as the square root of the effective bandwidth, while the decrease in peak sensitivity of the transmission readout setup goes as the effective bandwidth, and therefore we are limited in the improvement we can achieve before we start to degrade the overall sensitivity. For the previous reflection-readout setups, the effective bandwidth is given by $(\gamma_f {\omega_{S\,\mathrm{refl}}}^2)^{1/3}$ (where the sloshing frequency $\omega_{S\,\mathrm{refl}} = \sqrt{c\gamma_f / L_{\mathrm{arm}}}$ is defined differently to our analysis since we are measuring in reflection of the

unstable filter cavity rather than in transmission [5]), however in that case it can be increased further by decreasing the filter cavity length or increasing the ETM transmissivity without adversely affecting the shot noise or radiation pressure noise.

There is also strong coupling of the thermal noise into the unstable filter, putting a strict requirement on the environmental temperature. This can be mitigated using the optical dilution outlined in [43, 44, 45, 46, 47], stiffening the dynamics of the suspended mirror, although further R&D is required and ongoing to fabricate mechanical resonators with higher quality factors via optical dilution or other methods [48, 49, 50, 51, 52]. The thermal noise spectrum in this chapter differs from the flat thermal noise spectrum in previous designs [5, 36] since in this case the thermal heat bath fluctuations are fully shaped by the interferometer, except coupled indirectly by the mechanically suspended mirror. Overall it was found that at low frequencies the thermal noise contribution follows the vacuum noise except it is significantly larger by a factor $\gamma_{\mathrm{opt}}/\gamma_m \gg 1$, while the high-frequency thermal noise has a flat contribution.

Another issue is the control of the unstable dynamics of the system. Previously in [5] a stabilizing controller was constructed, however the time delay of the control signal from the arm cavities to the unstable filter were neglected. If they are included, it can be shown that the achievable phase margin will be very small. One other option is to use local sensing control to locally control the unstable filter, eliminating the time delay. Unfortunately, this will impart significant additional noise on the measurement readout, however as

Denis Martynov has discovered this local sensing noise can be cancelled out in post-processing by combining the local sensing readout and main readout optimally. An example of a local sensing control scheme for the transmission readout setup is given in Fig. 3.6.

Finally, for the analysis of future long-baseline GW detectors we need to relax the single-mode approximation, as well as the resolved sideband regime approximation which is manifested in the analysis as the rotating wave approximation, specifically that $\gamma_f \ll \omega_m$ and so we could ignore the sideband around $\omega + 2\omega_m$.

Chapter Four

Local sensing control

The unstable filter, or indeed any system with unstable dynamics, needs some form of control in order to be physically realised. In this section we will briefly overview some concepts used in the control of dynamical systems, as well as considering a method of locally controlling unstable systems while removing the added local control noise in post-processing.

4.1 Brief overview of control theory

In this section we will briefly review the state-space formalism for describing linear dynamical systems, which will be also used extensively throughout Chapter 5, and also discuss negative feedback and stability.

The most general system we will consider has linear dynamics and an arbitrary number of input and output ports. Such a system can be fully

described by two equations,

$$\dot{\mathbf{x}}(t) = A\,\mathbf{x}(t) + B\,\mathbf{u}(t), \tag{4.1}$$

$$\mathbf{y}(t) = C\,\mathbf{x}(t) + D\,\mathbf{u}(t), \tag{4.2}$$

where $\mathbf{x} = (x_1; \ldots; x_n)^T$ are the states of the system, describing the n internal degrees-of-freedom of the system, $\mathbf{u} = (u_1; \ldots; u_l)^T$ are the l inputs to the system, and $\mathbf{y} = (y_1; \ldots; y_m)^T$ are the m outputs of the system. The matrix $A \in \mathbb{C}^{n\times n}$ describes the internal dynamics of the system, $B \in \mathbb{C}^{n\times l}$ describes the coupling of the input into the internal degrees of freedom, $C \in \mathbb{C}^{m\times n}$ describes the coupling of the internal degrees of freedom into the outputs of the system, and $D \in \mathbb{C}^{m\times l}$ describes the "direct-feed" of the inputs to the outputs. If the system has one input and one output we call it a SISO (single-input single-output) system, if it has more than one input and more than one output we call it a MIMO (multiple-input multiple-output) system, similarly we can have SIMO (single-input multiple-output) or MISO (multiple-input single-output) systems. It can be easily shown by solving Eq. (4.1) and then diagonalising A that the system is dynamically stable given some fixed initial condition if $\Re\{\lambda_i\} < 0,\ \forall i$ where λ_i is the i-th eigenvalue of the dynamical matrix A [53].

We define the Laplace transform for a function $f(t)$ as,

$$f(s) = \int_{0^-}^{\infty} \mathrm{d}t\, e^{+st} f(t). \tag{4.3}$$

Note that s is not negated in the exponent, differing from other, possibly more common, conventions. $s = r + i\Omega$ is generally a complex number, with r

describing some exponential growth or decay and Ω labelling a Fourier component of the oscillation.

By taking the Laplace transform of the Eqs. (4.1) and (4.2) and then eliminating the internal degrees of freedom we can derive the transfer matrix,

$$\mathbf{G}(s) = C(-sI - A)^{-1}B + D, \tag{4.4}$$

where $\mathbf{G}(s) \in \mathbb{C}^{m\times l}$ and $y_i(s) = \sum_j \mathbf{G}_{i,j}(s)u_j(s)$. For simplicity we now focus on a SISO system and thus consider the transfer function $G(s)$. Generally this is in a pole-zero form,

$$G(s) = \frac{B(s)}{A(s)} = \frac{\prod_{i=1}^{n}(s+b_i)}{\prod_{j=1}^{m}(s+a_j)}, \tag{4.5}$$

with $B(s)$ and $A(s)$ being finite-order polynomials in s. The zeroes of $B(s)$ are called the zeroes of the system, while the zeroes of $A(s)$ are called the poles of the system. The poles are called *simple* poles if none of the a_j are degenerate [54]. In our Laplace convention, an unstable pole occurs when any of the a_j have a negative real part (since the Laplace transform of an exponential growth is a simple pole). However, in cases where a simple zero cancels a simple pole the instability disappears.

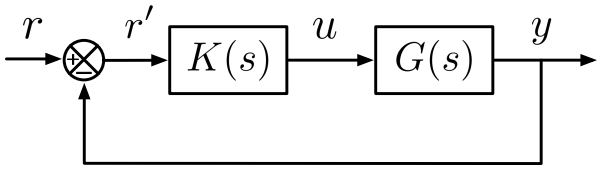

Figure 4.1 A block diagram showing the open-loop dynamics $G(s)$ modified using a controller $K(s)$, with the loop then closed via negative feedback $r' = r - y$.

We usually refer to $G(s)$ as the *open-loop* transfer function (or matrix) in contrast to the closed-loop when a controller is added. In this case we apply a control signal r as an input to the system but first pass it through a controller $K(s)$ which seeks to modify the dynamics of the system in some way, e.g. speeding up slow dynamics of the system or stabilising the system. We then feed-back the output of $G(s)$ into the control signal via negative feedback, so that the input to the controller becomes $r' = r - y$. By "closing the loop" we discover the closed-loop transfer function,

$$\frac{K(s)G(s)}{1 + K(s)G(s)}. \tag{4.6}$$

The closed-loop system is unstable when $K(s)G(s) = -1$, i.e. when it has unity gain and a π phase delay. One crucial part of designing a controller is considering the gain margin: the difference between the actual gain and unity gain at the π phase shift; and the phase margin: the difference between the actual phase and π at the unity gain. If one of these is too small then fluctuations in the physical parameters determining $K(s)$ or $G(s)$ could cause the closed-loop system to become unstable.

4.2 Transmission-readout setup

As discussed in sections. 3.2 and 5.1.2, the Laplace-domain transfer function for the unstable filter is given by,

$$G(s) = \frac{s - \gamma_{\text{neg}}}{s + \gamma_{\text{neg}}}, \tag{4.7}$$

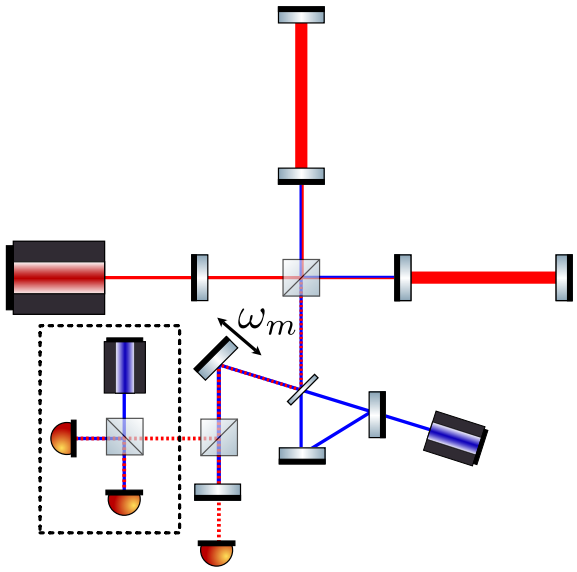

Figure 4.2 The transmission readout setup discussed in Section. 3.3 augmented with a heterodyne readout shown in the black dashed box. A small part of the output beam is picked off with a low reflectivity beamsplitter, and mixed with a local oscillator offset by the mechanical oscillator frequency, allowing the observation of both quadratures of the mirror displacement.

and so since the system has a simple pole at $s = -\gamma_{\text{neg}}$ it is unstable. This means that when used in isolation or used as a coherent feedback filter in a quantum measurement device as shown in Figure. 3.1 (a) a stabilising controller must be used as shown in [5].

As discussed in Section. 3.3, the transmission-readout setup shown in Figure. 3.1 (b) is somewhat less intuitive as the unstable filter does not exist as a separate black-box device within the setup, but rather is integrated within the system. Regardless, as shown in Section. 3.3.1 for the parameters used the system is still dynamically unstable.

First, we consider the unstable case where $g > \omega_s$. Similarly to the

reflection-readout case considered in [5] the system will not be controllable if we use homodyne measurement and only measure the phase quadrature since only one of the two quadratures of the suspended mirror will be observed. Therefore, as shown in Figure. 4.2, we pick off a small part of the output signal for control purposes and use heterodyne measurement to measure both mirror quadratures. In contrast to the reflection-readout case, we measure the SRC mode $\hat{a}$ and so the readout vector is $\mathbf{D} = (1, 0, 0)$, while the control input vector $\mathbf{B} = (0, 1, 0)^T$ remains the same, i.e. it is linear to $\hat{b}^\dagger$. The observability and controllability matrices are defined respectively by,

$$U_o = \begin{bmatrix} C \\ CA \\ CA^2 \\ \vdots \\ CA^{n-1} \end{bmatrix}, \tag{4.8}$$

and,

$$U_c = \begin{bmatrix} B & AB & A^2B & \cdots & A^{n-1}B \end{bmatrix}, \tag{4.9}$$

where n is the number of states. Since both matrices are full rank the system is controllable and observable [53], and so the stabilising controller (from $\hat{a}$ to $\hat{b}^\dagger$) may be immediately written down as shown in [5].

Now, let us consider the case where $g = \omega_s$; specifically, when g approaches ω_s from below, the system will be stable. Interestingly, as seen in Eq. (3.27), the signal response at DC is infinite so long as the upper mechanical sideband about $\omega_0 + 2\omega_m$ is neglected.

4.3 Local Control

One concern of the above control schemes is the time delay between the readout and the applied control. It is well known that time delays affect the maximum allowed controller gain before the system begins to self-oscillate [53], as well as reducing the phase margin of the stabilised system. In our case, this becomes a problem when the mechanically suspended mirror of the unstable filter is placed far away from the readout port. For example, in the reflection-readout setup the unstable filter can be placed on the ends of the arm cavities. In a 20 km arm-length there is a minimum time delay of 66 µs between the control signal and the readout, which could become significant especially if high feedback gains are required.

One solution, as shown in Figure. 3.6, is to use a local sensing laser to directly measure the displacement of the mechanically oscillating mirror, and then use a feedback loop to control the mirror, while still also reading out at the main port of the interferometer. The control force $f_c(t)$ can be applied, for example, by modulating the amplitude of the local sensing laser to produce a radiation pressure force at the mirror.

Unfortunately, introducing the local sensing laser injects a significant amount of extra quantum noise from the laser. Altogether we have the input vacuum fluctuations at the dark port n_1, the radiation pressure noise due to the random fluctuations of the local sensing laser power n_2, and the local sensing laser noise n_3. However, in post-processing we can cancel out the local sensing noise by minimising the noise power to recover the bandwidth-enhanced sensitivity. Since it is performed in post-processing the time delay between

the local sensing readout and the main readout is no longer relevant. This process is effectively a matched filter, since we are using our full knowledge of the noise coupling and spectral densities to design a filter perfectly cancelling the noise. For an overview of matched filtering see, for example, the appendix of [55].

There are now two readouts, the main readout s_1, and the local sensing readout s_2, both of which include the GW strain signal h. We assume that the two readouts are linear combinations of the GW strain signal and the noise sources,

$$s_1 = \xi_0 h + \sum_{i=1}^{3} \xi_i n_i, \quad s_2 = \eta_0 h + \sum_{i=1}^{3} \eta_i n_i. \tag{4.10}$$

where we have prior knowledge of the transfer functions $\xi_i, \eta_i, i = 0 \ldots 3$. We then combine the two readouts to give the optimal estimate via the coefficients k_1, k_2,

$$s = k_1 s_1 + k_2 s_2. \tag{4.11}$$

Next, we assert that the coefficients are normalised with respect to the GW strain coefficients,

$$k_1 \xi_0 + k_2 \eta_0 = 1 \implies k_1 = \frac{1}{\xi_0}(1 - k_2 \eta_0). \tag{4.12}$$

The optimal estimate therefore becomes,

$$s = h + \sum_{i=1}^{3} (k_1 \xi_i + k_2 \eta_i) n_i = \text{signal} + \text{noise}, \tag{4.13}$$

and the total noise power is then given by,

$$\sum_{i=1}^{3} S_{ii} |k_1 \xi_i + k_2 \eta_i|^2, \tag{4.14}$$

where S_{ii} is the power spectral density of noise source n_i. This is equal to the reciprocal of the signal-to-noise ratio (SNR), i.e. it is the noise-to-signal ratio (NSR), because of the normalisation in eq. (4.12).

We now minimise eq. (4.14) with respect to the coefficient k_2, subject to the constraint of eq. (4.12). This can be done by substituting for k_1 in terms of k_2, differentiating by k_2, and then setting to zero, yielding,

$$k_2^* = -\frac{\sum_{i=1}^{3} \left(\frac{\xi_i^*}{\xi_0^*}\right) \left(\eta_i - \eta_0 \frac{\xi_i}{\xi_0}\right) S_{ii}}{\sum_{i=1}^{3} \left(\eta_i - \eta_0 \frac{\xi_i}{\xi_0}\right) \left(\eta_i^* - \eta_0^* \frac{\xi_i^*}{\xi_0^*}\right) S_{ii}}. \tag{4.15}$$

By combining the readouts with the above equation we can completely recover the bandwidth-enhanced sensitivity while controlling the unstable filter. We can also reduce the local sensing laser power arbitrarily to reduce the back-action noise and increase the local sensing noise, limited only by the local sensing laser needing enough sensitivity to be able to detect the mirror motion, since we can subtract out the local sensing noise to an arbitrary degree. However, its implementation in a setup such as shown in Figure. 3.6 is a question of ongoing research, for example both upper and lower sidebands need to be observed by the local sensing laser and processed by the controller to be stabilised. Therefore the control scheme demonstrated in the aforementioned figure may not realise the necessary control.

Chapter Five

Frequency-domain quantum network synthesis

This chapter contains content from the second paper listed at the beginning of the thesis and is published at Phys. Rev. A **103**, 013707 [56] the entirety of which was written by the first author Joe Bentley.

In this chapter we will detail a novel set of techniques for the synthesis of quantum systems directly from their frequency domain transfer functions. The primary motivation arises from the synthesis of classical networks. For example, as shown in [10] it is trivial to construct a physical realisation of any set of linear classical state-space (A, B, C, D) simply by using a mixture of feedback and integrators (i.e. resistors and operational amplifiers), which begs the question of whether or not this would be possible for quantum systems, such as are relevant in high-precision measurements. This is in stark contrast to conventional methods for developing such systems which instead rely on physical intuition and experimentation to produce any desired behaviour,

which limits the complexity of systems we can design to our understanding of such systems.

Quantum systems propose unique constraints compared to classical systems. Most notably, any Hamiltonian evolution of the system via the system's dynamical equations must preserve all the commutation relations of the system, which leads to constraints on the possible state-space representations. In section. 5.1.1 we give a detailed analysis of how to achieve this for a system with one internal degree-of-freedom.

5.1 Applying network synthesis to high-precision measurements

In high-precision measurements, our understanding of physics is predominantly limited by quantum noise, arising due to the fundamental quantum fluctuations of the probing fields [57, 58, 19, 40]. This is particularly true for laser interferometric gravitational-wave detectors [59] where the quantum shot noise dominates at high frequencies due to the positive dispersion of the arm cavities [60]. Quantum and classical noises are also limiting factors in quantum optomechanical experiments [17, 41] and searches for new physics using an interferometer [1, 2]. To achieve a maximal signal-to-noise ratio, it is essential to engineer the frequency-dependent response of the measurement devices depending on the frequency content of the signal being measured. For example, advanced gravitational wave detectors are tuned to have maximum sensitivity in a frequency range containing the binary black hole inspiral waveform, how-

ever not all of the binary neutron star inspiral waveform is observed [25]. Quantum filters are designed to engineer this response. As illustrated in Fig. 5.1, there are three ways that the measurement device can be augmented with quantum filters. First, the input filter, coupling the noise input to the probe degrees of freedom, shapes how the quantum fluctuations enter the device. Next, the coherent feedback filter, coupled to the probe degrees of freedom and input-output fields, modifies the dynamics of the probe [8, 61, 62, 63]. This can enhance the response to the signal of interest when the quantum system is converted into a probe coupled to a classical signal. Finally, the output filter, coupling the probe degrees of freedom to the readout port, modifies the response of readout to the detector's output field. As a simple example, an optical Fabry-Perot cavity is used as an input filter for implementing frequency-dependent squeezed light [4, 64, 65].

Until now, formulating a physical realisation of a given quantum filter with a desired frequency response required a combination of intuition and prior experience, making more complicated frequency responses difficult to engineer. As first introduced in [8] and further discussed in [66][67, Chapter 2] we use the concept of physical realisability which tells us whether a given time-domain state-space representation of the system obeys quantum mechanics. An important observation comes from comparing the state-space representation of the system and its counterpart representation as a frequency-domain transfer matrix, specifically that the mapping from the system's transfer matrix to a state-space representation is not unique, in fact many different state-space representations are possible. Therefore requiring that the state-space is phys-

ically realisable sets a significant constraint on the range of this mapping. We can then choose a state-space chosen from the range and transform it to one which is physically realisable to infer the actual physical dynamics. Using this technique, in this paper we now present an approach to systematically realising quantum filters for high-precision measurements directly from their frequency-domain transfer matrices. This technique builds upon a general formalism for describing linear stochastic quantum networks and the synthesis of such networks, recently developed by the quantum control community [68, 8, 66, 69, 70, 71, 10, 72, 73, 74, 75, 67, 76, 77]. It has powerful implications on how active quantum filters are designed, making the realisation of filters with arbitrarily complicated frequency responses a possibility. Since in principle we can view the entire measurement device as a many degrees-of-freedom quantum filter, this approach also provides a new paradigm for designing optimal quantum measurement devices.

5.1.1 Direct approach

We now provide the details of the approach. The process to find a physical realisation, e.g. an optical layout and its associated parameters, from a given set of transfer functions is general to multi-input multi-output lossless linear quantum systems; losses and other noise sources can be added later by augmenting the system description. Our starting point is the frequency-domain transfer function matrix, which is the square matrix that relates the frequency-domain

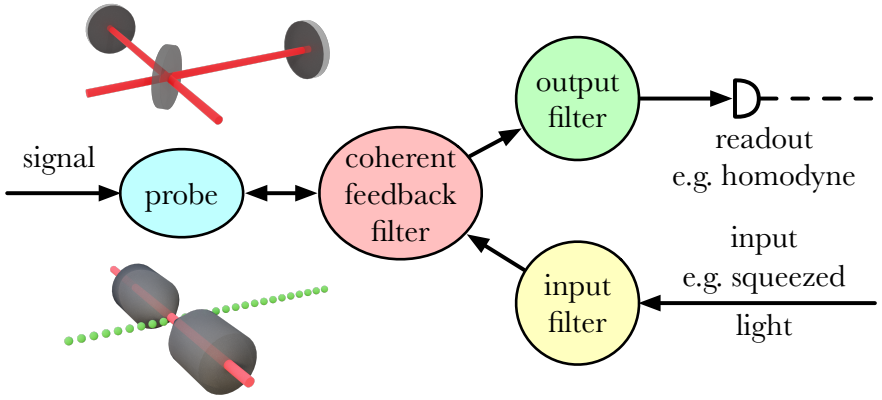

Figure 5.1 Flowchart illustrating the different places quantum filters can be used within a quantum measurement device. We consider a generic device consisting of a probe (e.g. a mirror-endowed test mass or an atomic ensemble) coupled to some classical signal, which receives an input (e.g. non-classical squeezed light) and whose output field is measured by the readout scheme (e.g.homodyne readout).

system outputs $\mathbf{y}(s)$ to its inputs $\mathbf{u}(s)$:

$$\mathbf{G}(s) = C(-sI - A)^{-1}B + D, \tag{5.1}$$
$$\mathbf{y}_i(s) = \sum_j G_{ij}(s)\mathbf{u}_j(s),$$

where (A, B, C, D) are the system matrices as defined below, and I is the identity matrix, and we assume that the number of inputs is equal to the number of outputs. Here the Laplace transform is defined as $f(s) = \int_{0^-}^{\infty} e^{+st} f(t)\mathrm{d}t$, with the lower bound at $t = 0^-$ so that an impulse can be added at $t = 0$. For a given transfer matrix a non-unique state-space representation can be found of the form [78, 79, 80, 81]:

$$\dot{\mathbf{x}} = A\,\mathbf{x} + B\,\mathbf{u}, \tag{5.2}$$
$$\mathbf{y} = C\,\mathbf{x} + D\,\mathbf{u}, \tag{5.3}$$

which is a *non-unique* time-domain representation of the system's dynamics. Here the quantity $\mathbf{x} \in \mathbb{L}^{2n\times 1}$ ($\mathbb{L}$ being the space of linear operators on the relevant Hilbert space $\mathcal{H}$) is a vector of conjugate operator pairs representing the internal n degrees of freedom of the system, $\mathbf{u} \in \mathbb{L}^{2m\times 1}$ is the vector of m system inputs, and $\mathbf{y} \in \mathbb{L}^{2m\times 1}$ is the vector of m system outputs. Note that in a quantum mechanical state-space, two conjugate operators are used to represent each individual degree of freedom of the system hence the factors of 2. In the context of quantum optomechanics, $\hat{x}$ represents the cavity/oscillator eigenmodes for the cavities and mechanical oscillators in the system, while $\hat{u}$ and $\hat{y}$ are continuous Bosonic fields in free space [18, 10]. The dynamical matrix $A \in \mathbb{C}^{2n\times 2n}$ describes the internal dynamics of the system, the input matrix $B \in \mathbb{C}^{2n\times 2m}$ describes the coupling of the input into the system, the output matrix $C \in \mathbb{C}^{2m\times 2n}$ describes the coupling of the system to the output, and the "direct-feed" matrix $D \in \mathbb{C}^{2m\times 2m}$ describes the coupling of the input directly to the output. (A, B, C, D) are together called the *system matrices* and fully describe the linear dynamics of the system.

The system is called *physically realisable* (and a corresponding physical realisation can be designed) if, in the Heisenberg picture evolution of the system, the commutation relations are preserved [8]:

$$\forall i, j \quad \mathrm{d}[\mathbf{x}_i, \mathbf{x}_j] = 0, \quad [\mathbf{y}_i(t), \mathbf{y}_j^\dagger(t')] = \delta(t - t')\delta_{ij}, \tag{5.4}$$

where the differential is treated using the quantum Itô rule, meaning that the cross-products of the differentials of the operators must be calculated [82, 16, 83]. The conditions on the system matrices for all such evolutions to preserve these commutation relations are found by using Eqs. (5.2) and (5.3)

to calculate the increment of the system state $\mathrm{d}\mathbf{x}_i$ in Eq. (5.4) for an infinitesimal time period $\mathrm{d}t$. For an n degree-of-freedom system described using complex mode operators (as are usually used in quantum optics) such that $\mathbf{x} = (\hat{a}_1, \hat{a}_1^\dagger; \ldots; \hat{a}_n, \hat{a}_n^\dagger)^T$ with m inputs and outputs described by $\mathbf{u} = (\hat{u}_1, \hat{u}_1^\dagger; \ldots; \hat{u}_m, \hat{u}_m^\dagger)^T$ and similarly for $\mathbf{y}$, the constraints on the system matrices are given by

$$AJ + JA^\dagger + BJ_mB^\dagger = 0, \tag{5.5}$$

$$JC^\dagger + BJ_mD^\dagger = 0, \tag{5.6}$$

$$DJ_mD^\dagger = J_m, \tag{5.7}$$

where $J = \mathrm{diag}(1, -1; \ldots; 1, -1) \in \mathbb{R}^{2n\times 2n}$ and $J_m = \mathrm{diag}(1, -1; \ldots; 1, -1) \in \mathbb{R}^{2m\times 2m}$[1]. See Appendix A of [66] for a proof of these constraints. So now we have a restriction on the possible system matrices that can lead to a physically realisable system.

Now we consider how to generate such a physically-realisable state-space model from the system's transfer matrix. The conventional procedure for transforming the transfer matrix to a minimal state-space model is outlined in Refs. [78, 80]. Such a state-space model constructed from a pole-zero form transfer matrix is minimal if the number of internal degrees of freedom (e.g. the number of pairs of conjugate ladder operators describing the system state) is equal to the highest polynomial order in the frequency s among all of the transfer functions in the transfer matrix. Generally such a procedure will lead

[1] As discussed in Appendix. C.1, this matrix takes a different form when using Hermitian observable quadrature operators.

to system matrices (A', B', C', D') that do not satisfy Eqs. (5.5) and (5.6) and therefore cannot be physically realised. Here we can construct a method allowing us to transform (A', B', C', D') to a physically realisable counterpart (A, B, C, D), given that the transfer matrix $\mathbf{G}(s)$ obeys a condition that will be given in Eq. (5.13). To achieve we assume that there exists a Hermitian matrix X which satisfies the following equations,

$$A'X + X(A')^\dagger + B'J_m(B')^\dagger = 0, \tag{5.8}$$

$$X(C')^\dagger + B'J_m(D')^\dagger = 0. \tag{5.9}$$

If we can write $X = TJ_mT^\dagger$, then this can be substituted into the above equations to give,

$$A'TJ_mT^\dagger + TJ_mT^\dagger(A')^\dagger + B'J_m(B')^\dagger = 0, \tag{5.10}$$

$$TJ_mT^\dagger(C')^\dagger + B'J_m(D')^\dagger = 0. \tag{5.11}$$

This matrix T can be used to transform the state-space via the canonical state-space transformation,

$$A = T^{-1}A'T,\ B = T^{-1}B',\ C = C'T,\ D = D'. \tag{5.12}$$

If we then invert these equations and substitute into Eqs. (5.10) and (5.11) then we recover the physically realisability Eqs. (5.5) and (5.6). Therefore this matrix T transforms the physically unrealisable state-space (A', B', C', D') into a realisable state-space (A, B, C, D).

The existence of T is guaranteed by the symplectic condition imposed on any physically realisable transfer matrix $\mathbf{G}(s)$ and direct-feed matrix D [9]:

$$\mathbf{G}^\dagger(s^*)J_m\mathbf{G}(-s) = J_m. \tag{5.13}$$

Now that we have shown how to obtain the physically realisable state-space model (A, B, C, D) from the transfer matrix obeying Eq. (5.13) we can infer the physical realisation. We describe the realisation chiefly using the generalised open oscillator [10] formalism. This is a general formalism describing open quantum systems with arbitrary internal linear dynamics and input-output couplings, providing a language for describing and analysing systems with internal degrees of freedom coupled to external continuum fields, such as quantum measurement devices and quantum filters. As shown in [8] for an n degree-of-freedom system, when the direct-feed matrix D is symplectic and unitary (i.e. it satisfies (5.7) and $D^\dagger D = DD^\dagger = I$), there is a one-to-one correspondence between the system matrices (A, B, C, D) and the generalised open oscillator which is parameterized by a triplet $(S, \hat{L}, \hat{H})$ [10, 70, 71]. Here, the scattering matrix $S \in \mathbb{C}^{m\times m}$ describes the transformation of the input fields through a passive network, i.e. any passive pre-processing of the system's input fields. The coupling operator $\hat{L} = K\mathbf{x}$ where $K \in \mathbb{C}^{m\times 2n}$ describes the coupling between the input and output fields and the internal degrees of freedom, e.g. equivalent to the usual input-output Langevin equations [17] when the input-output fields are coupled to the internal fields by a mirror. The Hamiltonian $\hat{H}$ describes the free evolution of the internal system dynamics as if the system were closed. The relation between the system matrices and the generalised open oscillator parameters is given by,

$$\begin{aligned} &S = [D_{2k-1,2l-1}]_{k,l=1,2\ldots,m}, \\ &\hat{L} = \begin{bmatrix} I_m & 0 \end{bmatrix} P_m C\,\mathbf{x}, \quad \hat{H} = \mathbf{x}^\dagger \frac{i}{4}\hbar \left(JA - A^\dagger J\right)\mathbf{x}, \end{aligned} \tag{5.14}$$

where I_m is an identity matrix, P_m is the permutation matrix that maps $\mathbf{u} =$

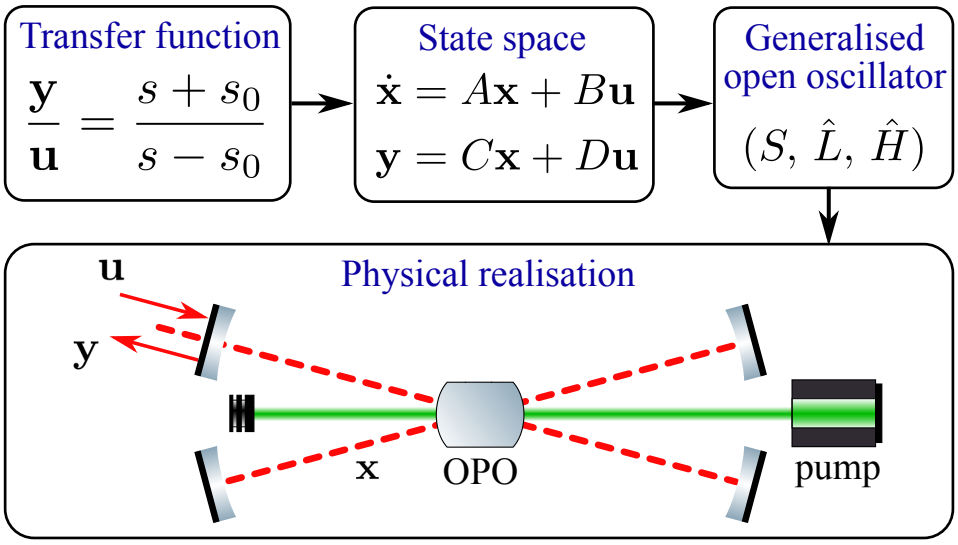

Figure 5.2 Flowchart showing the steps in constructing the physical realisation of a quantum filter; an active filter is used as an illustration.

$(\hat{u}_1, \hat{u}_1^\dagger; \ldots; \hat{u}_m, \hat{u}_m^\dagger)^T$ to $(\hat{u}_1, \hat{u}_2, \ldots, \hat{u}_m, \hat{u}_1^\dagger, \hat{u}_2^\dagger, \ldots, \hat{u}_m^\dagger)^T$, and $\hat{H}$ is derived in Appendix. C.1. The total Hamiltonian is then given by, [10]

$$\hat{H}_{\text{tot}} = \hat{H} + i\hbar[\ \hat{L}^\dagger \quad -\hat{L}^T\ ]\mathbf{u}, \tag{5.15}$$

where the input fields $\mathbf{u}$ are pre-processed by the static passive network described by S. Now we have achieved the full physical Hamiltonian describing the system starting from the transfer matrix describing the frequency-domain input-output behaviour.

In the case where only one of the internal degrees of freedom is coupled to the input-output fields it could be trivial from the Hamiltonian to construct the physical realisation by inspection, however this is not always the case. Systems consisting of more than one internal degree-of-freedom can first be sub-divided into separate one degree-of-freedom systems coupled via direct interaction Hamiltonians via the main synthesis theorem proved in [10]. These

systems can then be systematically realised by connecting the individual one degree-of-freedom systems in series, and overlapping them accordingly, giving a systematic way to construct the physical realisation regardless of complexity [2]. In the below example however this will not be required as the unstable filter only has one internal degree of freedom.

We will now outline the general approach to constructing the physical realisation given an n degree-of-freedom generalised open oscillator as developed in [10]:

1. First, the main synthesis theorem is used to split the n degree-of-freedom oscillator into n one degree-of-freedom oscillators which are connected in series, i.e. the output of each oscillator is fed into the input of the next, and also a direct interaction Hamiltonian is produced coupling the oscillators. The task is then to realise each of these one degree-of-freedom oscillators and the direct interaction Hamiltonian.

2. For each one degree-of-freedom oscillator we do the following. First the scattering matrix can be realised as a static passive linear network using only beamsplitters and mirrors. Then, the general coupling operator of the form $\hat{L} = \alpha\hat{a} + \beta\hat{a}^\dagger$ can be realised by indirectly coupling the mode $\hat{a}$ to the external continuum fields $\hat{u}$ and $\hat{y}$ via an auxiliary mode $\hat{b}$, which has sufficiently fast dynamics with coupling rate γ such that it can be adiabatically eliminated from the final input-output relation. This auxiliary mode is coupled to the main mode via non-linear crystal

[2]Note that the approach is also entirely general to optomechanical systems, provided that the dynamics can be linearised.

(two-mode squeezing process) for the $\beta\hat{a}^\dagger$ term, and via a beamsplitter for the $\alpha\hat{a}$ term. These are related to the physical parameters via $\alpha = -\epsilon_2^*/\sqrt{\gamma}$ where $\epsilon_2 = 2\Theta e^{-i\Phi}$ where Θ is the beamsplitter mixing angle and Φ is the relative phase detuning introduced by the beamsplitter, and $\beta = \epsilon_1/\sqrt{\gamma}$ where ϵ_1 is the effective pump intensity, shown to be equal to $cr/(2L)$ in the supplemental material, where r is the single-pass squeezing factor and L is the cavity length. Finally, the Hamiltonian $\hat{H}$ can be realised in the most general case as a detuned DPA (degenerate parametric amplifier), which can be implemented as a detuned cavity with a $\chi^{(2)}$ non-linear crystal with a pump frequency twice the laser carrier frequency ω_0. Specifically to realise the Hamiltonian $\hat{H} = \hbar\Delta\hat{a}^\dagger\hat{a} + \hbar\frac{i}{2}(\epsilon(\hat{a}^\dagger)^2 - \epsilon^*\hat{a}^2)$ we use a cavity with resonant frequency $\omega_{\text{cav}} = \omega_0 + \Delta$ where ω_0 is the laser carrier frequency and a non-linear crystal with effective pump intensity $\epsilon = cr/(2L)$ where again r is the single-pass squeezing factor and L is the cavity length.

3. To implement the interaction Hamiltonian between each one degree-of-freedom oscillator we overlap the relevant internal modes of each oscillator via a non-linear crystal and/or beamsplitter depending on the interaction. The interaction Hamiltonian between modes $\hat{a}_k$ and $\hat{a}_l$ can be written in the form $\hat{H}_{kl} = \hbar(\epsilon_2\hat{a}_k^\dagger\hat{a}_l + \epsilon_2^*\hat{a}_k\hat{a}_l^\dagger + \epsilon_1\hat{a}_k^\dagger\hat{a}_l^\dagger + \epsilon_1\hat{a}_k\hat{a}_l)$ where in this case the effective pump intensity is $-2i\epsilon_1$, and again $\epsilon_2 = 2\Theta e^{-i\Phi}$ where Θ is the mixing angle and Φ is the relative phase difference between the two modes. In the unstable filter example below we do not need to do this as we already only have one internal degree of freedom.

In summary, from the input-output transfer matrix we have developed the physical parameters describing the system. The procedure is summarised in Fig. 5.2.

5.1.2 Illustrative example: an unstable filter

To demonstrate the power of this approach, we will go beyond passive optical cavities by considering a non-trivial active filter for beating the universal gain-bandwidth product limit in resonant detection schemes [26, 84, 28, 30, 31, 33, 5, 85, 60, 52, 22, 32, 34, 86, 87], specifically, the so-called unstable filter [5] which has a broadband anomalous (negative) dispersion. The gain-bandwidth product, also known as the Mizuno limit [23], states that the integral of the squared frequency-domain signal transfer function for a resonant detector is bounded purely by the energy stored in the detector. Therefore, when considering the quantum shot noise due to the input quantum vacuum, the detection bandwidth and peak sensitivity are inversely proportional which cannot be surpassed by changing any physical parameter other than the power in the detector. One way this can be surpassed is by using the broadband anomalous dispersion of the aforementioned unstable filter to partially negate the positive dispersion of the detector's signal cavity as first discussed in [5]. The filter also is unusual because it seemingly violates the Kramers-Kronig relations which imply that a stable anomalous dispersion filter without absorption (i.e. with unity gain over the range of the anomalous dispersion) violates causality, however since this system is dynamically unstable this restriction does not apply [88, 89, 90, 91]. As discussed in the procedure above we start with the

frequency-domain transfer function of the unstable filter,

$$G(s) = \frac{s - s_0}{s + s_0}, \tag{5.16}$$

where $s \equiv i\omega$ and $s_0 = \gamma_{\text{neg}}$ is a characteristic frequency quantifying the anomalous (negative) dispersion. An example will now infer a physical realisation for this device using the above procedure.

First we note that since the transfer function is first order in frequency s, only one internal degree of freedom will be required for the minimal state-space realisation. Therefore the system state vector $\hat{x}$ will have two elements: $\mathbf{x}_1 = \hat{a}, \mathbf{x}_2 = \hat{a}^\dagger$ describing a single cavity mode, and similarly for the vectors $\mathbf{u}$ and $\mathbf{y}$ describing the input and output modes respectively. As a transfer-function matrix, Eq. (5.16) can be written as

$$\mathbf{G}(s) = \frac{s - s_0}{s + s_0} \begin{bmatrix} 1 & 0 \\ 0 & 1 \end{bmatrix}, \tag{5.17}$$

which can be verified to satisfy the constraint (5.13) and therefore a corresponding physical realisation can be found. To simplify the notation, we define a dimensionless s (and the corresponding time) which is normalised with respect to $s_0/2 = \gamma_{\text{neg}}/2$ (a factor of 2 for convenience), namely $s \to (s_0/2)s$ where s is now dimensionless. A corresponding minimal but not physically realisable state-space model is given by,

$$\begin{bmatrix} \dot{\hat{a}} \\ \dot{\hat{a}}^\dagger \end{bmatrix} = \begin{bmatrix} 2 & 0 \\ 0 & 2 \end{bmatrix} \begin{bmatrix} \hat{a} \\ \hat{a}^\dagger \end{bmatrix} + \begin{bmatrix} \hat{u} \\ \hat{u}^\dagger \end{bmatrix}, \tag{5.18}$$

$$\begin{bmatrix} \hat{y} \\ \hat{y}^\dagger \end{bmatrix} = \begin{bmatrix} 4 & 0 \\ 0 & 4 \end{bmatrix} \begin{bmatrix} \hat{a} \\ \hat{a}^\dagger \end{bmatrix} + \begin{bmatrix} \hat{u} \\ \hat{u}^\dagger \end{bmatrix}. \tag{5.19}$$

The matrix X that solves Eqs. (5.8) and (5.9) is given by $X = -J/4$, which can be written in the form $X = TJT^\dagger$ with the matrix T which transforms the above state-space model to the physically realisable one is given by,

$$T = \frac{1}{2}\begin{bmatrix} 0 & -1 \\ 1 & 0 \end{bmatrix}. \tag{5.20}$$

The resulting state-space model can be found by applying the similarity transformation as shown in Eq. (5.12),

$$A = \begin{bmatrix} 2 & 0 \\ 0 & 2 \end{bmatrix},\ B = \begin{bmatrix} 0 & 2 \\ -2 & 0 \end{bmatrix},\ C = \begin{bmatrix} 0 & -2 \\ 2 & 0 \end{bmatrix},\ D = I, \tag{5.21}$$

which obey Eqs. (5.5) and (5.6) by construction and therefore is s physically realisable state-space model.

Eq. (5.14) can now be used to calculate the scattering matrix, input-output coupling, and internal Hamiltonian for the unstable filter. We have

$$S = I,\ K = \begin{bmatrix} 0 & -2 \end{bmatrix},\ \hat{H} = 0. \tag{5.22}$$

This implies that there is no input scattering with $S = I$, and $\hat{L} = -2\hat{a}^\dagger$, and there is no detuning or internal squeezing of the cavity mode as $\hat{H} = 0$.

Since $\hat{H}$ and S are trivial to implement we now implement the coupling operator $\hat{L} = -2\hat{a}^\dagger$ as discussed above. In this case we have $\alpha = 0$, and so just have the auxiliary mode coupled to the main cavity mode via a non-linear crystal. This auxiliary mode will later be adiabatically eliminated, however it makes the physical realisation more feasible as coupling two cavity modes via a parametric oscillator is more experimentally durable. Therefore we construct

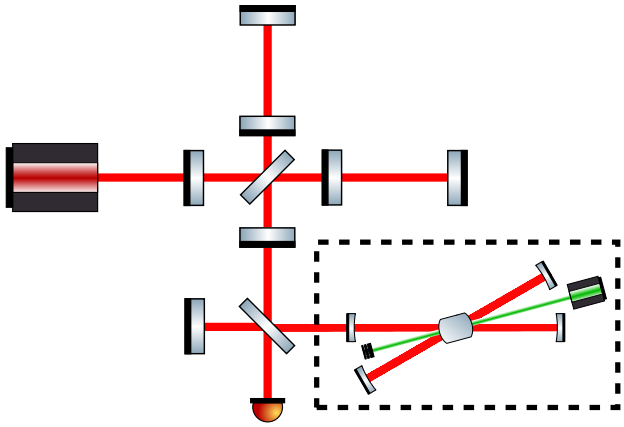

Figure 5.3 Diagram showing where the filter realisation (highlighted by the shaded box) would be integrated into a standard Michelson inteferometer, using a scheme similar to that proposed in Ref. [5], which improves the signal response at high frequencies via the negative dispersion compensating the positive dispersion of the arm cavities as discussed above.

the physical realisation shown in Fig. 5.2, which can be integrated into an interferometer as shown in Fig. 5.3.

The realisation simply consists of two tuned cavities (the main mode $\hat{a}$ and the auxiliary mode $\hat{b}$) coupled via a $\chi^{(2)}$ non-linear crystal, labelled OPO (optical parametric oscillator), pumped by a classical pump field, labelled pump. One of the cavities is coupled to the external fields. Specifically, we have

$$\hat{H}_{ab} = -\hbar\sqrt{s_0\,\gamma}(\hat{a}^\dagger\hat{b}^\dagger + \hat{a}\hat{b})\,, \tag{5.23}$$

$$\hat{H}_{\rm ext} = -i\hbar\sqrt{\gamma}(\hat{b}\,\hat{c}^\dagger_{\rm ext} - \hat{b}^\dagger\hat{c}_{\rm ext})\,. \tag{5.24}$$

The interaction Hamiltonian $\hat{H}_{ab}$ describes the coupling of both cavity modes $\hat{a}$ and $\hat{b}$ via the OPO. As shown in Appendix. C.2, the coupling rate $\sqrt{s_0\,\gamma}$ is equal to $rc/(2L_b)$, where r is the single-pass squeezing factor of the crystal

and L_b is the length of the auxiliary cavity. As an order of magnitude estimate for implementation in a laser interferometer with arm length of $L_{\text{arm}} = 4\,\text{km}$ (where $s_0 \equiv \gamma_{\text{neg}} = c/L_{\text{arm}}$ [5]), the required squeezing factor is

$$r = 7.7 \times 10^{-5} \sqrt{\frac{T_b}{100\,\text{ppm}}} \sqrt{\frac{L_b}{24\,\text{cm}}} \sqrt{\frac{4\,\text{km}}{L_{\text{arm}}}}. \tag{5.25}$$

The Hamiltonian $\hat{H}_{\text{ext}}$ describes the coupling between the auxiliary mode $\hat{b}$ and the external continuum field $\hat{c}_{\text{ext}}$, which is related to the input and output operators via $\hat{u} \equiv \hat{c}_{\text{ext}}(t = 0_-)$ and $\hat{y} \equiv \hat{c}_{\text{ext}}(t = 0_+)$ [11, 17]. The coupling rate γ is defined as $T_b c/(4L_b)$ where T_b is the input mirror transmissivity. The negative dispersion transfer function shown in Eq. (5.16) can then be recovered by solving the resulting Heisenberg equations of motion in the frequency domain, and then applying the approximation $\gamma \gg \omega$, the so-called "resolved-sideband regime", which effectively adiabatically eliminates $\hat{b}$ [10].

In Appendix. C.3, we include the effect of optical loss for the realistic implementation. We found that the noise contribution from the auxiliary cavity loss is insignificant compared to the contribution from the $\hat{a}$ cavity loss. The resulting input-output relation including the optical loss is given by

$$\hat{y}(s) \approx \frac{\omega + i(\gamma_a^\epsilon + s_0)}{\omega + i(\gamma_a^\epsilon - s_0)} \hat{u}(s) + \frac{2\sqrt{s_0\,\gamma_a^\epsilon}}{\omega + i(\gamma_a^\epsilon - s_0)} \hat{n}_a^\dagger(s), \tag{5.26}$$

where $\gamma_a^\epsilon = \epsilon_a c/(4L_a)$ with ϵ_a being the total optical loss in the $\hat{a}$ cavity and L_a being the cavity length, and $\hat{n}_a$ is the corresponding vacuum noise process. The distortion of the transfer function due to γ_a^ϵ is on the order of γ_a^ϵ/s_0, while the noise term is on the order of $\sqrt{\gamma_a^\epsilon/s_0}$ and is therefore more significant.

The above input-output relation takes the same form as the optomechanical case [5] if we view $\hat{n}_a$ as the thermal noise of the mechanical oscillator. In

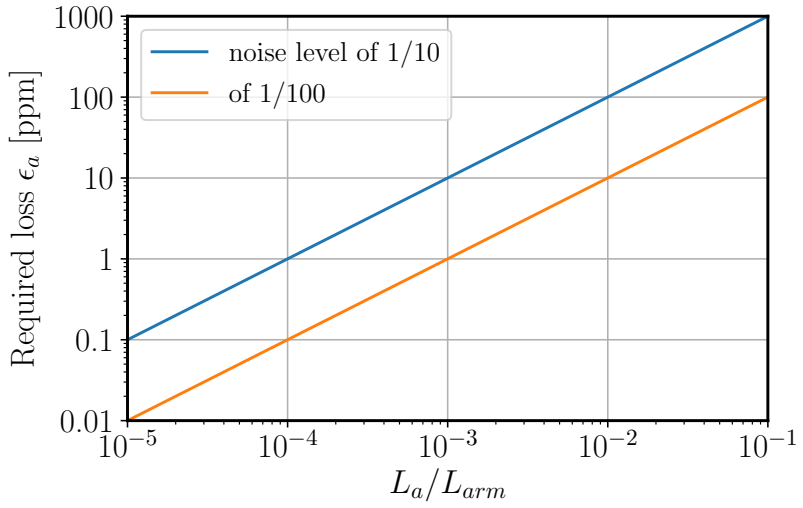

Figure 5.4 Required total $\hat{a}$ cavity loss ϵ_a as a function of ratio of $\hat{a}$ cavity length to arm cavity length L_a/L_{arm} for the cases where the noise power contribution at $\omega = 0$ due to $\hat{n}_a$ is a tenth of that of the signal power (blue line) and a hundred (orange line).

contrast, in this case the loss n_a is sourced by the quantum vacuum and so it only has vacuum fluctuations, equivalent to a mechanical oscillator at environmental temperature $T_{\text{env}} = 0$. Therefore the strict thermal requirements of the optomechanical unstable filter are avoided. Instead vacuum fluctuations are injected due to losses in the mirrors and the non-linear crystal. The required loss to achieve low noise as a function of $\hat{a}$ cavity length is shown in Fig. 5.4. As we can see, given an interferometer arm length of $L_{\text{arm}} = 4\,\text{km}$, a loss per unit length of $\epsilon_a/L_a = 2.5\,\text{ppm}\,\text{m}^{-1}$ is required to achieve a 1/10 noise contribution, i.e. to have the squared magnitude of the second (loss) term in Eq. (5.26) be a tenth of the first (dark port vacuum) term, which is already achievable with state-of-the-art optics [92, 93].

5.1.3 Discussion

In addition to realising quantum filters with a known transfer function, this approach can also be used to design the optimal high-precision measurement devices, where the optimality is based upon the quantum Cramér-Rao bound [94, 95, 96, 97, 98, 99]. We can view the entire measurement device as a N degree-of-freedom quantum filter, and then tune the filter parameters so as to minimise the quantum Cramér-Rao bound. Therefore, we can construct the most sensitive possible N degree-of-freedom measurement device. This opens up a new paradigm of designing and optimising measurement devices and is worthy of being further explored. We will explore this in detail in Section. 6.

5.2 Example: Internal Squeezing

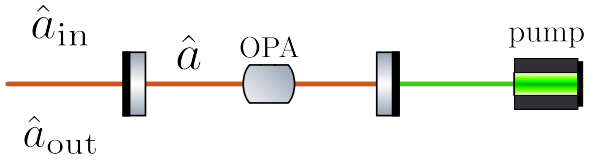

Figure 5.5 The setup for the squeezing of one quadrature via internal squeezing within the cavity. The transformation between the input and output sidebands obeys the J-J unitary condition in Eq. (6.19), however interestingly the quadrature operators $\hat{a}_1, \hat{a}_2$ experience amplification and de-amplification. The OPA (optical parametric amplifier) is pumped by the classical pump beam.

In section. 5.1.2 we considered a diagonal transfer matrix with each element having unity gain. One example of a physical system with a diagonal transfer matrix that does not have unity gain is a cavity with internal squeezing as

discussed in Appendix. C.2 and shown in Figure. 5.5, however in this case it is diagonal in the basis of the quadrature operators,

$$\mathbf{G}_q(i\Omega) = \begin{bmatrix} \frac{\gamma+\sqrt{\gamma s_0}+i\Omega}{\gamma-\sqrt{\gamma s_0}-i\Omega} & 0 \\ 0 & \frac{\gamma-\sqrt{\gamma s_0}+i\Omega}{\gamma+\sqrt{\gamma s_0}-i\Omega} \end{bmatrix}, \tag{5.27}$$

which obeys Eq. (6.19) and so can be physically realised. The top-left element has magnitude greater than unity for $s_0 \neq \gamma$ and so this quadrature is amplified, while the other quadrature is de-amplified by the same amount. Infinite gain at $\Omega = 0$ is achieved in the amplified quadrature when $s_0 = \gamma$. Using Eq. (A.6) we can find the sideband-picture transfer matrix,

$$\mathbf{G}(i\Omega) = \begin{bmatrix} -\frac{\gamma^2+\gamma s_0+\Omega^2}{\gamma s_0-(\gamma-i\Omega)^2} & \frac{2\gamma\sqrt{\gamma s_0}}{-\gamma s_0+(\gamma-i\Omega)^2} \\ \frac{2\gamma\sqrt{\gamma s_0}}{-\gamma s_0+(\gamma-i\Omega)^2} & -\frac{\gamma^2+\gamma s_0+\Omega^2}{\gamma s_0-(\gamma-i\Omega)^2} \end{bmatrix}, \tag{5.28}$$

which obviously also obeys Eq. (5.13). To achieve this we use Mathematica to find an arbitrary unrealisable canonical state-space and then solve Eq. (5.9) to find the matrix X which we then diagonalise into $X = TJT^\dagger$ to find the transformation T to the physically realisable state-space,

$$A = \begin{bmatrix} -\gamma & \sqrt{s_0\gamma} \\ \sqrt{s_0\gamma} & -\gamma \end{bmatrix},\ B = \sqrt{2\gamma}I,\ C = -\sqrt{2\gamma}I,\ D = I, \tag{5.29}$$

where I is the 2×2 identity matrix. Note that the dynamical matrix A has one real positive eigenvalue for $s_0 > \gamma$ and so the system is dynamically unstable in this regime. The corresponding generalised open oscillator $G = (S, \hat{L}, \hat{H})$ is calculated using Eq. (5.14), giving,

$$S = I,\ K = -\sqrt{2\gamma}I,\ R = \frac{i}{2}\begin{bmatrix} 0 & \sqrt{s_0\gamma} \\ \sqrt{s_0\gamma} & 0 \end{bmatrix}. \tag{5.30}$$

The Hamiltonian matrix R is related to the Hamiltonian via $\hat{H} = \mathbf{x}^\dagger R \mathbf{x}$ where $\mathbf{x}$ is the system state vector for the internal degrees of freedom as complex ladder operators. As shown in [10] for a detuned cavity with detuning Δ and effective (complex) pump intensity ϵ the Hamiltonian matrix is given by,

$$R = \frac{1}{2}\begin{bmatrix} \Delta & i\epsilon \\ -i\epsilon^* & \Delta \end{bmatrix}. \tag{5.31}$$

In this case since K is diagonal there is a beamsplitter coupling between the auxiliary mode and the internal mode, and R being off-diagonal tells us that there is a degenerate parametric amplification process within the main cavity with effective pump intensity $\epsilon = \sqrt{s_0\gamma}$. Comparing this with Eq. (C.12) we can see that the effective pump intensity is related to the squeezing factor by,

$$r = \frac{2\epsilon L}{c}, \tag{5.32}$$

where L is the length of the cavity.

The corresponding graphical representation produced by Simba (as discussed in Section. 9.1.1) is shown in Figure. 5.6. Since the auxiliary mode can be adiabatically eliminated, we are left simply with a tuned cavity with internal squeezing and hence we recover the setup shown in Figure. 5.5.

From the physical realisation we calculate the quadrature picture transfer matrix from the inputs to the internal degree of freedom,

$$\begin{bmatrix} \hat{a}^1 \\ \hat{a}^2 \end{bmatrix} = \begin{bmatrix} -\frac{\sqrt{2}\sqrt{\gamma}}{\gamma - \sqrt{\gamma s_0} + i\Omega} & 0 \\ 0 & -\frac{\sqrt{2}\sqrt{\gamma}}{\gamma + \sqrt{\gamma s_0} + i\Omega} \end{bmatrix} \begin{bmatrix} \hat{a}^1_{\text{in}} \\ \hat{a}^2_{\text{in}} \end{bmatrix}, \tag{5.33}$$

where $\hat{a}^1_{\text{in}}$ and $\hat{a}^2_{\text{in}}$ are the input amplitude and phase quadratures respectively, and $\hat{a}^1$ and $\hat{a}^2$ are the quadratures for the internal degree of freedom. For

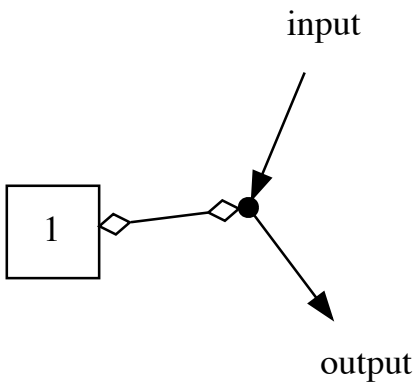

Figure 5.6 A graph representation of the internal squeezing system. The input field is $\hat{a}_{\text{in}}$, which couples into the auxiliary degree of freedom which can be adiabatically eliminated as discussed in Section. 5.1.2. The diamond arrow denotes a beamsplitter-like coupling between mode 1 and the auxiliary mode. The main mode 1 has a square shape which denotes internal squeezing without detuning.

$s_0 = \gamma$, as mentioned above, we expect an infinite gain and thus the SNR as defined in Eq. (6.16) should diverge. In this case the quadrature transfer matrix is given by,

$$\begin{bmatrix} \hat{a}^1 \\ \hat{a}^2 \end{bmatrix} = \begin{bmatrix} \frac{i\sqrt{2}\sqrt{\gamma}}{\Omega} & 0 \\ 0 & -\frac{\sqrt{2}\sqrt{\gamma}}{2\gamma+i\Omega} \end{bmatrix} \begin{bmatrix} \hat{a}^1_{\text{in}} \\ \hat{a}^2_{\text{in}} \end{bmatrix}. \tag{5.34}$$

Indeed, we see that the SNR diverges for the amplitude quadrature, while the SNR for the phase quadrature is π and so is constrained by the Mizuno limit. We will repeat this analysis starting with a more general transfer function in Section. 6.2.4.

5.3 Quantum network synthesis for n degrees of freedom

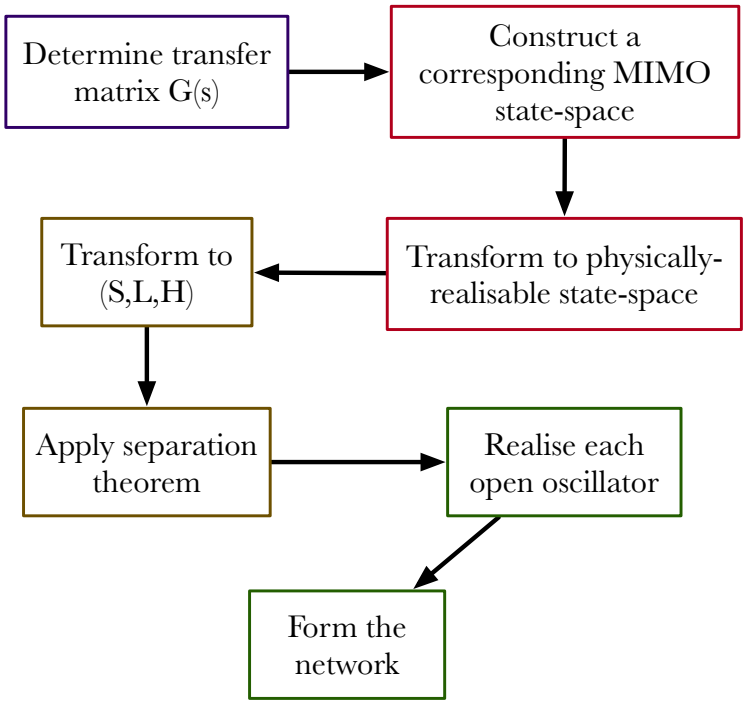

Figure 5.7 An overview of the steps for forming the physical realisation, i.e. the quantum network of generalised open oscillators, from a given transfer matrix.

In this section we will give a brief mostly-qualitative overview of the synthesis of quantum networks given a transfer-function or state-space representation of the dynamics of the system for systems with n internal degrees of freedom, summarising the methodology in [10] which we refer to for more specific quantitive details eschewed here. An overview of the steps for generally finding the physical realisation from the transfer matrix is shown in Figure. 5.7.

It is generally possible to find a physical realisation for a given transfer

matrix $\mathbf{G}(s)$ so long as it obeys Eq. (5.13), given some restrictions of the eigenvalues of the state-space matrices as discussed in [9]. Assuming the transfer matrix is in pole-zero form, the number of internal degrees of freedom of the system can be seen by the highest order in the Laplace frequency s in any of the elements $G_{ij}(s)$ of $\mathbf{G}(s)$, since this determines the number of states of the (not necessarily physically realisable) minimal state-space realisation. This order is unchanged by the similarity transformation mapping to the physically realisable state-space. Once this transformation is found a physically realisable state-space (A, B, C, D) can be deduced which can be used to determine the n degree-of-freedom generalised open oscillator $G = (S, \hat{L}, \hat{H})$ via Eq. (5.14). This open oscillator formalism is already quite a physically interesting representation of the system: it demonstrates all passive pre-processing of the input via the scattering matrix S, all the input-output coupling equations via $\hat{L}$, and the full internal dynamics of the system via $\hat{H}$.

When G represents a system with one degree-of-freedom we can already immediately write down the physical realisation as described above, however when it consists of n degrees of freedom it must first be separated into n individual one degree-of-freedom systems which are appropriately connected. For simplicity we consider the case where $S = I$ so there is no input scattering process which makes the following theorem significantly simpler. We also introduce a notation for the series product of two generalised open oscillators $G_1 = (I, K_1\mathbf{x}_1, \frac{1}{2}\mathbf{x}_1^\dagger R_1 \mathbf{x}_1)$ and $G_2 = (I, K_2\mathbf{x}_2, \frac{1}{2}\mathbf{x}_2^\dagger R_2 \mathbf{x}_2)$ (where we have let

$S_i = I$ for simplicity),

$$G_2 \triangleleft G_1 = \Big(I, K_2\mathbf{x}_2 + K_1\mathbf{x}_1, \frac{1}{2}\mathbf{x}_1^\dagger R_1 \mathbf{x}_1 + \frac{1}{2}\mathbf{x}_2^\dagger R_2 \mathbf{x}_2 + \frac{1}{2i}\mathbf{x}_2^\dagger (K_2^\dagger K_1 - K_2^T K_1^\#)\mathbf{x}_1 \Big), \tag{5.35}$$

which represents the feeding of the output of G_1 into the input of G_2. More generally we can have a "reducible network" of generalised open oscillators by also allowing direct interaction Hamiltonians between the open oscillators which is itself a generalised open oscillator, $\mathcal{N} = \{\{G_k\}_{k=1,\ldots,n}, \hat{H}^d, \mathcal{S}\}$ where $\hat{H}^d = \sum_j \sum_{k=j+1} \mathbf{x}_j^\dagger R_{jk} \mathbf{x}_k$ and $R_{jk} \in \mathbb{C}^{2\times 2}$ are the elements of the Hamiltonian matrix of each oscillator, and $\mathcal{S} = \{G_k \triangleleft G_j\}$ is a list of series products between each oscillator. We can now give a simplified version of Theorem 2 from [10].

Synthesis Theorem (simplified). *Let G be an n degree of freedom generalised open oscillator with Hamiltonian matrix $R \in \mathbb{C}^{2n\times 2n}$, coupling matrix $K \in \mathbb{C}^{m\times 2n}$, and identity scattering matrix $S = I_{m\times m}$. Then write R as 2×2 block matrices $R = [R_{jk}]_{j,k=1,\ldots,n}$ which are each Hermitian, and write K as a block matrix $K = [K_1 \; K_2 \; \ldots \; K_n]$ for each $j = 1, \ldots, n$ where $K_j \in \mathbb{C}^{m\times 2}$.*

Now, for each $j = 1, \ldots, n$ let $G_j = (I_{2\times 2}, K_j\mathbf{x}_j, \frac{1}{2}\mathbf{x}_j^\dagger R_{jj}\mathbf{x}_j)$ be independent one degree-of-freedom generalised open oscillators with ladder operators $\mathbf{x}_j = (\hat{a}_j, \hat{a}_j^\dagger)^T$, coupling operator K_j, and Hamiltonian matrix R_{jj}. Then define a direct interaction Hamiltonian,

$$\hat{H}^d = \sum_{j=1}^{n-1} \sum_{k=j+1}^{n} \mathbf{x}_k^\dagger \left(R_{jk}^\dagger - \frac{1}{2i}(K_k^\dagger K_j - K_k^T K_j^\#) \right) \mathbf{x}_j, \tag{5.36}$$

then the reducible network $\mathcal{N} = \{\{G_1, \ldots, G_n\}, \hat{H}^d, \{G_2 \triangleleft G_1, G_3 \triangleleft G_2, \ldots, G_n \triangleleft G_{n-1}\}\}$ is equivalent to G.

Once the system is separated, the individual systems can be realised as described in section. 5.1. The interaction Hamiltonian $\hat{H}^d$ can then be realised by overlapping the internal modes of each system through a beamsplitter and/or a non-linear crystal. For example, if we have a two degree-of-freedom system with main modes $\hat{a}$ and $\hat{b}$, then the interaction Hamiltonian $\hat{H}^d \propto \hat{a}\hat{b}^\dagger + \hat{a}^\dagger\hat{b}$ can be realised by overlapping both the cavity modes using a beamsplitter. This fuller formalism is used in Section. 6.1.1 and Chapter. 9.

Chapter Six

Optimal detector design

In Section. 5.1.3 we discussed how it would be possible to use the systematic realisation framework to design a detector that optimises the signal response. In general, there are two approaches to this: we can either start with an existing detector design and ask what kind of device can be inserted that improves the performance of the detector via coherent feedback, or take a bottom-up approach and design the entire detector using the framework.

In either case we are interested in optimising the signal-to-noise ratio (SNR), which is given by,

$$\mathcal{S} = \int_{f_1}^{f_2} \mathrm{d}f \, \frac{|h(f)|^2}{S_{hh}(f)}, \tag{6.1}$$

where $h(f)$ is the Fourier transform of the strain signal $h(t)$ and $S_{hh}(f)$ is the strain-referred noise spectral density.

6.1 Coherent feedback design

In this section I give an example of using the framework to design a coherent feedback filter, specifically a device to broaden the coupled cavity resonance.

6.1.1 Coupled cavity broadener

As discussed previously, current and future ground-based gravitational wave detectors are limited by quantum shot noise at high frequencies. Currently this prevents our measurement of the high frequency part of the binary neutron star inspiral waveform, knowledge of which would allow us to significantly constrain the neutron star equation of state. One way to improve the high-frequency sensitivity in a specific region is to use the coupled cavity resonance between the signal recycling cavity (SRC) and the arm cavities. This is a general feature of coupled harmonic oscillators with the same resonant frequency, where the single resonance at ω_0 is separated into two symmetric resonances at $\omega_0 \pm \omega_s$ due to the coupling between them [37]. When a gravitational wave passes it modulates the phase of the light in the arm cavities to induce sidebands in the differential laser mode at $\omega_0 \pm \omega$, with ω_0 being the input laser carrier frequency. Therefore the detector response to gravitational waves at frequency $\omega \approx \omega_s$ is increased. Since the coupled cavity resonances $\omega_0 \pm \omega_s$ are symmetric about ω_0 along with the induced sidebands $\omega_0 \pm \omega$ double the response can be achieved. The separation frequency is approximately given by $\omega_s \approx \sqrt{\gamma_{\rm arm}/\tau_{\rm SRC}}$ where $\gamma_{\rm arm}$ is the arm cavity bandwidth and $\tau_{\rm SRC} \equiv L_{\rm SRC}/c$ is the time delay across the SRC, with $L_{\rm SRC}$ being the length of the SRC and c being the speed of light.

Unfortunately, the width of the coupled cavity resonance is approximately given by the SRC bandwidth $\gamma_{\rm SRC}$, while its peak is proportional to $(\gamma_{\rm SRC})^{-1/2}$, and so there exist a tradeoff. In this chapter we will explore a new approach allowing us to broaden this coupled cavity resonance without sacrificing its peak.

Designing the transfer function

To analyse the system a single-sideband field approach was used. This is sufficient because we are predominantly interested in the behaviour of the shot noise which dominates at high frequencies, which is determined solely by the transfer function from the strain to the main interferometer readout. Note also that we are working in the rotating frame with respect to the laser carrier frequency ω_0 throughout this paper. To broaden the bandwidth a transfer function with a frequency-dependent phase $e^{i\phi(\Omega)}$ was placed into the SRC, and the system solved such as to give a control on the width of the coupled cavity peak while keeping its peak constant.

For ease of notation we define $\tau_1, \gamma_1 \equiv \tau_{\rm SRC}, \gamma_{\rm SRC}$, and $\tau_2, \gamma_2 \equiv \tau_{\rm arm}, \gamma_{\rm arm}$. We assume that both cavities are short and so we can expand the time delay across both cavities to first order, i.e. $\Omega\tau_1, \Omega\tau_2 \ll 1$. This is essential as otherwise the resulting transfer function will be infinite order. We also assume for simplicity that the cavity bandwidth's are small compared to the inverse round-trip travel time $\gamma_1\tau_1, \gamma_2\tau_2 \ll 1$, however this should be dropped for a more complete analysis. Finally we assume that the phase we introduce $\phi \ll 1$ to obtain a closed-form solution for ϕ. Altogether this leads to the

strain transfer function,

$$T_h(\Omega) \approx \frac{\alpha\gamma_1\tau_1\omega_s(i-\phi)}{\sqrt{\gamma_1\tau_2}\left(\gamma_1\tau_2\omega - i(\phi\omega + \tau_1(\omega^2-\omega_s^2))\right)}, \tag{6.2}$$

where α is the coupling strength of the signal. Note that our last approximation confines us to short-baseline facilities where the GW sideband frequency is much less than the free spectral range of the arm cavities.

By setting the phase $\phi = 0$ the transfer function for the coupled cavity is recovered,

$$T_h(\Omega) \approx \frac{\alpha\gamma_1\tau_1\omega_s i}{\sqrt{\gamma_1\tau_2}\left(\gamma_1\tau_2\Omega - i\tau_1(\Omega^2-\omega_s^2)\right)}. \tag{6.3}$$

This has a maximum at $\Omega = \omega_s$ called the "coupled cavity resonance", the width of which we wish to broaden by our choice of ϕ while keeping its peak constant.

To achieve this we set the denominator of eq. (6.2) to be equal to that of eq. (6.3) except with the former having a modified bandwidth γ_1' and a constant scaling factor β. The equation we solve is,

$$\gamma_1\tau_1\Omega - i\tau_1(\Omega^2-\omega_s^2) = \beta(\gamma_1'\tau_1\Omega - i(\phi\Omega + \tau_1(\Omega^2-\omega_s^2))). \tag{6.4}$$

The scaling factor β was then chosen to match the two transfer functions at $\Omega = \omega_s$, giving $\beta = \gamma_1/\gamma_1'$.

Solving eq. (6.4) for ϕ and then substituting for β we obtain a frequency-dependent phase of,

$$\phi = -\frac{\tau_1(\Omega^2-\omega_s^2)(\gamma_1-\gamma_1')}{\gamma_1\Omega}. \tag{6.5}$$

The transfer function we want to realise is given by $T(\Omega) = e^{i\phi}$, however this would be infinite order in the frequency Ω. To find a finite pole-zero

expansion we expand for $\phi \ll 1$, giving,

$$T(\omega) = \frac{2\gamma_1\Omega - i\tau_1(\Omega^2 - \omega_s^2)(\gamma_1 - \gamma_1')}{2\gamma_1\Omega + i\tau_1(\Omega^2 - \omega_s^2)(\gamma_1 - \gamma_1')}. \tag{6.6}$$

To find the controllable canonical form for the state-space, as in [100], we normalise the frequency variable by defining a normalised complex frequency $s = i\Omega/\omega_s$, giving,

$$T(s) = \frac{-s^2 + \frac{2\gamma_1}{\tau_1(\gamma_1 - \gamma_1')\omega_s}s - 1}{s^2 + \frac{2\gamma_1}{\tau_1(\gamma_1 - \gamma_1')\omega_s}s - 1}, \tag{6.7}$$

which gives the canonical state-space representation,

$$\begin{aligned}
\begin{bmatrix} \dot{\hat{a}} \\ \dot{\hat{a}}^\dagger \\ \dot{\hat{b}} \\ \dot{\hat{b}}^\dagger \end{bmatrix} &= \begin{bmatrix} 0 & 0 & 1 & 0 \\ 0 & 0 & 0 & 1 \\ -1 & 0 & \frac{2\gamma_1}{\tau_1\omega_s(\gamma_1' - \gamma_1)} & 0 \\ 0 & -1 & 0 & \frac{2\gamma_1}{\tau_1\omega_s(\gamma_1' - \gamma_1)} \end{bmatrix} \begin{bmatrix} \hat{a} \\ \hat{a}^\dagger \\ \hat{b} \\ \hat{b}^\dagger \end{bmatrix} \\
&\quad + \begin{bmatrix} 0 & 0 \\ 0 & 0 \\ 1 & 0 \\ 0 & 1 \end{bmatrix} \begin{bmatrix} \hat{a}_{\text{in}} \\ \hat{a}_{\text{in}}^\dagger \end{bmatrix},
\end{aligned} \tag{6.8}$$

$$\begin{bmatrix} \hat{a}_{\text{out}} \\ \hat{a}_{\text{out}}^\dagger \end{bmatrix} = \begin{bmatrix} 0 & 0 & \frac{4\gamma_1}{\tau_1\omega_s(\gamma_1' - \gamma_1)} & 0 \\ 0 & 0 & 0 & \frac{4\gamma_1}{\tau_1\omega_s(\gamma_1' - \gamma_1)} \end{bmatrix} \begin{bmatrix} \hat{a} \\ \hat{a}^\dagger \\ \hat{b} \\ \hat{b}^\dagger \end{bmatrix} - \begin{bmatrix} \hat{a}_{\text{in}} \\ \hat{a}_{\text{in}}^\dagger \end{bmatrix}. \tag{6.9}$$

In this case the system has two internal degrees of freedom $\hat{a}$ and $\hat{b}$, one input field $\hat{a}_{\text{in}}$, and one output field $\hat{a}_{\text{out}}$. The corresponding physically realisable

state-space is given by,

$$\begin{bmatrix} \dot{\hat{a}} \\ \dot{\hat{a}}^\dagger \\ \dot{\hat{b}} \\ \dot{\hat{b}}^\dagger \end{bmatrix} = \begin{bmatrix} 0 & 0 & 1 & 0 \\ 0 & 0 & 0 & 1 \\ -1 & 0 & \frac{2\gamma_1}{\tau_1\omega_s(\gamma_1'-\gamma_1)} & 0 \\ 0 & -1 & 0 & \frac{2\gamma_1}{\tau_1\omega_s(\gamma_1'-\gamma_1)} \end{bmatrix} \begin{bmatrix} \hat{a} \\ \hat{a}^\dagger \\ \hat{b} \\ \hat{b}^\dagger \end{bmatrix} + 2\sqrt{\frac{\gamma_1}{\tau_1\omega_s(\gamma_1'-\gamma_1)}} \begin{bmatrix} 0 & 0 \\ 0 & 0 \\ 0 & 1 \\ 1 & 0 \end{bmatrix} \begin{bmatrix} \hat{a}_{\text{in}} \\ \hat{a}_{\text{in}}^\dagger \end{bmatrix}, \tag{6.10}$$

$$\begin{bmatrix} \hat{a}_{\text{out}} \\ \hat{a}_{\text{out}}^\dagger \end{bmatrix} = 2\sqrt{\frac{\gamma_1}{\tau_1\omega_s(\gamma_1'-\gamma_1)}} \begin{bmatrix} 0 & 0 & 0 & 1 \\ 0 & 0 & 1 & 0 \end{bmatrix} \begin{bmatrix} \hat{a} \\ \hat{a}^\dagger \\ \hat{b} \\ \hat{b}^\dagger \end{bmatrix} - \begin{bmatrix} \hat{a}_{\text{in}} \\ \hat{a}_{\text{in}}^\dagger \end{bmatrix}. \tag{6.11}$$

A graphical representation of the above system was found using Simba and can be seen in Figure. 6.1 with an example optical layout given in Figure. 6.2, it too consisting of a coupled cavity, although coupled to the external continuum fields via a non-linear interaction. To match the desired transfer function, the separation frequency $\omega_s = \frac{c}{2}\sqrt{\frac{T}{LL_1}}$, where T is the power transmissivity of the mirror coupling the two cavities, and L, L_1 are the lengths of the two cavities, must match the separation frequency of the device we wish to broaden (in the case of broadening the coupled cavity resonance of an interferometer as discussed above we have $\omega_s = \sqrt{\gamma_{\text{arm}}/\tau_{\text{SRC}}}$).

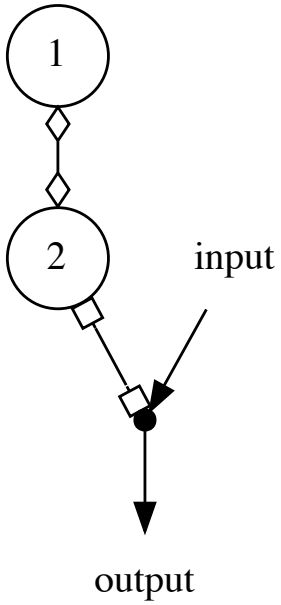

Figure 6.1 A schematic diagram of a physical realisation for the transfer function in Eq. (6.6). An optical layout is shown in Figure. 6.2. In this case we have two internal degrees of freedom labelled 1 and 2 which are coupled via a beamsplitter-like interaction, with mode 2 being coupled to the external continuum via an auxiliary mode, which it is coupled to via a non-linear crystal interaction. In the optical layout we label 1 as $\hat{a}_1$, 2 as $\hat{a}_2$. For general details of the graph representation see Section. 9.1.1.

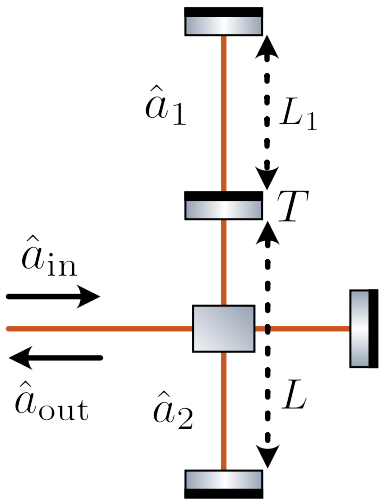

Figure 6.2 A schematic optical realisation of the coupled cavity broadener inferred from Figure. 6.1 after adiabatically eliminating the auxiliary mode. The device in the $\hat{a}_2$ cavity is the non-linear crystal.

6.2 Bottom-up approach

This section contains content from the third paper listed at the beginning of this thesis which is currently in preparation.

6.2.1 Introduction

The sensitivity of high-precision measurements is constrained by the quantum Cramer-Rao Bound (QCRB) which states that the variance of the measured signal due to noise is inversely proportional the variance σ_{NN} of the photon number of the probe degree of freedom coupled to the signal [94, 101, 95, 102, 99, 103]. This quantity is ultimately limited by the Heisenberg limit $\sigma_{NN} = N^2$, which states that the uncertainty scales with the number of resources available (in this case photons), although for most resonant detectors it is often constrained by the stronger shot noise limit $\sigma_{NN} = N$ [104]. This shot noise limit can be surpassed using techniques such as frequency-dependent squeezing [4] and bandwidth broadening via negative dispersion [30, 31, 5, 22], however the Heisenberg limit is not saturated in those cases. Previously the Heisenberg limit for phase measurement has been saturated in a non-resonant detector using a combination of entanglement, multiple sampling, and probabilistic adaptive measurements [105]. Theoretical examples of systems that saturate the limit have also been derived for exotic non-classical states [106, 107] and using quantum error correction [108]. Here we instead focus on linear optical phase measurement and an alternative approach to saturating the Heisenberg limit. In this section we introduce a general approach to realising

a Heisenberg limited detector directly from its input-output transfer matrix. We will use internal squeezing to directly increase the photon number fluctuation in the probe degree of freedom [109, 110] using the systematic realisation framework developed in [56]. We will consider both the most general first order detector and the most general second order detector.

The outline of this section is as follows. In Section. 6.2.2 we will show how quantum network synthesis can be used to find a physical realisation directly from the transfer matrix, and how the resulting detector's performance can be evaluated using the Quantum Cramér-Rao bound. In Section. 6.2.3 we will then discuss the various conditions on the transfer matrix arising from the physical realisability conditions, which greatly reduce the number of parameters needed to describe a physically realisable system. As an example of a system which saturates the Heisenberg limit via squeezing, in Section. 6.2.4 we consider a realisation of a system exhibiting input-output squeezing and show how the SNR diverges at the threshold.

6.2.2 Quantum Cramér-Rao Bound

For simplicity we consider only single-input single-output (SISO) quantum systems with the input and output fields each described by a pair of bosonic annihilation and creation operators. Specifically, we work in the quadrature formalism described by Caves and Schumaker [111, 112]. As discussed in [99], the Quantum Cramér-Rao Bound (QCRB) sets a fundamental lower limit on the variance of an unbiased estimator of a classical signal $x(t)$ coupled to a

detector linearly via $\hat{H}_{\rm int} = -\hat{F}x(t)$,

$$\sigma_{xx}^{\rm QCRB}(\Omega) = \frac{\hbar^2}{4S_{FF}(\Omega)}, \tag{6.12}$$

where $S_{FF}(\Omega)$ is the symmetrised power spectral density describing the quantum fluctuations of $\hat{F}$. Ignoring losses the spectral density of $\hat{F}$ is given by,

$$S_{FF}(\Omega) = S_{uu}(\Omega)|G_{uF}(\Omega)|^2 = |G_{uF}(\Omega)|^2, \tag{6.13}$$

where $G_{uF}(\Omega)$ is the open-loop transfer function from the input quadrature $\hat{u}$ to the internal degree-of-freedom $\hat{F}$. Further we have used that the measurement shot noise spectrum at the input has a white-noise spectrum $S_{uu}(\Omega) = 1$. Therefore by maximising the transfer function from the input to the probe degree of freedom we reduce the QCRB.

For simplicity we illustrate the general process with an optical GW interferometer where the probe fluctuation is related to the intracavity photon number fluctuation by,

$$S_{FF}(\Omega) = \frac{\hbar^2\omega_0^2}{2L_{\rm arm}^2}S_{NN}(\Omega), \tag{6.14}$$

where $S_{NN}(\Omega)$ is the power spectral density of the photon number fluctuations, ω_0 is the laser carrier frequency, and $L_{\rm arm}$ is the arm cavity length. In this case we measure the strain and therefore we should maximise the strain signal-to-noise ratio (SNR),

$$\mathcal{S} = \int_{-\infty}^{\infty} \frac{{\rm d}\Omega}{S_{hh}(\Omega)}, \tag{6.15}$$

where $S_{hh}(\Omega)$ is the strain signal spectral density and we have assumed that the frequency domain strain signal obeys $|h(\Omega)|^2 = 1$. This SNR is bound by

the QCRB,

$$\mathcal{S} \leq \int_{-\infty}^{\infty} \frac{\mathrm{d}\Omega}{S_{hh}^{\mathrm{QCRB}}(\Omega)} = \frac{\omega_0^2}{2}\sigma_{NN} \tag{6.16}$$

where $S_{hh}^{\mathrm{QCRB}}(\Omega) = \sigma_{xx}^{\mathrm{QCRB}}(\Omega)/L_{\mathrm{arm}}^2$, and σ_{NN} is total variance of the photon number of the probe degree of freedom. Therefore as shown in Eq. (6.13) maximising the transfer of the input field to $\hat{F}$ maximises the photon number variance which in turn minimises the QCRB and maximises the SNR. For passive resonant detectors the photon number fluctuation is limited by the aforementioned shot noise limit $\sigma_{NN} = N$ where N is the average photon number, giving $\mathcal{S} = \omega_0^2 N^2/2 = E^2/(2\hbar^2)$ where E is the average energy. This is known as the Mizuno limit [23]. The most important insight here is that the ultimate sensitivity limit of such detectors is limited purely by the detector's energy and is always independent of any other physical parameter such as the bandwidth or optical topology. As we shall see in Section. 7.1 the tuned cavity is Mizuno limited. In the following sections we will see that we can engineer an infinite photon number fluctuation $\sigma_{NN} \to \infty$ so that the Heisenberg limit $\sigma_{NN} \propto N^2$ is saturated.

As discussed in [56], we can synthesise any n degree-of-freedom system directly from its input-output transfer matrix, so long as it obeys certain conditions which we will discuss in Section. 6.2.3. Labelling each internal degree-of-freedom of the realisation as $\hat{F}_i,\ i = 1, \ldots, n$ we can then calculate the open-loop transfer functions from the input to those degrees of freedom, $G_{uF_i}(\Omega)$. We can then maximise the right-hand-side of Eq. (6.16) by maximising $G_{uF_i}(\Omega)$ for the optimal system parameters and also choosing the optimal internal degree-of-freedom $\hat{F}_i$ to couple the signal $x(t)$ to, giving us a sys-

tematic way of optimising the detector design given the input-output transfer matrix.

6.2.3 Constraints on input-output relations of linear detectors

In this section we will consider the constraints on the general input-output transfer matrix given by,

$$\begin{bmatrix} \hat{y}_1(\Omega) \\ \hat{y}_2(\Omega) \end{bmatrix} = \begin{bmatrix} G_{11}(\Omega) & 0 \\ 0 & G_{22}(\Omega) \end{bmatrix} \begin{bmatrix} \hat{u}_1(\Omega) \\ \hat{u}_2(\Omega) \end{bmatrix}, \tag{6.17}$$

where $\hat{y}$ and $\hat{u}$ are the output and input fields respectively in the two-photon quadrature formalism [111, 112]. We choose the off-diagonal rotation terms to be zero without loss of generality. One special case is where $|G_{11}(\Omega)|^2 = |G_{22}(\Omega)|^2 = 1$ in which case we have no squeezing as in Section. 7.1. To parameterise the transfer function we consider an n degree-of-freedom pole-zero form,

$$G_{11}(s) = \frac{\prod_{j=1}^{n}(s - z_j)}{\prod_{k=1}^{n}(s - p_k)}, \tag{6.18}$$

where $\{z_j \in \mathbb{C} \,|\, j = 1, \ldots, n\}$, $\{p_k \in \mathbb{C} \,|\, k = 1, \ldots, n\}$ are the zeroes and poles respectively, and n is equal to the number of internal modes of the quantum system. As shown in [9] the transfer matrix is physically realisable if,

$$\mathbf{G}_q^{\dagger}(s^*)\Theta\mathbf{G}_q(-s) = \Theta, \tag{6.19}$$

where $s = i\Omega$ and,

$$\Theta = \begin{bmatrix} 0 & i \\ -i & 0 \end{bmatrix}. \tag{6.20}$$

This condition restricts the conjugate transfer function to,

$$G_{22}(s) = \frac{\prod_{k=1}^{n}(-s - p_k^*)}{\prod_{j=1}^{n}(-s - z_j^*)}, \tag{6.21}$$

and so the poles/zeroes of G_{22} are the conjugates of the zeroes/poles of G_{11} respectively and the sign of the frequency is flipped. Since the real and imaginary parts of the poles and zeroes are independent we have in total $4n$ independent parameters specifying our system.

The possible poles and zeroes can be further reduced by noting that the quadrature operators are real and so the transfer matrix must obey $\mathbf{G}_q(-s) = \mathbf{G}_q^\dagger(s^*)$, which leads to the equation,

$$\prod_{j,k=1}^{n}(-s - p_k)(s - z_j^*) = \prod_{j,k=1}^{n}(s - p_k^*)(-s - z_j), \tag{6.22}$$

which can be expanded as,

$$\sum_{j=1}^{2n} a_j s^{j-1} = 0, \tag{6.23}$$

where a_j are algebraic combinations of the poles and zeroes. Therefore we have $a_j = 0,\ j = 1, \ldots, 2n$ and therefore the number of independent parameters is reduced to $2n$.

6.2.4 General first-order system

In this section we realise a general first-order input-output transfer matrix exhibiting squeezing, i.e. $|G(\Omega)| \neq 1$ for the sideband operators. Using internal squeezing to enhance the quantum-limited sensitivity was previously developed

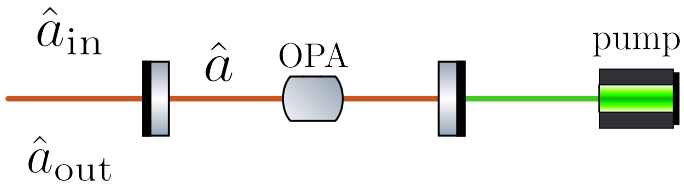

Figure 6.3 The setup for the squeezing of one quadrature via internal squeezing within the cavity, achieving an SNR that diverges at DC. The OPA (optical parametric amplifier) is pumped by the classical pump beam.

in [109, 110]. Specifically we consider the quadrature picture transfer matrix,

$$\mathbf{G}^q(i\Omega) = \begin{bmatrix} \frac{\alpha+i\Omega}{\beta-i\Omega} & 0 \\ 0 & \frac{\beta+i\Omega}{\alpha-i\Omega} \end{bmatrix}, \tag{6.24}$$

which obeys Eq. (6.19) and is the most general first order transfer matrix. Assuming that $\alpha > \beta$ so that the amplitude quadrature is amplified the physically realisable state-space is given by,

$$\begin{aligned} A &= \frac{1}{2}\begin{bmatrix} -\alpha-\beta & \alpha-\beta \\ \alpha-\beta & -\alpha-\beta \end{bmatrix}, \\ B &= \sqrt{\alpha+\beta}\; I_{2\times 2}, \\ C &= -\sqrt{\alpha+\beta}\; I_{2\times 2},\; D = I_{2\times 2}, \end{aligned} \tag{6.25}$$

where $I_{2\times 2}$ is the 2×2 identity matrix. The physical quantum system has one internal degree of freedom and its generalised open oscillator [10] is given by,

$$S = I_{2\times 2} \tag{6.26}$$

$$\hat{L} = \sqrt{2\alpha_+}\hat{a} \tag{6.27}$$

$$\hat{H} = -\frac{i}{2}\hbar\alpha_-(\hat{a}\hat{a} - \hat{a}^\dagger\hat{a}^\dagger), \tag{6.28}$$

where $\alpha_{\pm} \equiv (\alpha \pm \beta)/2$, and $\hat{a}$ is the annihilation operator of the cavity mode. Here S is the input-output direct scattering matrix, $\hat{L}$ is the coupling operator to the external continuum, and finally $\hat{H}$ is the system's internal Hamiltonian in the rotating frame at the laser carrier frequency. As shown in [56] this corresponds to a tuned cavity with coupling coefficient $\gamma \equiv \alpha_{+}$ and with a non-linear crystal with coupling frequency $\chi \equiv \alpha_{-}$, which is related to the single-pass squeezing factor by $r = 2\chi L/c$ where L is the cavity length. Inverting these relations gives $\alpha = \gamma + \chi$ and $\beta = \gamma - \chi$.

The quadrature picture transfer matrix from the inputs to the internal degree of freedom is given by,

$$\begin{bmatrix} \hat{a}^1 \\ \hat{a}^2 \end{bmatrix} = \begin{bmatrix} \frac{\sqrt{2\gamma}}{\gamma-\chi-i\Omega} & 0 \\ 0 & \frac{\sqrt{2\gamma}}{\gamma+\chi-i\Omega} \end{bmatrix} \begin{bmatrix} \hat{a}^1_{\text{in}} \\ \hat{a}^2_{\text{in}} \end{bmatrix}. \tag{6.29}$$

In this case the probe degree of freedom is $\hat{F} = \hat{a}^1$ and the input field is $\hat{u} \equiv \hat{a}^1_{\text{in}}$ giving the input-to-probe transfer function,

$$G_{uF}(\Omega) = \frac{\sqrt{2\gamma}}{\gamma - \chi - i\Omega}, \tag{6.30}$$

the magnitude of which (and thus the probe fluctuation S_{FF}) diverges when the cavity damping rate is equal to the non-linear crystal coupling frequency $\gamma = \chi$ which corresponds to the threshold case where the cavity acts as an optical parametric oscillator.

6.2.5 General second-order system

In this section we realise a general second-order input-output transfer matrix, showing that the optimal sensitivity is achieved when the parameters match

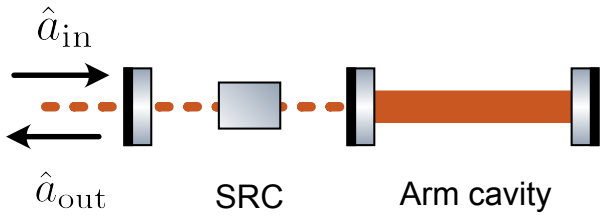

Figure 6.4 The setup analysed for the quantum expander as explored in [110], equivalent to a tuned Michelson interferometer except with squeezing (via a non-linear crystal) internally within the SRC (signal recycling cavity).

that of the so-called quantum expander first explored in [110], a setup which, similarly to the transmission-readout setup discussed in [22], can directly increase the detection bandwidth of a gravitational-wave interferometer. This setup, shown in Figure. 6.4, consists of a tuned, signal-recycled Michelson interferometer with internal squeezing in the signal recycling cavity. The signal-recycled Michelson can be mapped to an equivalent coupled-cavity [21]. We show that the quantum expander is the optimal detector for any second-order quadrature-picture transfer matrix obeying the above constraints.

We start with the most general second-order input-output transfer matrix,

$$\mathbf{G}^{q}(i\Omega) = \begin{bmatrix} \frac{(i\Omega-\alpha_1)(i\Omega-\beta_1)}{(i\Omega-\alpha_2)(i\Omega-\beta_2)} & 0 \\ 0 & \frac{(-i\Omega-\alpha_2)(-i\Omega-\beta_2)}{(-i\Omega-\alpha_1)(-i\Omega-\beta_1)} \end{bmatrix}, \tag{6.31}$$

where $\alpha_1, \alpha_2, \beta_1, \beta_2 \in \mathbb{R}$. Requiring that there is no gain at DC we also obtain the condition $\alpha_1\beta_1 = \alpha_2\beta_2$. We then follow the procedure given in [56] to find the physical realisation directly from this transfer matrix,

1. a minimal non-realisable canonical state-space is first found,

2. a transformation to the physically realisable state-space is then found,

3. the physical realisation corresponding to this state-space is found by calculating the two degree-of-freedom generalised open oscillator and separating into two one degree-of-freedom generalised open oscillators using the synthesis theorem in [10].

The corresponding physically realisable state-space is given by,

$$
\begin{aligned}
A &= \begin{bmatrix} 0 & 0 & -i\omega_s & 0 \\ 0 & 0 & 0 & i\omega_s \\ -i\omega_s & 0 & -\gamma & -\chi \\ 0 & i\omega_s & -\chi & -\gamma \end{bmatrix}, \\
B &= \begin{bmatrix} 0 & 0 \\ 0 & 0 \\ \sqrt{2}\sqrt{\gamma} & 0 \\ 0 & \sqrt{2}\sqrt{\gamma} \end{bmatrix}, \\
C &= \begin{bmatrix} 0 & 0 & -\sqrt{2}\sqrt{\gamma} & 0 \\ 0 & 0 & 0 & -\sqrt{2}\sqrt{\gamma} \end{bmatrix}, \; D = I_{2\times 2},
\end{aligned}
\tag{6.32}
$$

where $\gamma \equiv \frac{1}{2}(-\alpha_1 + \alpha_2 - \beta_1 + \beta_2)$, $\chi \equiv \frac{1}{2}(\alpha_1 + \alpha_2\beta_1 + \beta_2)$, and $\omega_s \equiv \sqrt{\alpha_1\beta_1}$. This corresponds to the dynamics derived from Hamiltonian for the quantum expander first described in [110]. The corresponding quantum network is given by $\mathcal{N} = \{\{G_1, G_2\}, \hat{H}^d, \mathcal{S}\}$ where $\mathcal{S} = G_2 \triangleleft G_1$ represents the series product [68], i.e. the output of G_1 is fed into G_2. The two generalised open oscillators are given by,

$$G_1 = (I_{2\times 2}, 0, 0)\,, \tag{6.33}$$

$$G_2 = \left(I_{2\times 2}, -\sqrt{2\gamma}\hat{a}_q, \tfrac{i}{2}\hbar\chi(\hat{a}_q\hat{a}_q + \hat{a}_q^\dagger\hat{a}_q^\dagger)\right), \tag{6.34}$$

where $I_{2\times2}$ is the 2×2 identity matrix, γ is the coupling frequency of the continuum to the cavity mode described by annihilation operator $\hat{a}_q$, and χ is the strength of the non-linear interaction. The Hamiltonian coupling the two cavities is given by $\hat{H}^d = \hbar\omega_s(\hat{a}_q\hat{a}^\dagger + \hat{a}_q^\dagger\hat{a})$ where $\hat{a}$ is the cavity mode of the second cavity, and is therefore a simple beamsplitter-like coupling between the two cavities. Note that G_1 is not coupled to the external continuum and therefore it is only coupled to G_2 via H^d. In total we have two tuned cavities coupled by a beamsplitter-like interaction, with the first cavity coupled to the external continuum and exhibiting internal squeezing, and have thus recovered the quantum expander realisation pictured in Fig. 6.4.

The quadrature transfer matrix from the input to the arm cavity mode $\hat{a}$ was found to be,

$$\begin{bmatrix} \hat{a}^1 \\ \\ \hat{a}^2 \end{bmatrix} = \begin{bmatrix} 0 & \frac{\sqrt{2\gamma}\omega_s}{i\omega(\chi-\gamma)+\omega_s^2-\omega^2} \\ -\frac{\sqrt{2\gamma}\omega_s}{-i\omega(\gamma+\chi)+\omega_s^2-\omega^2} & 0 \end{bmatrix} \begin{bmatrix} \hat{a}_{\rm in}^1 \\ \\ \hat{a}_{\rm in}^2 \end{bmatrix}. \tag{6.35}$$

Using Eq. (6.16) we see that the SNR for signal coupled to the amplitude quadrature is given by $2\pi\gamma/|\gamma - \chi|$, which diverges as $\chi \to \gamma$. At $\chi \gg \gamma$ the SNR approaches zero since the non-linear interaction totally depletes the amplitude quadrature fluctuations in the cavity. The SNR for the phase quadrature is given by $2\pi\gamma/(\gamma + \chi)$ which is maximal at $\chi = 0$ where it is equal to 2π and is thus constrained by the Mizuno limit.

For the signal recycling cavity mode $\hat{a}_q$, we also see the divergence at $\chi \to \gamma$, except that in this case the SNR for the phase quadrature diverges rather than

the amplitude quadrature,

$$\begin{bmatrix} \hat{a}_q^1 \\ \\ \hat{a}_q^2 \end{bmatrix} = \begin{bmatrix} -\frac{i\sqrt{2}\sqrt{\gamma}\omega}{-i\omega(\gamma+\chi)+\omega_s^2-\omega^2} & 0 \\ 0 & -\frac{i\sqrt{2}\sqrt{\gamma}\omega}{i\omega(\chi-\gamma)+\omega_s^2-\omega^2} \end{bmatrix} \begin{bmatrix} \hat{a}_{\text{in}}^1 \\ \\ \hat{a}_{\text{in}}^2 \end{bmatrix}. \tag{6.36}$$

In this case the SNR for the amplitude quadrature is given by $2\pi\gamma/(\gamma+\chi)$ and for the phase quadrature is given by $2\pi\gamma/|\gamma-\chi|$ i.e. the role of the amplitude and phase quadrature are swapped compared to the arm cavity mode.

Chapter Seven

Saturating the Heisenberg Limit via Hidden Modes

This chapter contains content from the third paper listed at the beginning of this thesis which is currently in preparation.

In this chapter we show how a tuned cavity can be augmented with auxiliary modes that do not affect the input-output dynamics, leading to infinite signal amplification and thus also saturating the Heisenberg limit [113]. In section. 7.2 we further show that an ideal QND (quantum non-demolition) measurement can be formed [42] by adding the auxiliary modes, and further that decoherence-free subspace [114, 115] is realised, allowing the auxiliary mode pair to be modified with arbitrary dynamics which are then realisable using the aforementioned framework. In section. 7.3 we also discuss the case where we begin with a two degree-of-freedom transfer function. Finally in section. 7.4 we discuss the general conditions for modifying a system's internal dynamics without affecting its input-output transfer matrix.

7.1 Signal Amplification via Hidden Modes

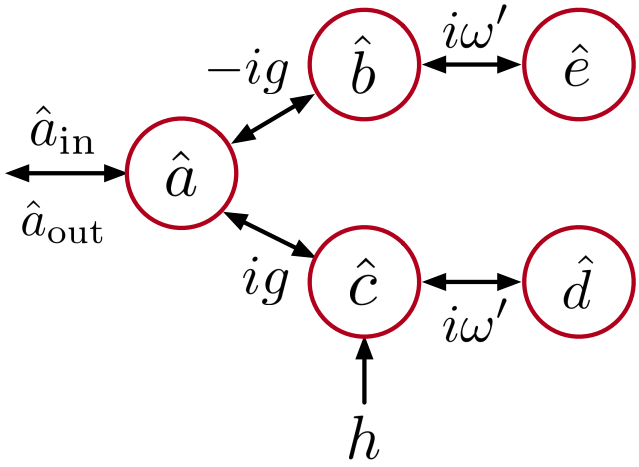

Figure 7.1 A schematic representation of the final input output relation developed in Section. 7.1. The modes $\hat{b}$ and $\hat{c}$ are coupled to the mode $\hat{a}$ via a squeezing-like interaction and beamsplitter-like interaction respectively with the same coupling frequency g, with the signal h being coupled to mode $\hat{c}$. In this setup the signal response diverges at DC. We then add two additional modes $\hat{d}$ and $\hat{e}$ coupled to the modes $\hat{b}$ and $\hat{c}$ respectively, both via beamsplitter-like couplings with coupling frequency ω' which shifts the signal response resonance to $\Omega = \omega'$.

In this section we show a tuned cavity can be augmented with a pair of unobservable "hidden" modes that act to amplify the signal and saturate the Heisenberg limit without modifying the input-output dynamics. We will first show that the minimal realization of a tuned cavity is constrained by the aforementioned Mizuno limit, however recently it has been shown that an infinite DC signal response can be achieved by adding a pair of modes that do not manifest in the input-output dynamics [113]. We will show how this is the simplest case of a general class of such non-minimal realisations, and that a degenerate free subspace is formed allowing for arbitrary modification of the

system dynamics.

First, the sideband-picture tuned cavity transfer matrix is given by,

$$\begin{bmatrix} \hat{a}_{\rm out}(\Omega) \\ \hat{a}^\dagger_{\rm out}(-\Omega) \end{bmatrix} = \begin{bmatrix} \frac{\Omega-i\gamma}{\Omega+i\gamma} & 0 \\ 0 & \frac{\Omega-i\gamma}{\Omega+i\gamma} \end{bmatrix} \begin{bmatrix} \hat{a}_{\rm in}(\Omega) \\ \hat{a}^\dagger_{\rm in}(-\Omega) \end{bmatrix}. \tag{7.1}$$

The physical realisation of this is a single mode coupled to the external continuum with dynamics determined by the Langevin equation and associated input-output relation, [19, 40, 17, 41]

$$\dot{\hat{a}} = -\gamma\hat{a} + \sqrt{2\gamma}\hat{a}_{\rm in} \tag{7.2}$$

$$\hat{a}_{\rm out} = \hat{a}_{\rm in} - \sqrt{2\gamma}\hat{a}, \tag{7.3}$$

where γ is the bandwidth of the cavity mode. The corresponding generalised open oscillator is given by,

$$S = I_{2\times 2},\ \hat{L} = -\sqrt{2\gamma}\hat{a},\ \hat{H} = 0. \tag{7.4}$$

If we choose to couple the signal to the $\hat{a}$ mode then the input-to-probe transfer function is given by,

$$G_{uF}(\Omega) = \frac{\sqrt{2\gamma}}{\gamma - i\Omega}. \tag{7.5}$$

Integrating this over all frequencies gives 2π and thus the total SNR will be bounded by a constant independent of the bandwidth, which is the aforementioned Mizuno limit.

We now consider adding two auxiliary modes $\hat{b}$ and $\hat{c}$ as shown in Fig. 7.1 and discussed in [113],

$$\hat{H}_0 = -\hbar g(\hat{a}\hat{c}^\dagger + \hat{a}^\dagger\hat{c}) - \hbar g(\hat{a}\hat{b} + \hat{a}^\dagger\hat{b}^\dagger). \tag{7.6}$$

We show in Appendix. 7.4 how this Hamiltonian can be inferred from a more general class of dynamics by requiring that the input-output relation remain unchanged by the auxiliary modes. Such a system is known as PT-symmetric (parity-time symmetric) as the Hamiltonian is left invariant under the parity operation (when the modes $\hat{c}$ and $\hat{b}$ are interchanged) and the time reversal operation ($\hat{c} \leftrightarrow \hat{c}^\dagger$, $\hat{b} \leftrightarrow \hat{b}^\dagger$) [116]. The equations of motion are given by,

$$\dot{\hat{a}} = -\gamma\hat{a} + ig\hat{c} + ig\hat{b}^\dagger + \sqrt{2\gamma}\hat{a}_{\text{in}}, \tag{7.7}$$

$$\dot{\hat{b}}^\dagger = -ig\hat{a}, \tag{7.8}$$

$$\dot{\hat{c}} = ig\hat{a}. \tag{7.9}$$

In this case we consider $\hat{c}$ to be the probe degree of freedom. Solving in the frequency domain we can find the input-to-probe transfer function,

$$G_{uF}(\Omega) = -\frac{g}{\Omega}\frac{\sqrt{2\gamma}}{\gamma - i\Omega}, \tag{7.10}$$

and therefore the probe fluctuation S_{FF} diverges at DC.

We can also explicitly introduce a classical signal $h(t)$ coupling to the amplitude quadrature of mode $\hat{c}$ (as for a cavity whose length is being modulated by a classical signal [17]) via,

$$\hat{H}_{\text{sig}} = -\hbar\alpha\hat{X}_c h(t), \tag{7.11}$$

where we have defined the amplitude quadrature as $\hat{X}_c = (\hat{c} + \hat{c}^\dagger)/\sqrt{2}$, and the dynamics for mode $\hat{c}$ are now given by,

$$\dot{\hat{c}} = ig\hat{a} + i\alpha h. \tag{7.12}$$

Solving for the readout mode $\hat{a}$ in terms of the signal leads to a divergent signal response at DC,

$$\hat{a}(\Omega) = \frac{g\alpha}{\Omega^2} h(\Omega) + \ldots, \tag{7.13}$$

and therefore the SNR $\mathcal{S}$ diverges.

7.2 Connection to QND measurement

It is interesting to consider why the signal response diverges at DC in this regime. We shall see here that it occurs due to this being an ideal QND (quantum non-demolition) measurement [42], in which case the probe degree of freedom has infinite fluctuation as it is conjugate to a conserved QND quantity. By re-writing Eq. (7.6) as,

$$\hat{H}_0 = -\hbar g[\hat{a}^\dagger(\hat{c} + \hat{b}^\dagger) + \hat{a}(\hat{c}^\dagger + \hat{b})], \tag{7.14}$$

we can see that the composite quantity $\hat{c}+\hat{b}^\dagger$ is conserved (since $[\hat{c}+\hat{b}^\dagger, \hat{c}^\dagger+\hat{b}] = 0$). This further implies two conserved quantities $\hat{X}_+ \equiv (\hat{X}_c + \hat{X}_b)/\sqrt{2}$, $\hat{Y}_- \equiv (\hat{Y}_c - \hat{Y}_b)/\sqrt{2}$ in terms of amplitude and phase quadratures $\hat{X}_c \equiv (\hat{c} + \hat{c}^\dagger)/\sqrt{2}$, $\hat{Y}_c \equiv (\hat{c} - \hat{c}^\dagger)/\sqrt{2}i$ (and similarly for $\hat{a}$ and $\hat{b}$). Rewriting the Hamiltonian in terms of these gives,

$$\hat{H}_0 = \hbar g(\hat{Y}_a\hat{X}_+ - \hat{X}_b\hat{Y}_-) - \hbar(\alpha/\sqrt{2})(\hat{X}_+ + \hat{X}_-)h, \tag{7.15}$$

where $\hat{X}_- \equiv (\hat{X}_c - \hat{X}_b)/\sqrt{2}$. The relevant residue part that can lead to detection of the signal h is given by,

$$\hat{H}_{\rm res} = -\hbar g\hat{X}_b\hat{Y}_- - \hbar(\alpha/\sqrt{2})\hat{X}_-h, \tag{7.16}$$

with $\hat{Y}_-$ being the conserved QND observable and $\hat{X}_-$ being the probe degree-of-freedom thus having infinite variance and therefore giving infinite signal response. In the frequency-domain $\hat{Y}_-$ exhibits the divergence at DC,

$$\hat{Y}_-(\Omega) = \frac{i\alpha}{\sqrt{2}\Omega} h(\Omega). \tag{7.17}$$

As discovered above, the operators $\hat{X}_+$ and $\hat{Y}_-$ are constants of motion and therefore act on a so-called decoherence-free subspace [114, 115], which is essentially decoupled from the external continuum. The dynamics can be arbitrarily modified while keeping this subspace decoherence-free so long as the simultaneous measurability condition is kept,

$$[\hat{X}_+(t), \hat{X}_+(t')] = [\hat{Y}_-(t), \hat{Y}_-(t')] = 0. \tag{7.18}$$

We can then use the realisation framework discussed above to realise modifications of the dynamics such that the Heisenberg limit is saturated over a range of frequencies. As an example we can shift the divergent response from DC to another frequency ω' by adding an extra pair of modes $\hat{d}$ and $\hat{e}$ which couple to $\hat{b}$ and $\hat{c}$ respectively, in which case the interaction Hamiltonian gains the following terms,

$$\begin{aligned} &-\hbar\omega'(\hat{b}\hat{d}^\dagger + \hat{b}^\dagger\hat{d} + \hat{c}^\dagger\hat{e} + \hat{c}\hat{e}^\dagger) \\ &= i\hbar\omega'(\hat{X}_+\hat{Q}_+ + \hat{Y}_+\hat{P}_+ - \hat{Y}_-\hat{P}_- + \hat{X}_-\hat{Q}_-), \end{aligned}$$

which satisfies Eq. (7.51) equal to zero and thus does not affect the input-output dynamics, and where we have defined,

$$\hat{Q}_\pm \equiv \frac{\hat{X}_d \pm \hat{X}_e}{\sqrt{2}}, \quad \hat{P}_\pm \equiv \frac{\hat{Y}_d \pm \hat{Y}_e}{\sqrt{2}}. \tag{7.19}$$

The residue part relevant to signal detection gains the term,

$$\hbar\omega'(\hat{X}_-\hat{Q}_- - \hat{Y}_-\hat{P}_-). \tag{7.20}$$

The latter term modifies the dynamics of $\hat{Y}_-$ to become,

$$\dot{\hat{Y}}_- = -\omega'\hat{Q}_- + \frac{\alpha}{\sqrt{2}}h, \tag{7.21}$$

$$\dot{\hat{Q}}_- = \omega'\hat{Y}_-, \tag{7.22}$$

and so eliminating $\hat{Q}_-$ in the frequency domain we obtain,

$$\hat{Y}_-(\Omega) = \frac{i\alpha\Omega}{\sqrt{2}(\Omega^2 - \omega'^2)}h(\Omega). \tag{7.23}$$

We see that the signal response now diverges at $\Omega = \omega'$ rather than at DC, and that the PT symmetric case shown in Eq. (7.17) is recovered for for $\omega' = 0$. The final phase quadrature input-output relation is given by,

$$\hat{Y}_{\text{out}}(\Omega) = -\frac{\Omega - i\gamma}{\Omega + i\gamma}\hat{Y}_{\text{in}}(\Omega) + \frac{\sqrt{\gamma}\alpha g\Omega h(\Omega)}{(\Omega^2 - \omega'^2)(\Omega + i\gamma)}. \tag{7.24}$$

So we have a system with no squeezing (in this case a first-order tuned cavity input output relation), while still saturating the Heisenberg limit by means of infinite signal amplification.

7.3 Signal amplification example: two degrees of freedom

Now we consider the transfer function for the transmission-readout setup first discussed in [22], which in the case where the damping rate of the mechanically

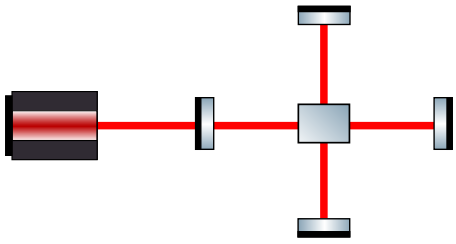

Figure 7.2 Realisation of an active coupled cavity, consisting of two cavity modes coupled by a non-linear crystal. A diagrammatic representation is shown in Figure. 9.1.

suspended oscillator γ_m is much less than any other frequency is given by,

$$\begin{bmatrix} \hat{a}_{\text{out}}(\Omega) \\ \hat{a}^{\dagger}_{\text{out}}(-\Omega) \end{bmatrix} = \frac{\Omega^2 - i\Omega\gamma_f + g^2 - \omega_s^2}{\Omega^2 + i\Omega\gamma_f + g^2 - \omega_s^2} \begin{bmatrix} \hat{a}_{\text{in}}(\Omega) \\ \hat{a}^{\dagger}_{\text{in}}(-\Omega) \end{bmatrix}, \tag{7.25}$$

where Ω is the GW (gravitational wave) sideband frequency relative to the laser carrier ω_0, γ_f is the damping rate of the SRC (signal recycling cavity), g is the coupling rate of the mechanically suspended oscillator in the SRC, and ω_s is the sloshing frequency between the SRC and the arm cavity. This system surpasses the Mizuno limit, i.e. $\mathcal{S} > \pi$, for $g > \omega_s$, and for $g = \omega_s$ has $\mathcal{S} = \infty$ since the signal response diverges at DC.

Note that the above transfer matrix is second order while the transmission-readout setup has three modes (the SRC mode $\hat{a}$, the arm cavity mode $\hat{A}$, and the mechanically suspended mirror mode $\hat{b}$), so one of those modes is now hidden. If we apply our framework to find the realisation of the above transfer function we get an active coupled cavity as shown diagrammatically in Figure. 7.2 which does not result in surpassing the Mizuno limit for either mode (i.e. $\mathcal{S} = \pi$). Therefore in this case the minimal realisation is not sufficient, and

we have to consider how a hidden mode can be added to regain the sensitivity improvement. One way to realise the system would be to consider the full 4×4 MIMO transfer matrix with a thermal heat bath $\hat{b}_{\rm th}$ coupled to the mechanically suspended mirror with $\gamma_m \neq 0$, however it is not easy to find the minimal state-space realisation in this case. To make progress we start with the interaction Hamiltonian for the transmission-readout setup,

$$\begin{aligned}\hat{H}_0 = &- \hbar\omega_s(\hat{a}\hat{A}^\dagger + \hat{a}^\dagger\hat{A}) - \hbar g(\hat{a}\hat{b} + \hat{a}^\dagger\hat{b}^\dagger) \\ &- \hbar\alpha(\hat{A} + \hat{A}^\dagger)h,\end{aligned} \tag{7.26}$$

where h is the classical signal. This leads to the equations of motion,

$$\dot{\hat{a}} + \gamma_f\hat{a} = ig\hat{b}^\dagger - i\omega_s\hat{A} + \sqrt{2\gamma_f}\hat{a}_{\rm in}, \tag{7.27}$$

$$\dot{\hat{b}}^\dagger = ig\hat{a}, \tag{7.28}$$

$$\dot{\hat{A}} = -i\omega_s\hat{a} + i\alpha h, \tag{7.29}$$

where $\hat{a}_{\rm in}$ is the input vacuum. Then by calculating the frequency domain equations and substituting into the equation for $\hat{a}$ the equation for the SRC mode is obtained,

$$(-i\Omega + \gamma_f)\hat{a} = \frac{ig^2}{\Omega}\hat{a} - \frac{i\omega_s^2}{\Omega}\hat{a} + \ldots, \tag{7.30}$$

where the term with g^2 arises from the $\hat{b}$ mode, and the term with ω_s^2 arises from the $\hat{A}$ mode and $\ldots$ contains the contribution from the input mode $\hat{a}_{\rm in}$ as well as the signal h which is not important here. Note that even though there are two modes they contribute the same frequency dependence to the system, and indeed we can add as many more modes as desired to the system

without increasing the order of the input-output transfer function. The reason for this is two-fold: first, both modes are degenerate (they both have zero eigenfrequency in our reference frame at the carrier frequency ω_0); second, they are not coupled to each other. The takeaway is that we can couple an arbitrary number of such modes to the system that are "hidden" from the input-output dynamics and that if the signal it coupled to one of these modes $\mathcal{S} > \pi$ can be achieved. If we add another mode coupled to $\hat{a}$ with the same eigenfrequency and coupling frequency then g_2 it can be easily shown that the strain transfer function and SNR $\mathcal{S}$ is unchanged if we make the replacement $g \to \sqrt{g^2 - g_2^2}$, therefore adding more modes does not add any further improvement and instead effectively shifts the coupling frequency of the mechanical resonator.

Now we consider the case where $g = \omega_s$ in which case Eq. (7.25) becomes a first-order tuned cavity. Clearly in this case it will not be possible to pass the Mizuno limit with the minimal realisation, however we know that the transmission-readout signal response diverges at DC for this parameter regime. Again looking at Eq. (7.30) we see that if g exactly equals ω_s then the contribution from the two modes cancels and the system becomes first-order. Therefore we can also add pairs of exactly cancelling modes without increasing the order of the input-output transfer function. Such modes cancel in the case where the coupling frequencies are equal, the modes' eigenfrequencies are equal (as in the above case), and one of the modes has a beamsplitter-like coupling to the mode $\hat{a}$ and the other has a non-linear crystal like coupling.

7.4 Auxiliary Mode Dynamics.

In this section we will discuss how the dynamics of added auxiliary modes, shown in Fig. 7.1, can be inferred by requiring that the frequency-domain input-output relation remain unchanged by the addition of them. Each auxiliary mode is coupled to a set of n_d internal modes $\hat{d}_j$ and n_e internal modes $\hat{e}_j$ adding the following terms to the Hamiltonian,

$$\begin{aligned}
\sum_j & -\hbar g_{d_j}(\hat{b}\hat{d}_j^\dagger + \hat{b}^\dagger \hat{d}_j) - \hbar g_{d_j^\dagger}(\hat{b}\hat{d}_j + \hat{b}^\dagger \hat{d}_j^\dagger) \\
& - \hbar g_{e_j}(\hat{c}\hat{e}_j^\dagger + \hat{c}^\dagger \hat{e}_j) - \hbar g_{e_j^\dagger}(\hat{c}\hat{e}_j + \hat{c}^\dagger \hat{e}_j^\dagger) \\
& + \sum_{i\neq j} \hbar g_{d_i d_j^\dagger}(\hat{d}_i \hat{d}_j^\dagger + \hat{d}_i^\dagger \hat{d}_j) + \hbar g_{d_i d_j}(\hat{d}_i \hat{d}_j + \hat{d}_i^\dagger \hat{d}_j^\dagger) \\
& + \sum_{i\neq j} \hbar g_{e_i e_j^\dagger}(\hat{e}_i \hat{e}_j^\dagger + \hat{e}_i^\dagger \hat{e}_j) + \hbar g_{e_i e_j}(\hat{e}_i \hat{e}_j + \hat{e}_i^\dagger \hat{e}_j^\dagger),
\end{aligned}$$

where $g_{d_i d_j^\dagger}$ and $g_{d_i d_j}$ respectively quantify the beamsplitter-like and non-linear coupling between modes $\hat{d}_i$ and $\hat{d}_j$, and similarly for the $\hat{e}$ modes. Note that there is no direct coupling between the $\hat{d}$ and $\hat{e}$ modes.

The full set of equations of motion are,

$$\begin{aligned}\dot{\hat{a}} =& -\gamma\hat{a} + \sqrt{2\gamma}\hat{a}_{\text{in}} \\ & - ig_b\hat{b} + ig_{b^\dagger}\hat{b}^\dagger - ig_c\hat{c} + ig_{c^\dagger}\hat{c}^\dagger, \end{aligned} \tag{7.31}$$

$$\dot{\hat{b}} = ig_b\hat{a} - ig_{b^\dagger}\hat{a}^\dagger + i\sum_j g_{d_j}\hat{d}_j - i\sum_j g_{d_j^\dagger}\hat{d}_j^\dagger, \tag{7.32}$$

$$\dot{\hat{d}}_j = ig_{d_j}\hat{b} + ig_{d_j^\dagger}\hat{b}^\dagger - i\sum_{i\neq j} g_{d_i d_j^\dagger}\hat{d}_i - i\sum_{i\neq j} g_{d_i d_j}\hat{d}_i^\dagger, \tag{7.33}$$

$$\dot{\hat{c}} = ig_c\hat{a} - ig_{c^\dagger}\hat{a}^\dagger + i\sum_j g_{e_j}\hat{e}_j - i\sum_j g_{e_j^\dagger}\hat{e}_j^\dagger, \tag{7.34}$$

$$\dot{\hat{e}}_j = ig_{e_j}\hat{c} + ig_{e_j^\dagger}\hat{c}^\dagger - i\sum_{i\neq j} g_{e_i e_j^\dagger}\hat{e}_i - i\sum_{i\neq j} g_{e_i e_j}\hat{e}_i^\dagger. \tag{7.35}$$

Focussing on $\hat{d}_j$, the frequency-domain expression is given by,

$$-i\Omega\vec{d}(\Omega) = \vec{g}_d\hat{b}(\Omega) + \vec{g}_{d^\dagger}\hat{b}^\dagger(-\Omega) - iG^{(d)}\vec{d}(\Omega), \tag{7.36}$$

where,

$$\vec{g}_d = (ig_{d_1}, -ig^*_{d_1^\dagger}, \ldots, ig_{d_{n_d}}, -ig^*_{d_{n_d}^\dagger})^T, \tag{7.37}$$

$$\vec{g}_{d^\dagger} = (ig_{d_j^\dagger}, -ig^*_{d_j}, \ldots, ig_{d_{n_d}^\dagger}, -ig^*_{d_{n_d}})^T, \tag{7.38}$$

and where,

$$\vec{d}(\Omega) = (\hat{d}_1(\Omega), \ldots, \hat{d}_{n_d}(\Omega); \hat{d}_1^\dagger(-\Omega), \ldots, \hat{d}_{n_d}^\dagger(-\Omega))^T. \tag{7.39}$$

and where in block form,

$$G^{(d)} = \begin{bmatrix} G_1^{(d)} \\ \vdots \\ G_{n_d}^{(d)} \end{bmatrix} \in \mathbb{C}^{2n_d\times 2n_d}, \tag{7.40}$$

where,

$$G_j^{(d)} = \begin{bmatrix} g_{d_1 d_j^\dagger} & \cdots & g_{d_{n_d} d_j^\dagger}; & g_{d_1 d_j} & \cdots & g_{d_{n_d} d_j} \\ g^*_{d_1 d_j^\dagger} & \cdots & g^*_{d_{n_d} d_j^\dagger}; & g^*_{d_1 d_j} & \cdots & g^*_{d_{n_d} d_j} \end{bmatrix}, \tag{7.41}$$

with $g_{d_j d_j} = g_{d_j d_j^\dagger} = 0$. Solving for $\vec{d}(\Omega)$ gives,

$$\begin{aligned} \vec{d}(\Omega) &= (-i\Omega I_{2n_d \times 2n_d} + iG^{(d)})^{-1} \begin{bmatrix} \vec{g}_d & \vec{g}_{d^\dagger} \end{bmatrix} \begin{bmatrix} \hat{b}(\Omega) \\ \hat{b}^\dagger(-\Omega) \end{bmatrix} \\ &\equiv M^{(d)} \begin{bmatrix} \hat{b}(\Omega) \\ \hat{b}^\dagger(-\Omega) \end{bmatrix}, \end{aligned}$$

where $I_{2n_d \times 2n_d}$ is the $2n_d \times 2n_d$ identity matrix, and $M^{(d)} \in \mathbb{C}^{2n_d \times 2}$.

The frequency domain expression for $\hat{b}$ is given by,

$$-i\Omega \begin{bmatrix} \hat{b}(\Omega) \\ \hat{b}^\dagger(-\Omega) \end{bmatrix} = \begin{bmatrix} ig_b & -ig_{b^\dagger} \\ ig^*_{b^\dagger} & -ig^*_b \end{bmatrix} \begin{bmatrix} \hat{a}(\Omega) \\ \hat{a}^\dagger(-\Omega) \end{bmatrix} + iD^{(d)}\vec{d}(\Omega), \tag{7.42}$$

where,

$$D^{(d)} = \begin{bmatrix} g_{d_1}, & \ldots, & g_{d_{n_d}}; & -g_{d_1^\dagger}, & \ldots, & -g_{d_{n_d}^\dagger} \\ g^*_{d_1^\dagger}, & \ldots, & g^*_{d_{n_d}^\dagger}; & -g^*_{d_1}, & \ldots, & -g^*_{d_{n_d}} \end{bmatrix}. \tag{7.43}$$

Solving for the $\hat{b}$ mode we get,

$$\begin{bmatrix} \hat{b}(\Omega) \\ \hat{b}^\dagger(-\Omega) \end{bmatrix} = T^{(b)}(\Omega) \begin{bmatrix} \hat{a}(\Omega) \\ \hat{a}^\dagger(-\Omega) \end{bmatrix}, \tag{7.44}$$

where,

$$T^{(b)}(\Omega) \equiv (-i\Omega I_{2\times 2} - iD^{(d)}M^{(d)})^{-1} \begin{bmatrix} ig_b & -ig_{b^\dagger} \\ ig^*_{b^\dagger} & -ig^*_b \end{bmatrix}, \tag{7.45}$$

and where $I_{2\times 2}$ is the 2×2 identity matrix.

Similarly we have,

$$\begin{bmatrix} \hat{c}(\Omega) \\ \hat{c}^\dagger(-\Omega) \end{bmatrix} = T^{(c)}(\Omega) \begin{bmatrix} \hat{a}(\Omega) \\ \hat{a}^\dagger(-\Omega) \end{bmatrix},$$

where,

$$T^{(c)}(\Omega) \equiv (-i\Omega I_{2\times 2} - iD^{(e)}M^{(e)})^{-1} \begin{bmatrix} ig_c & -ig_{c^\dagger} \\ ig^*_{c^\dagger} & -ig^*_c \end{bmatrix} \tag{7.46}$$

where,

$$D^{(e)} = \begin{bmatrix} g_{e_1}, & \ldots, & g_{e_{n_e}}; & -g_{e_1^\dagger}, & \ldots, & -g_{e_{n_e}^\dagger} \\ g^*_{e_1^\dagger}, & \ldots, & g^*_{e_{n_e}^\dagger}; & -g^*_{e_1}, & \ldots, & -g^*_{e_{n_e}} \end{bmatrix}, \tag{7.47}$$

and where,

$$M^{(e)} = (-i\Omega I_{2n_e\times 2n_e} + iG^{(e)})^{-1}, \tag{7.48}$$

where in block form,

$$G^{(e)} = \begin{bmatrix} G_1^{(e)} \\ \vdots \\ G_{n_e}^{(e)} \end{bmatrix} \in \mathbb{C}^{2n_e\times 2n_e}, \tag{7.49}$$

where,

$$G_j^{(e)} = \begin{bmatrix} g_{e_1e_j^\dagger} & \cdots & g_{e_{n_e}e_j^\dagger}; & g_{e_1e_j} & \cdots & g_{e_{n_e}e_j} \\ g^*_{e_1e_j^\dagger} & \cdots & g^*_{e_{n_e}e_j^\dagger}; & g^*_{e_1e_j} & \cdots & g^*_{e_{n_e}e_j} \end{bmatrix}. \tag{7.50}$$

The frequency domain expression for $\hat{a}$ is given by,

$$\begin{aligned}
-i\Omega \begin{bmatrix} \hat{a}(\Omega) \\ \hat{a}^\dagger(-\Omega) \end{bmatrix} &= \begin{bmatrix} ig_b & -ig_{b^\dagger} \\ ig_{b^\dagger}^* & -ig_b^* \end{bmatrix} \begin{bmatrix} \hat{b}(\Omega) \\ \hat{b}^\dagger(-\Omega) \end{bmatrix} \\
&\quad + \begin{bmatrix} ig_c & -ig_{c^\dagger} \\ ig_{c^\dagger}^* & -ig_c^* \end{bmatrix} \begin{bmatrix} \hat{c}(\Omega) \\ \hat{c}^\dagger(-\Omega) \end{bmatrix} + \ldots, \\
&= T^{(a)}(\Omega) \begin{bmatrix} \hat{a}(\Omega) \\ \hat{a}^\dagger(-\Omega) \end{bmatrix} + \ldots
\end{aligned}$$

where $\ldots$ are the damping and input vacuum terms from Eq. (7.2) and where,

$$\begin{aligned}
T^{(a)}(\Omega) \equiv &\begin{bmatrix} ig_b & -ig_{b^\dagger} \\ ig_{b^\dagger}^* & -ig_b^* \end{bmatrix} T^{(b)}(\Omega) \\
&+ \begin{bmatrix} ig_c & -ig_{c^\dagger} \\ ig_{c^\dagger}^* & -ig_c^* \end{bmatrix} T^{(c)}(\Omega) = 0.
\end{aligned} \tag{7.51}$$

Therefore to keep the input-output dynamics invariant, all elements of this matrix must be zero.

We can now use the above to recover the Hamiltonian with two auxiliary degrees of freedom given in Eq. (7.6), starting with the general linear Hamiltonian,

$$\begin{aligned}
&- \hbar g_b(\hat{a}\hat{b}^\dagger + \hat{a}^\dagger\hat{b}) - \hbar g_{b^\dagger}(\hat{a}\hat{b} + \hat{a}^\dagger\hat{b}^\dagger) \\
&- \hbar g_c(\hat{a}\hat{c}^\dagger + \hat{a}^\dagger\hat{c}) - \hbar g_{c^\dagger}(\hat{a}\hat{c} + \hat{a}^\dagger\hat{c}^\dagger).
\end{aligned}$$

The terms with coupling rates g_b and g_c are coupled to $\hat{a}$ via a beamsplitter, and the terms with coupling rates $g_{b^\dagger}$ and $g_{c^\dagger}$ via a non-linear crystal (or

equivalently an optomechanical interaction with optomechanical coupling frequency g, as discussed in [22, 113]). Each auxiliary mode has just one degree of freedom, and so we have $n_d = n_e = 0$, and thus,

$$T^{(b)} = \frac{1}{-i\Omega}\begin{bmatrix} ig_b & -ig_{b^\dagger} \\ ig^*_{b^\dagger} & -ig^*_b \end{bmatrix}, \tag{7.52}$$

$$T^{(c)} = \frac{1}{-i\Omega}\begin{bmatrix} ig_c & -ig_{c^\dagger} \\ ig^*_{c^\dagger} & -ig^*_c \end{bmatrix}. \tag{7.53}$$

This gives,

$$T^{(a)}(\Omega) \equiv \frac{1}{-i\Omega}(-g_b^2 + g_{b^\dagger}^2 - g_c^2 + g_{c^\dagger}^2)I_{2\times 2}. \tag{7.54}$$

If we now choose cavity mode $\hat{c}$ to be coupled to mode $\hat{a}$ purely by a beamsplitter-like interaction, as for the arm cavity of an interferometer, then we have $g_c = \omega_s$ with ω_s being the sloshing frequency between the mode $\hat{c}$ and mode $\hat{a}$ and no non-linear coupling: $g_{c^\dagger} = 0$. Therefore the input-output dynamics are left invariant if $g_b = 0$ and $g_{b^\dagger} = \omega_s$, and so mode $\hat{b}$ should be coupled to mode $\hat{a}$ via a non-linear interaction (e.g. a non-linear crystal if $\hat{b}$ is an optical mode) with the same coupling constant as the $\hat{c}$ mode: $g \equiv g_{b^\dagger} = \omega_s$. Therefore we have recovered the expected Hamiltonian.

Chapter Eight

All-optical PT Symmetric Amplifier

This section contains content from the fourth paper listed at the beginning of this thesis which is currently in preparation. Here I present the PT-symmetric quantum amplifier, a stable configuration which exhibits infinite signal response at DC. I infer an all-optical realisation of the previous optomechanical design and propose a preliminary implementation example in a LIGO-like detector as well as a tabletop experiment design.

8.1 Introduction

Recently the breakthrough theoretical discovery was made that a PT (parity-time) symmetric system can lead to an infinite signal response at DC and thus a diverging quantum-limited sensitivity while remaining marginally stable [113]. Such a setup consists of a readout mode, coupled to an arm cavity probe field via a beamsplitter, and coupled to a mechanically suspended mirror via

radiation pressure with a pump beam. As we will see this is identical to the non-symmetric setup first discussed in [22] except with the two coupling rates exactly equal. However, due to the optomechanical nature of the setup it is very susceptible to thermal noise, and in those works extreme parameters were chosen for the mechanically suspended mirror to minimise the effect. For this setup the additional noise power spectral density added by the mechanical oscillator is given by,

$$S_{\hat{n}\hat{n}}(\Omega) = \frac{T_{\text{env}}}{Q_m} \frac{4k_B c T_a}{\hbar L_a T_b \Omega^2}, \tag{8.1}$$

where Q_m is the quality factor of the mechanical oscillator, T_a is the transmissivity of the input mirror to the signal cavity, T_b is the transmissivity of the readout port mirror, and L_a is the length of the signal cavity. We use the parameters given for the LIGO implementation in Table. 8.1, and examine the higher frequencies of interest around $\Omega = 2\pi \times 1\,\text{kHz}$. For the thermal noise contribution to be less than the shot noise contribution we then require,

$$\frac{T_{\text{env}}}{Q_m} \lesssim 2 \times 10^{-9}\,\text{K}, \tag{8.2}$$

which gets even stricter as the frequency of interest decreases.

This strict requirement has lead to significant research and development efforts, such as ultra-high Q mechanical resonators [51] and also using an optical spring to dampen the thermal noise [43, 60]. Motivated by a previous all-optical realisation of an unstable filter [56], in this paper we demonstrate how a non-linear crystal can be used to implement the same interaction as present in the optomechanical setup, resulting in a realisation which does not suffer from intense degradation due to thermal noise.

In [117] it was shown that in the simplest case an infinite DC signal response can be realised without affecting the input-output dynamics of the system given that two modes are coupled to the readout mode with equal coupling constants, with one of the modes (e.g. the arm cavity mode) being coupled via a beamsplitter-like interaction, and the other mode being coupled by a non-linear interaction. In the optomechanical case explored in [22, 113] it was shown that given the rotating wave approximation, the radiation pressure interaction between the readout mode $\hat{b}$ and the idler mode $\hat{c}$ (in this case a mechanically suspended mirror), as well as the coupling between the readout and the probe mode $\hat{a}$ which the signal is coupled to, is described by the following interaction Hamiltonian:

$$\hat{H}_{\text{int}} = -\hbar G(\hat{c}\hat{b} + \hat{c}^{\dagger}\hat{b}^{\dagger}) - \hbar g(\hat{a}^{\dagger}\hat{b} + \hat{a}\hat{b}^{\dagger}), \tag{8.3}$$

where G is the optomechanical coupling rate and g is the sloshing rate between the arm cavity and readout mode. The PT symmetric condition is given by $G = g$ where the system becomes symmetric under parity transformation $\hat{a} \leftrightarrow \hat{c}$ and time reversal $\hat{a} \leftrightarrow \hat{a}^{\dagger}, \hat{c} \leftrightarrow \hat{c}^{\dagger}$ [116]. Effectively the loss and gain processes are perfectly matched. A schematic of the general system is shown in Fig. 8.1. As shown in [56] this same interaction can be realised using a non-linear crystal. This immediately points us to an all-optical realisation of the PT-symmetric amplifier, which as discussed above does not suffer from the issue of thermal noise. Instead we will see that the main difficulty becomes the optical loss requirement in the idler mode.

In this paper we will discuss two designs. First in Section. 8.2 we will give the theoretical background of the setup. Then in Section. 8.3 we will

discuss a possible implementation into a LIGO-like interferometer. Finally in Section. 8.4 we will propose a table-top experiment demonstrating this effect. In both cases we use the frequency regime inspired by [118] of quantum up-conversion of the 810 nm idler field to the 1550 nm probe field via a 532 nm pump field.

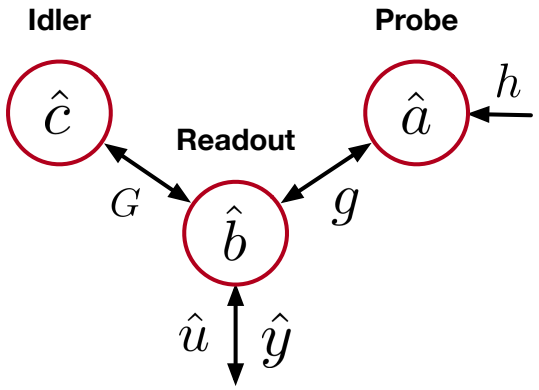

Figure 8.1 Schematic of a general PT-symmetric amplifier, consisting of three modes: an idler, readout, and probe, with a signal h coupled to the probe mode. The idler and readout are coupled via a non-linear interaction with coupling strength G, while the probe and readout are coupled via a beamsplitter-like interaction with coupling strength g. The system is PT-symmetric when $G = g$. The readout mode is coupled to the external input and output continuum fields $\hat{u}$ and $\hat{y}$.

8.2 Theoretical overview

As discussed above, the form of the interaction in Eq. (8.3) is identical between the optomechanical case and the all-optical realisation. Therefore we can use the same formalism as discussed in previous optomechanical realisations [22, 113], which we will briefly outline here. Specifically, we work in the single-mode approximation $\Omega \ll \mathrm{FSR}_{\mathrm{arm}}$ where Ω is the sideband frequency relative

to the laser carrier ω_0 and $\mathrm{FSR}_{\mathrm{arm}}$ is the free spectral range of the arm cavity, allowing us to represent each cavity by a single annihilation operator. Overall we have three modes describing our setup, the arm cavity mode $\hat{a}$, the signal recycling cavity (SRC) readout mode $\hat{b}$, and the mechanically suspended mirror mode $\hat{c}$. As shown in [56] the two-mode squeezing Hamiltonian in Eq. (8.3) can be realised with a non-linear crystal by replacing the mechanically suspended mirror mode $\hat{c}$ with an optical idler mode, and that this is identical to the two-mode squeezing interaction with a non-linear crystal with,

$$G = rc/(2L_b), \tag{8.4}$$

where L_b is the length of the signal recycling cavity and r is the single-pass squeezing factor [56]. The sloshing frequency between the arm cavity and readout mode is given by $g \approx \sqrt{c\gamma_a/L_b}$ where c is the speed of light, γ_a is the half-bandwidth of the $\hat{a}$ mode, and L_b is the length of the readout mode cavity [37, 38]. The readout mode $\hat{b}$ is coupled to the continuous input $\hat{u}$ and output $\hat{y}$ modes via the Langevin equation with damping rate $\gamma_b = T_b c/(4L_b)$ where T_b is the transmissivity of the mirror coupling to the external continuum [18, 17]. In the absence of radiation-pressure and losses, and letting the real signal $h(t)$ be coupled to the phase of mode $\hat{a}$, the full equations of motion are given by,

$$\hat{y} = \hat{u} - \sqrt{2\gamma_b}\hat{b}, \tag{8.5}$$

$$\dot{\hat{b}} + \gamma_b\hat{b} = iG\hat{c}^\dagger + ig\hat{a} + \sqrt{2\gamma_b}\hat{u}, \tag{8.6}$$

$$\dot{\hat{c}} = iG\hat{b}^\dagger, \tag{8.7}$$

$$\dot{\hat{a}} = ig\hat{b} + i\omega_0\bar{a}h, \tag{8.8}$$

where $\bar{a} \equiv [2P_a L_a/(\hbar\omega_0 c)]^{1/2}$ is the mean photon number in the $\hat{a}$ mode, and where P_a is the circulating power in the $\hat{a}$ mode, L_a is the length of the cavity, and ω_0 is the main laser carrier frequency. The dynamical matrix, using state vector $\vec{x} = (\hat{a}, \hat{b}, \hat{c}^\dagger)^T$, can be written as,

$$A = \begin{bmatrix} 0 & ig & 0 \\ ig & -\gamma_b & iG \\ 0 & -iG & 0 \end{bmatrix}, \tag{8.9}$$

with the following eigenvalues,

$$\lambda = 0,\ \frac{1}{2}\left(-\gamma_b \pm \sqrt{4(G^2 - g^2) + \gamma_b^2}\right). \tag{8.10}$$

For $G > g$ as used in [22] we thus have one positive real eigenvalue and thus the system is unstable, however in the PT symmetric regime $G = g$ the system is marginally stable [53, 113]. This simple stability analysis in the single-mode approximation regime will be extended to higher frequencies in future work.

The frequency-domain input-output relation is given by,

$$\begin{aligned} \hat{y} = &\frac{g^2 - G^2 + i\gamma_b\Omega - \Omega^2}{g^2 - G^2 - i\gamma_b\Omega - \Omega^2}\hat{u} \\ &+ \frac{\sqrt{2\gamma_b}g\omega_0\bar{a}}{g^2 - G^2 - \Omega(\Omega + i\gamma_b)}h. \end{aligned} \tag{8.11}$$

We can see that the input-output transfer function has unity gain as expected, and the strain transfer function diverges at DC in the PT symmetric regime $G = g$. In this regime the system exhibits an exceptional point where the total SNR scales with time faster than the relative measurement error, and thus an infinite SNR can be achieved [119].

The optical loss terms can be easily added by adding the following terms to the equations of motions for the cavity modes,

$$\dot{\hat{a}} = -\gamma_a^\epsilon \hat{a} + \sqrt{2\gamma_a^\epsilon} + \ldots, \tag{8.12}$$

$$\dot{\hat{b}} = -\gamma_b^\epsilon \hat{b} + \sqrt{2\gamma_b^\epsilon} + \ldots, \tag{8.13}$$

$$\dot{\hat{c}} = -\gamma_c^\epsilon \hat{c} + \sqrt{2\gamma_c^\epsilon} + \ldots, \tag{8.14}$$

where $\gamma_a = \epsilon_a c/(4L_a)$ where ϵ_a is the total loss in the $\hat{a}$ mode cavity and similarly for $\hat{b}$ and $\hat{c}$.

8.3 LIGO implementation

In this section we will consider the LIGO implementation of such an all-optical PT symmetric amplifier as shown in Fig. 8.2, with the sensitivity improvement over the standard tuned case shown in Fig. 8.3. The parameters used are shown in Table. 8.1. In this case the modes $\hat{a}, \hat{b}, \hat{c}$ are the arm cavity, signal recycling cavity, and idler mode respectively. A set of different mirror dichroic and trichroic coatings are used. The steering mirrors for the pump beam are fully reflective for the 532 nm pump, while fully transparent for the 810 nm idler and 1550 nm probe beams. The SRM (signal-recycling mirror) is partially reflective for the probe while fully reflective for the idler. Finally the ITM (input test mass) is partially reflective for the probe while being fully transmissive for the idler, so as to increase the effective length of the idler mode cavity and thus dilute its optical loss.

Losses in the signal recycling cavity do not break the PT symmetry and therefore do not greatly affect the sensitivity improvement. This is shown in

Fig. 8.4: even at losses as high as 5000 ppm there is little degradation of the effect. The arm cavity and idler cavity losses do break the PT symmetry, as they introduce loss into each mode which is not perfectly matched by gain in the other mode, and therefore as seen in Fig. 8.3 the low-frequency sensitivity boost is greatly impacted by the idler and arm losses.

Parameter		Value
Arm length	L_a	4 km
SRC length	L_b	56 m
Test mass	M	40 kg
ITM trans.	T_a	0.02
SRM trans.	T_b	0.01
Arm power	P_a	270 kW
Sloshing freq.	$g/(2\pi)$	7.129 kHz

Table 8.1 Parameters used in the LIGO implementation.

8.4 Experimental design

In this section we will propose a tabletop experimental design, shown in Fig. 8.5, demonstrating improved signal response via PT symmetry. In this case, the mirror labelled IM is partially transmissive to the probe, fully transmissive to the pump, and fully reflective to the idler. The mirror opposite that to the left is fully transmissive to the pump and fully reflective to the pump and probe. The mirror CM is partially reflective to the probe while being fully

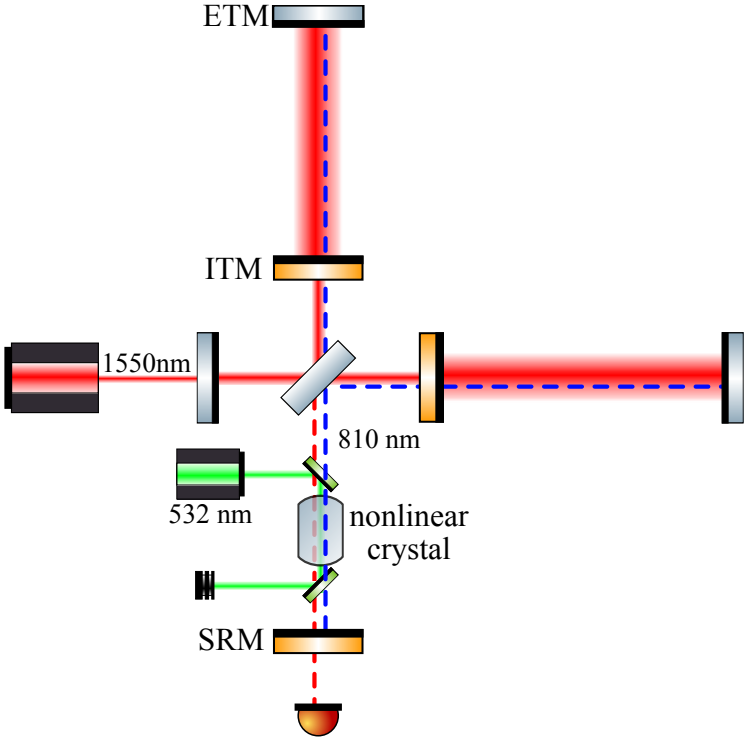

Figure 8.2 The all-optical PT-symmetric amplifier implementation in a LIGO-like interferometer

transmissive to the idler (again to dilute the effect of the idler loss).

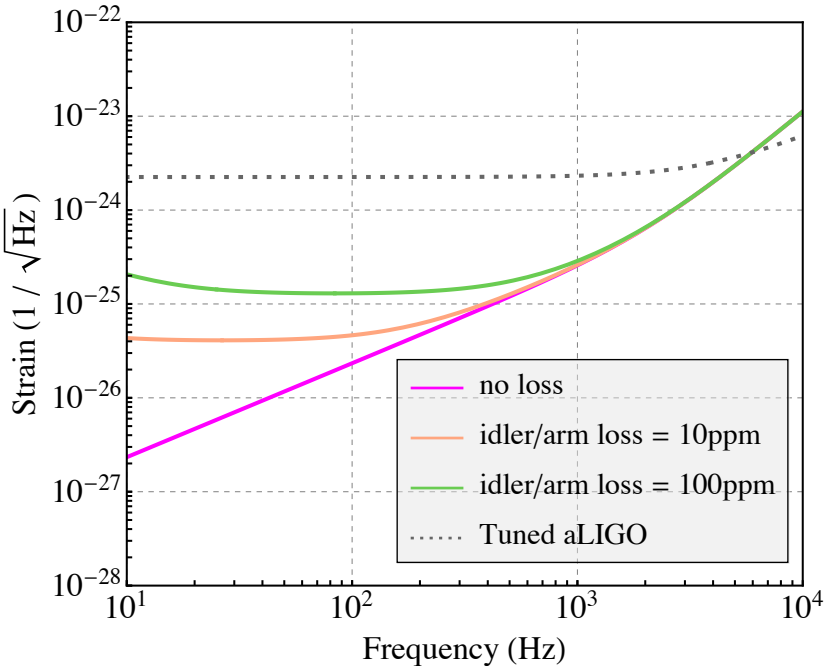

Figure 8.3 Comparison between the sensitivity between the PT symmetric amplifier and tuned case, as well as the impact of loss in the idler and arm cavity fields. The introduction of loss to these modes breaks the PT symmetry, reducing the low-frequency sensitivity boost. Note that the impact of the idler and arm cavity losses are equivalent.

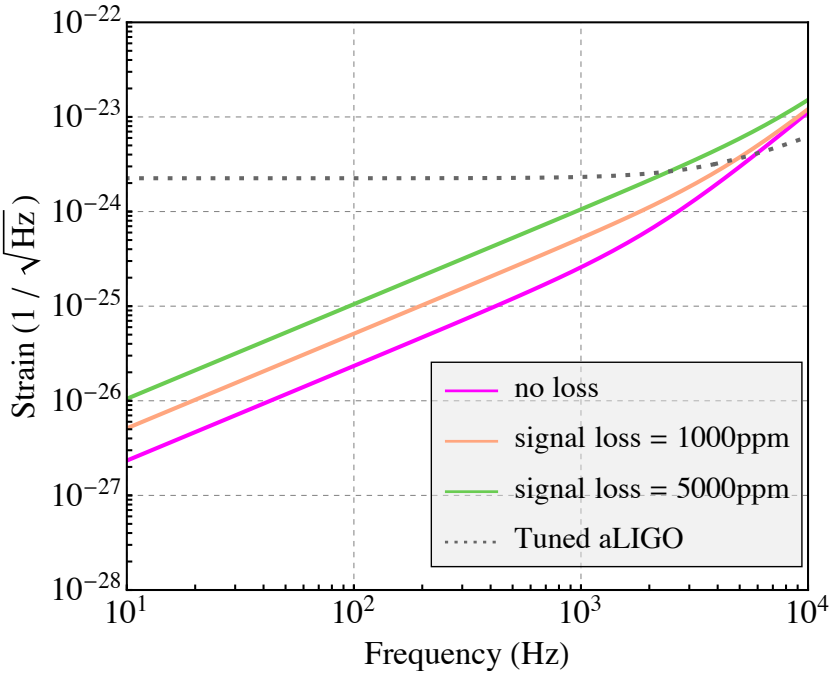

Figure 8.4 Impact of optical loss in the signal recycling mode on the sensitivity. In this case the PT symmetry is not broken and thus the low-frequency sensitivity boost is not greatly impacted, even up to losses of 5000 ppm.

Parameter		Value
Top cavity length	L	50 cm
Bottom cavity length	L_f	10 cm
IM trans.	T_{IM}	0.01
CM trans.	T_{CM}	100 ppm
Sloshing freq.	$g/(2\pi)$	1.067 MHz
Crystal pump power	P_c	3 W
Crystal parameters...		...

Table 8.2 Parameters used in the tabletop experimental implementation.

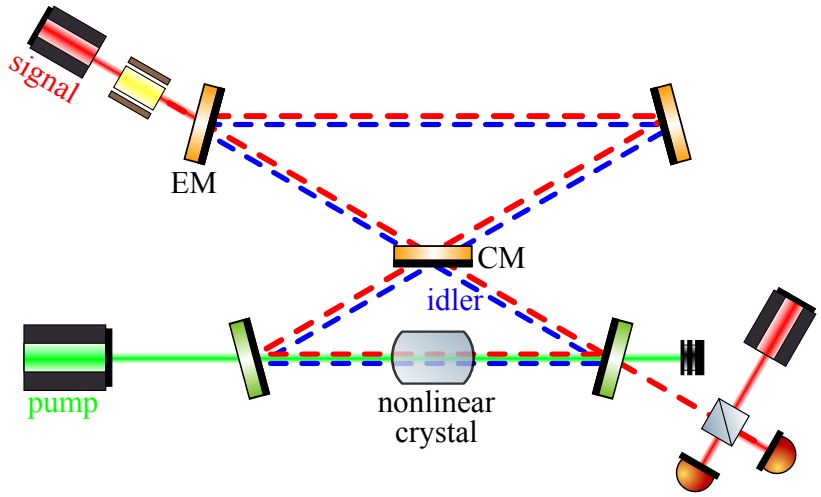

Figure 8.5 Experimental design for an all-optical PT-symmetric amplifier.

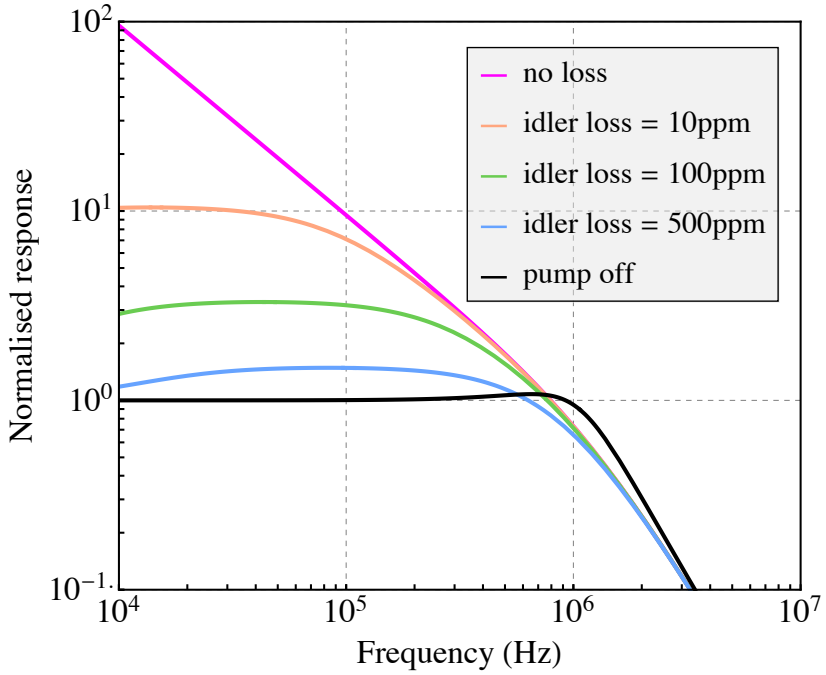

Figure 8.6 Impact of idler loss on the probe response.

Chapter Nine

SImBA

In this section we will discuss a set of Python and Mathematica scripts that automate the discovery of a physical realisation directly from a given set of transfer functions. The scripts are posted publicly on Github (https://github.com/joebentley/simba) and in-depth documentation of all features is hosted on Read the Docs (https://simbapy.readthedocs.io/en/latest/).

9.1 Capabilities and core functions

Here we will discuss the core functionality of the software. Some parts are only available in the Mathematica package, while most parts are entirely in Python using the Sympy symbolic manipulation package. Mathematica was used mainly for convenience as a lot of functions such as finding the minimal realisation of MIMO state spaces for given transfer matrices are built-in. The following is a list of core capabilities with M meaning only in Mathematica, P meaning only in Python, and MP meaning available in both,

- The conversion of SISO transfer function to a state-space representation

(MP)

- The conversion of MIMO transfer matrices to a state-space representation (M—built-in to Mathematica)
- Checking whether a MIMO transfer matrix obeys the symplectic condition given in Eq. (5.13) and is thus physically realisable (MP)
- Finding the physically realisable state-space from a given state-space (MP)
- Checking whether a state-space is physically realisable (MP)
- Converting a state-space to the generalised open oscillator formalism as in Eq. (5.14) (P)
- Separating the n degree-of-freedom generalised open oscillator into n 1 degree-of-freedom generalised open oscillators as discussed in section. 5.3 (P)
- Calculating all open-loop and closed-loop transfer functions between degrees of freedoms of the system (P)
- Generating a graph layout representing the different couplings between modes of the system as discussed in section. 9.1.1 (P)

Some features that are not yet implemented that should be in the future are,

- Non-identity direct-feed matrices $D \neq I$
- Graphical representation for MIMO systems

9.1.1 Graph representation and legend

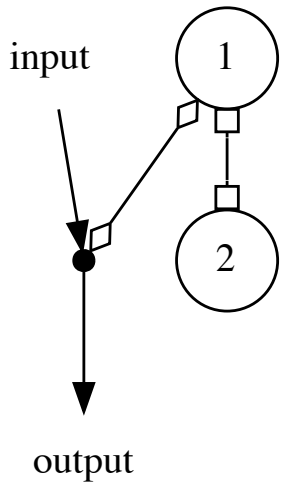

Figure 9.1 The generated graph for an active coupled cavity transfer function. It simply consists of two cavity modes that are coupled via a non-linear interaction, with an auxiliary mode coupling to one of the cavity modes via a beamsplitter interaction.

It is possible to generate a graph representation for any physically realisable SISO system, an example of which are shown in Figs. 9.3 and 9.1. In fact the function `transfer_function_to_graph` can be used to generate the graph directly from the transfer function. The graph representation is a useful way to visualise the physical connections in the system and what kind of interactions these consist of. It gives a physical intuition for what kind of configuration of quantum elements will be needed to realise any given system, especially in cases where the resulting system might be particularly complicated. Note

however that it gives no information on any of the coefficients of terms of the system (apart from whether or not they are non-zero).

Each internal mode is numbered as n, while auxiliary modes associated with each internal mode are drawn as filled dots. The shape of the main mode is determined by the R matrix for that degree of freedom as given by Eq. (5.31) which we repeat here for reference,

$$R = \frac{1}{2}\begin{bmatrix} \Delta & i\epsilon \\ -i\epsilon^* & \Delta \end{bmatrix}, \tag{9.1}$$

where Δ is the detuning and ϵ is the effective non-linear crystal pump intensity, which determine the shape of each mode as shown in Figure. 9.2.

The filled black arrows each represent a series connection ($G_i \triangleleft G_j$) from open oscillator j to i as described in Section. 5.3. Each auxiliary mode is connected in series in this way. Auxiliary modes that are not coupled to their corresponding main modes (i.e. the coupling matrix $K = 0$) are adiabatically eliminated and so we do not draw them. For example, in Fig. 9.3 the associated auxiliary mode is not coupled to 2, and so we do not draw it, as it does not affect the dynamics of the system. The couplings between two different modes, for example $\hat{a}$ and $\hat{b}$ are represented by unfilled double-ended arrows. Beamsplitter-like interactions with interaction Hamiltonians of the form $\hat{H} = \hat{a}\hat{b}^\dagger + \hat{a}^\dagger\hat{b}$ are displayed as diamonds; non-linear/squeezing-like interactions of the form $\hat{H} = \hat{a}\hat{b} + \hat{a}^\dagger\hat{b}^\dagger$ are represented by boxes as shown in Fig. 9.1; interactions which have a mixture of both are marked using a box on one side of the arrow, and a diamond on the other side.

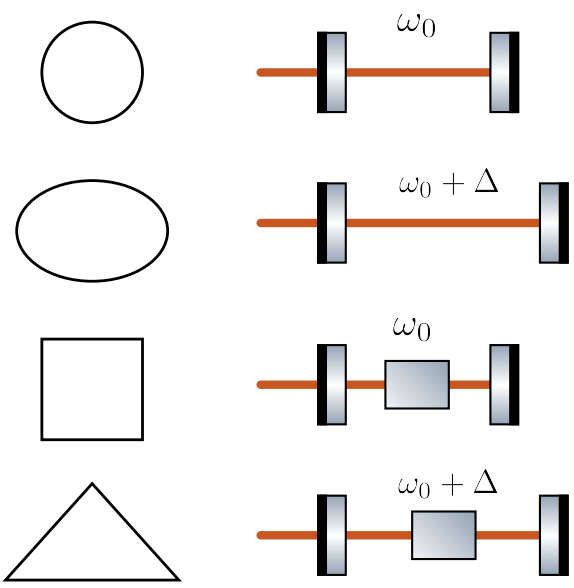

Figure 9.2 The correspondence between different shapes of the internal mode and the type of cavity mode as determined by the internal Hamiltonian show in Eq. (9.1). The laser carrier frequency is ω_0. From top-to-bottom, a circle represents a tuned cavity ($\Delta = 0, \epsilon = 0$), an ellipse represents a detuned cavity ($\Delta \neq 0, \epsilon = 0$), a square represents a degenerate parametric amplifier ($\Delta = 0, \epsilon \neq 0$), and a triangle represents a detuned degenerate parametric amplifier ($\Delta \neq 0, \epsilon \neq 0$).

9.2 In-depth overview

We will now summarise the most important functions and classes that comprise the software.

9.2.1 Mathematica

The Mathematica package is located in the Github repository at `notebooks/Simba.wl` and comprises of four main functions,

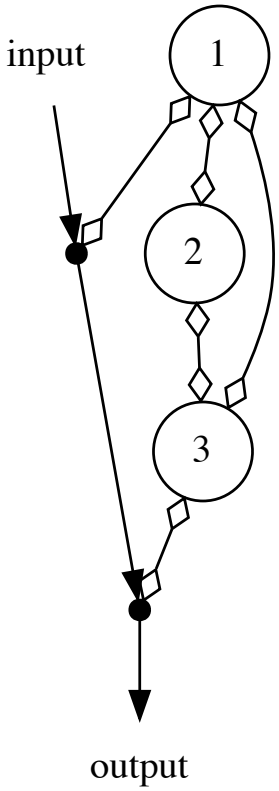

Figure 9.3 The generated graph for the third-order transfer function $\frac{s^3+s^2+s-1}{-s^3+s^2-s-1}$. In this case all of the interactions are beamsplitter-like. The auxiliary mode for mode 2 is not coupled to mode 2 and so is not drawn as it is adiabatically eliminated.

- `JMatrix` takes a positive integer n and returns the $2n \times 2n$ J-matrix as in Eq. (5.13),
- `SymplecticJ` computes the left-hand side of Eq. (5.13),
- `FindXMatrix` finds the matrix X that solves the physical realisability

conditions in Eqs. (5.8) and (5.9),

- `FindTMatrix` finds the matrix T given X such that $X = TJT^\dagger$.

The benefit of using Mathematica is that it already includes a rich set of built-in functionality around the symbolic manipulation of state spaces which is not available in Python. For example given a transfer matrix $\mathbf{G}(s)$ in Mathematica bound to a variable `tfmatrix`, a minimal MIMO state-space realisation can be found simply via `MinimalStateSpaceModel[StateSpaceModel[ TransferFunctionModel[tfmatrix,s]]]`. Similarly `ObservableModelQ` and `ControllableModelQ` can be used to determine if the system is observable and controllable respectively. It also includes functionality for designing stabilising control systems via pole placement and other methods. However, since it is not open-source software and is quite expensive for non-academic users, a majority of the functionality was written in Python so as to be accessible to a wider audience.

9.2.2 Python

As mentioned above, as much of the software as possible was written using Python using only open-source packages to be more accessible. In this section we will summarise the main classes and methods of the software. The software comprises of two main modules: `simba.core` contains classes and functions associated with computing state-spaces, separating generalised open oscillators, and calculating transfer functions, while `simba.graph` generates graphical representations of quantum networks.

Most systems will start as an instance of `simba.core.StateSpace`. Either the (A, B, C, D) matrices can be passed to the constructor after being calculated in Mathematica, or if the transfer matrix is SISO the `classmethod`s can be used to construct an instance directly. If a SISO transfer matrix is used, the system can be extended to quantum afterwards by using the `extended_to_quantum` method, which simply takes the Hermitian conjugate of the matrices and stacks them up in doubled-up notation [66]. The method `reorder_to_paired_form` reorders the state, input, and output vectors from the doubled-up ordering $(\hat{a}_1, \ldots, \hat{a}_n; \hat{a}_1^\dagger, \ldots, \hat{a}_n^\dagger)^T$ to the paired ladder-operator ordering $(\hat{a}_1, \hat{a}_1^\dagger; \ldots; \hat{a}_n, \hat{a}_n^\dagger)^T$. The method `to_physically_realisable` is used to transform to a physically realisable state-space. The property `is_physically_realisable` is used to check whether or not the state-space is currently physically realisable. Finally, the method `to_slh` returns an instance of `simba.core.SLH` which represents the system as a generalised open oscillator as given in Eqs. (5.14) and described in detail in Section. 5.3.

The `SLH` class has one important method `split` which separates the n degree-of-freedom generalised open oscillator into n one degree-of-freedom generalised open oscillators and a direct interaction Hamiltonian as described in Section. 5.3. The split network is represented by an instance of `simba.core.SplitNetwork`.

The `simba.core.SplitNetwork` class has a number of useful methods for calculating the dynamics of the system. First the method `interaction_hamiltonian` calculates the interaction Hamiltonian between all the internal modes $\hat{a}_i$ of the system, including the auxiliary modes $\hat{a}_i'$ introduced to alter

the coupling to the external continuum modes as described previously, but not including the Hamiltonian for coupling to the external continuum itself[1]. The method `dynamical_matrix` computes the full frequency-domain dynamical matrix (`SplitNetwork.DynamicalMatrix`) for the system including the Langevin and input-output terms. The transfer matrix can then be calculated and used to calculate all the open and closed loop transfer functions between the internal modes and input and output modes of the system.

The main class for handling graph-based representations of quantum networks is `simba.graph.Nodes`, which can be generated from a `SplitNetwork` instance using the `simba.graph.nodes_from_network` function. The graph can be converted to an instance of `pygraphviz.AGraph` from the `pygraphviz` module which can then be rendered and saved.

9.3 Next steps

SImBA is a novel and useful piece of software in itself, however some difficulties in the development have showed that an alternative approach could be taken. I decided at an early point that it would be better to work in a fully symbolic way, since this is often more useful for theoreticians designing new detectors and quantum noise reduction approaches. However, this makes the calculation much more complicated in general, especially given the difficulties of letting Sympy know whether given combinations of parameters are positive or negative, and generally long computation times. The next step in the

[1]That is, we do not compute the Hamiltonian shown in Eq. (5.24), but instead just compute the Langevin equations directly for each external continuum field.

development for SImBA will then be facilitating a fully numerical approach, which is potentially more useful for experimentalists who already have given numerical parameters in mind.

Chapter Ten

Conclusion

In this thesis I have presented a set of new techniques for the design of optimal detectors for high-precision measurements. Starting with an exploration of the quantum noise that currently limits precise linear measurements, and how the Mizuno limit sets a limit on the sensitivity-bandwidth product of all passive resonant detectors, I then proposed a new optical layout known as the transmission-readout setup which incorporates a non-linear interaction to broaden the bandwidth of the detector without sacrificing the peak sensitivity. Since devices that incorporate negative dispersion such as the unstable filter and transmission-readout setup are unstable in their bandwidth broadening regimes I then briefly discussed how local control can be applied to stabilise the system without sacrificing sensitivity.

Using a mathematical formalism developed by the quantum control community, I then applied quantum network synthesis to find an all-optical realisation of the unstable filter as opposed to the optomechanical design originally proposed, as well as recovering the internal squeezing setup. This inspired the most important discovery of the thesis: the use of quantum network synthe-

sis to design optimal detectors by maximising the signal-to-noise ratio (SNR). Two approaches were considered, the design of coherent feedback devices for already existing detectors, of which a device which broadens the bandwidth of a coupled-cavity resonance without sacrificing the peak sensitivity is deduced, and a "bottom-up" approach of designing the entire detector using the framework. In the latter approach I considered three systems in increasing complexity. First I revisited the one degree-of-freedom system with internal squeezing, showing that the maximal SNR can be recovered at the threshold $s_0 = \gamma$ from a general transfer function. Then, I looked at a general second-order transfer matrix and recovered a system known as the quantum expander, recovering the results discussed in [110]. Finally, I considered how the entire transmission-readout setup could be inferred from the full transfer-matrix.

Given recent developments by the group in Caltech and using the above all-optical realisation of an optomechanical interaction, I also proposed an all-optical realisation of the PT-symmetric quantum amplifier, both in a LIGO implementation and as a table-top experimental proposal.

Finally I presented my software Simba which allows the user to automate the process of finding the realisation from the transfer matrix. I invented a new graphical format for representing the types of interactions between complex quantum systems which is generic to different realisation methods (optical, atomic, optomechanical, etc. . .).

There are some interesting future avenues that need to be explored. For example, the application of local sensing to cancelling the thermal noise and its integration in future designs, and the application of the new techniques

outlined to producing detectors for new physics such as axion detection and quantum gravity experiments, as well as general high-precision measurements. Finally we can consider extending our single mode approach to multi mode detectors which use their resonance across multiple FSRs, leading to the possibility of detecting very broadband signals.

APPENDICES

Appendix A

Transforming Between Sideband and Quadrature pictures

In this section we will derive the transformation between the single-photon sideband operators and the two-photon quadratures. In the sideband picture the general input-output relation can be written in the form,

$$\hat{b}(\Omega) = T_+(\Omega)\hat{a}(\Omega) + T_-(\Omega)\hat{a}^\dagger(-\Omega) + G(\Omega)h(\Omega), \tag{A.1}$$

where Ω is the sideband frequency relative to some reference frequency ω_0.

The definition of the amplitude and phase quadratures for the input and output fields about ω_0 are given by,

$$\hat{b}_1(\Omega) = \frac{\hat{b}(\Omega) + \hat{b}^\dagger(-\Omega)}{\sqrt{2}}, \qquad \hat{b}_2(\Omega) = \frac{\hat{b}(\Omega) - \hat{b}^\dagger(-\Omega)}{i\sqrt{2}},$$
$$a_1(\Omega) = \frac{a(\Omega) + a^\dagger(-\Omega)}{\sqrt{2}}, \qquad a_2(\Omega) = \frac{a(\Omega) - a^\dagger(-\Omega)}{i\sqrt{2}}.$$

Note we have written $a_{\omega_0 \pm \Omega}$ as $a(\pm\Omega)$ and the same for b.

From these equations we see that we can write,

$$\begin{bmatrix} b_1(\Omega) \\ b_2(\Omega) \end{bmatrix} = \frac{1}{\sqrt{2}} \begin{bmatrix} 1 & 1 \\ -i & i \end{bmatrix} \begin{bmatrix} b(\Omega) \\ b^\dagger(-\Omega) \end{bmatrix} = \mathbb{U} \begin{bmatrix} b(\Omega) \\ b^\dagger(-\Omega) \end{bmatrix}, \tag{A.2}$$

and the same for a, where $\mathbb{U}$ is unitary ($\mathbb{U}\mathbb{U}^\dagger = \mathbb{U}^\dagger\mathbb{U} = \mathbb{I}$).

Note that $h(t) \in \mathbb{R} \implies h(\Omega) = h^\dagger(-\Omega)$, so we can write the matrix equation,

$$\begin{bmatrix} b(\Omega) \\ b^\dagger(-\Omega) \end{bmatrix} = \mathbb{M}_s(\Omega) \begin{bmatrix} a(\Omega) \\ a^\dagger(-\Omega) \end{bmatrix} + \vec{D}_s(\Omega)h(\Omega), \tag{A.3}$$

where,

$$\mathbb{M}_s(\Omega) = \begin{pmatrix} T_+(\Omega) & T_-(\Omega) \\ T_+^*(-\Omega) & T_-^*(-\Omega) \end{pmatrix}, \tag{A.4}$$

and

$$\vec{D}_s(\Omega) = \begin{pmatrix} G(\Omega) \\ G^*(-\Omega) \end{pmatrix}. \tag{A.5}$$

Therefore by using eq. (A.2) we can write,

$$\begin{aligned} \begin{bmatrix} b_1(\Omega) \\ b_2(\Omega) \end{bmatrix} = \mathbb{U} \begin{bmatrix} b(\Omega) \\ b^\dagger(-\Omega) \end{bmatrix} &= \mathbb{U}\mathbb{M}_s(\Omega) \begin{bmatrix} a(\Omega) \\ a^\dagger(-\Omega) \end{bmatrix} + \mathbb{U}\vec{D}_s(\Omega)h(\Omega) \\ &= \mathbb{U}\mathbb{M}_s(\Omega)\mathbb{U}^\dagger \begin{bmatrix} a_1(\Omega) \\ a_2(\Omega) \end{bmatrix} + \mathbb{U}\vec{D}_s(\Omega)h(\Omega). \end{aligned}$$

So we can identify,

$$\mathbb{M}_q(\Omega) = \mathbb{U}\mathbb{M}_s(\Omega)\mathbb{U}^\dagger, \tag{A.6}$$

$$\vec{D}_q(\Omega) = \mathbb{U}\vec{D}_s(\Omega). \tag{A.7}$$

Appendix B

Spectral density of Thermal Heat Bath Fluctuations

In this section we will derive the spectral density of the fluctuations of a heat bath. The result also applies to the thermal state of the optical field, which can be approximated as a vacuum when $\hbar\omega_0 \gg k_B T$ where ω_0 is the carrier frequency and T is the environmental temperature.

A heat bath can be modelled as a mixed state,

$$\{|n\rangle, P_n\} \tag{B.1}$$

whose statistics are determined by the Bose-Einstein distribution,

$$\langle n_\omega \rangle = \frac{1}{e^{\frac{\hbar\omega}{k_B T}} - 1} = \frac{1}{e^{\frac{\hbar(\omega_0+\Omega)}{k_B T}} - 1} \approx \frac{1}{e^{\frac{\hbar\omega_0}{k_B T}} - 1}. \tag{B.2}$$

where $\omega = \omega_0 + \Omega$ and assuming $\Omega \ll \omega_0$. T is the temperature of the heat bath and k_B is Boltzmann's constant.

We define annihilation operators for mode n and define continuous operators as in [18],

$$b^j_{\text{th}} \to b_{\text{th}\,\omega} = b_{\text{th}}(\Omega) = \sqrt{\frac{2\pi}{d\Omega}} b^j_{\text{th}}. \tag{B.3}$$

Therefore,

$$\langle n_\omega \rangle = \langle b_{\text{th}}^{\dagger\, j} b_{\text{th}}^{j} \rangle = \frac{d\Omega}{2\pi} \langle b_{\text{th}}^{\dagger}(\Omega) b_{\text{th}}(\Omega) \rangle$$
$$\implies \langle b_{\text{th}}^{\dagger}(\Omega) b_{\text{th}}(\Omega) \rangle = \frac{2\pi}{d\Omega} \frac{1}{e^{\frac{\hbar\omega_0}{k_B T}} - 1},$$

and since $d\Omega \approx 1/\delta(\Omega - \Omega)$ we can infer,

$$\langle b_{\text{th}}^{\dagger}(\Omega) b_{\text{th}}(\Omega') \rangle = 2\pi\delta(\Omega - \Omega') \frac{1}{e^{\frac{\hbar\omega_0}{k_B T}} - 1}. \tag{B.4}$$

Next using the commutation relation for $b_{\text{th}}(\Omega)$ and eq. (3.24) we can infer,

$$S_{b_{\text{th}} b_{\text{th}}} = 1 + \frac{2}{e^{\frac{\hbar\omega_0}{k_B T}} - 1}. \tag{B.5}$$

For a laser at room temperature $\hbar\omega_0 \gg k_B T$ and so,

$$S_{b_{\text{th}} b_{\text{th}}} \approx 1. \tag{B.6}$$

For a mechanical oscillator we write ω_0 as ω_m, the oscillator eigenfrequency, and we generally have $\hbar\omega_m \ll k_B T$ and so,

$$S_{b_{\text{th}} b_{\text{th}}} \approx \frac{2k_B T}{\hbar\omega_m} + 1. \tag{B.7}$$

Appendix C

Supplementary material for section. 5.1

C.1 Hamiltonian matrix in complex operator notation

In this section the expression for the internal Hamiltonian $\hat{H}$ shown in Eq. (5.14) will be transformed from the real-quadrature form in Ref. [8] to the complex ladder operator form.

The Hamiltonian in the real-quadrature form is given by

$$\hat{H} = \mathbf{x}_r^\dagger \Omega_r \mathbf{x}_r \,, \tag{C.1}$$

where $\mathbf{x}_r = (\hat{q}_1, \hat{p}_1; \ldots; \hat{q}_n, \hat{p}_n)^T$ are the real quadrature operators. The relation between Ω_r and the dynamical matrix A_r in the state-space model is given uniquely by,

$$\Omega_r = \frac{1}{4}\left(-\Theta A_r + A_r^\dagger \Theta\right), \tag{C.2}$$

where,

$$\Theta = \mathrm{diag}(\underbrace{\Theta_1, \ldots, \Theta_1}_{\text{n times}}) \in \mathbb{R}^{2n\times 2n}, \tag{C.3}$$

and,

$$\Theta_1 = \begin{bmatrix} 0 & 1 \\ -1 & 0 \end{bmatrix}. \tag{C.4}$$

The complex ladder operators are related to the real quadrature operators by $\mathbf{x} = (\hat{a}_1, \hat{a}_1^\dagger; \ldots; \hat{a}_n, \hat{a}_n^\dagger)^T = U\mathbf{x}_r$, where,

$$U = \mathrm{diag}(\underbrace{U_1, \ldots, U_1}_{\text{n times}}) \in \mathbb{C}^{2n\times 2n}, \tag{C.5}$$

where,

$$U_1 = \frac{1}{\sqrt{2}} \begin{bmatrix} 1 & i \\ 1 & -i \end{bmatrix}, \tag{C.6}$$

is the unitary transformation that converts from the real quadrature operators $(\hat{q}, \hat{p})$ to the complex ladder operators $(\hat{a}, \hat{a}^\dagger)$.

Note that we can write $\Theta = -iU^\dagger JU$, and that the relation between the dynamical matrix in the real quadrature picture and the complex ladder operators is given by $A = U^\dagger A_r U$, and recall that U is unitary. Substituting these facts into the expression for $\hat{H}$ we get $\hat{H} = \mathbf{x}^\dagger \Omega \mathbf{x}$ where,

$$\Omega = \frac{i}{4}\left(JA - A^\dagger J\right). \tag{C.7}$$

Where J is defined in the main text.

C.2 Relating the coupling rate to the single-pass squeezing factor

To compare the coupling rate $\sqrt{s_0\gamma}$ to the single-pass amplification factor r, we look at the degenerate case of the interaction Hamiltonian given in Eq. (20)

of the main text,

$$\hat{H}_{\rm deg} = -\hbar\sqrt{s_0\gamma/2}[(\hat{a}^\dagger)^2 + \hat{a}^2]. \tag{C.8}$$

Solving the equation of motion in the frequency domain, the resulting input-output relation for the amplitude quadrature $\hat{a}_1$ in the two-photon formalism [111, 112] is

$$\hat{a}_1^{\rm out}(\omega) = \frac{\gamma + \sqrt{s_0\gamma} + i\omega}{\gamma - \sqrt{s_0\gamma} - i\omega}\hat{a}_1^{\rm in}(\omega)\,. \tag{C.9}$$

We can derive the same input-output relation by propagating the continuum field through the cavity with a nonlinear crystal, and obtain

$$\hat{a}_1^{\rm out}(\omega) = \frac{-\sqrt{R} + e^{2r}e^{2i\omega L/c}}{1 - \sqrt{R}\,e^{2r}e^{2i\omega L/c}}\hat{a}_1^{\rm in}(\omega)\,. \tag{C.10}$$

Assuming $T \equiv 1 - R, r, \omega L/c \ll 1$, we can make the Taylor expansion of the above equation to the leading order of these small dimensionless quantities:

$$\hat{a}_1^{\rm out}(\omega) \approx \frac{T/2 + 2r + 2i\omega L/c}{T/2 - 2r - 2i\omega L/c}\hat{a}_1^{\rm in}(\omega)\,. \tag{C.11}$$

Eq. (C.9) and Eq. (C.11) become identical when

$$\gamma \equiv \frac{Tc}{4L}\,, \quad r = 2\sqrt{s_0\gamma}\,\frac{L}{c}\,, \tag{C.12}$$

which is the mapping used in the main text.

C.3 Including losses into the analysis

In this section, we show how the effect of optical loss is included in the analysis for the realistic implementation. The optical losses in the mirrors of both cavities will introduce quantum white noise vacuum processes [19, 57, 10],

$\hat{n}_a, \hat{n}_b$, which are coupled to modes $\hat{a}$ and $\hat{b}$ respectively via transmissivities T_a, T_b. This results in extra terms added to the Heisenberg equations of motion for the two modes,

$$\dot{\hat{b}} = -\gamma_b^\epsilon \hat{b} + \sqrt{2\gamma_b^\epsilon}\hat{n}_b + \frac{i}{\hbar}[\hat{H}_{\rm tot}, \hat{b}], \tag{C.13}$$

$$\dot{\hat{a}} = -\gamma_a^\epsilon \hat{a} + \sqrt{2\gamma_a^\epsilon}\hat{n}_a + \frac{i}{\hbar}[\hat{H}_{\rm tot}, \hat{a}], \tag{C.14}$$

where $H_{\rm tot}$ is the total Hamiltonian derived in the main text. The noise coupling constants for the $\hat{a}$ cavity and $\hat{b}$ cavity respectively are given by:

$$\gamma_a^\epsilon = \epsilon_a c/(4L_a)\,, \quad \gamma_b^\epsilon = \epsilon_b c/(4L_b), \tag{C.15}$$

where ϵ_a and ϵ_b are the optical losses described by cavity respectively. The loss from the non-linear crystal couples identically to the mirror loss into both cavities, and so can be included in ϵ_a, ϵ_b.

Solving the Heisenberg equations of motion in the frequency domain, we found that the noise contribution from the auxiliary cavity loss $\hat{n}_b$ is much smaller than the contribution from the $\hat{a}$ cavity loss $\hat{n}_a$ by a factor:

$$\frac{\omega^2 \gamma_b^\epsilon}{\gamma_{\rm neg}\gamma\gamma_a^\epsilon} \ll 1, \tag{C.16}$$

assuming $\gamma_a^\epsilon \approx \gamma_b^\epsilon$, and $\omega \ll \gamma_{\rm neg}$, $\omega \ll \gamma$, a result also found in the optomechanical case explored in [5], in which the filter cavity takes the role of the auxiliary cavity mode $\hat{b}$ and the mechanical oscillator takes the role of the main cavity mode $\hat{a}$. However in our case the main cavity loss is due to vacuum and is not thermally driven, and so is effectively at zero temperature. The phase noise due to the thermal fluctuation of the non-linear crystal [120] is negligible as there is almost no carrier power in either cavity.

C.4 Alternative topology

Here we show an alternative topology for the realisation shown in Fig. 5.2. The system consists of a linear coupled cavity. We call the cavity with the nonlinear crystal in it the active cavity and the other the passive cavity. The length of the passive cavity L_1 differs from the length L_2 of the active cavity so that they have different mode spacings. The two modes $\hat{a}$ and $\hat{b}$ in this case belong to the same longitudinal modes of the active cavity but separated by one free spectral range. The passive cavity acts as a compound mirror with frequency-dependent effective phase $\phi_{\text{eff}}(\omega)$ and transmissivity $T_{\text{eff}}(\omega)$, the former shifting the resonances of the active cavity by ω_a and ω_b for the $\hat{a}$ and $\hat{b}$, and the latter imparting different bandwidths for the two modes, denoted $\gamma_a = T_{\text{eff}}(\omega_a)c/(4L_2)$ and $\gamma_b = T_{\text{eff}}(\omega_b)c/(4L_2)$ respectively. The nonlinear crystal pump frequency is set to ω_p where $\omega_p/2$ is between the two modes $\hat{a}$ and $\hat{b}$. To make $\hat{b}$ satisfy the adiabatic condition, we require $\gamma_b \gg \omega$, while to ensure good performance we require $\gamma_a \ll \gamma_{\text{neg}}$. Both bandwidths can be independently controlled by changing the relative lengths of the two cavities.

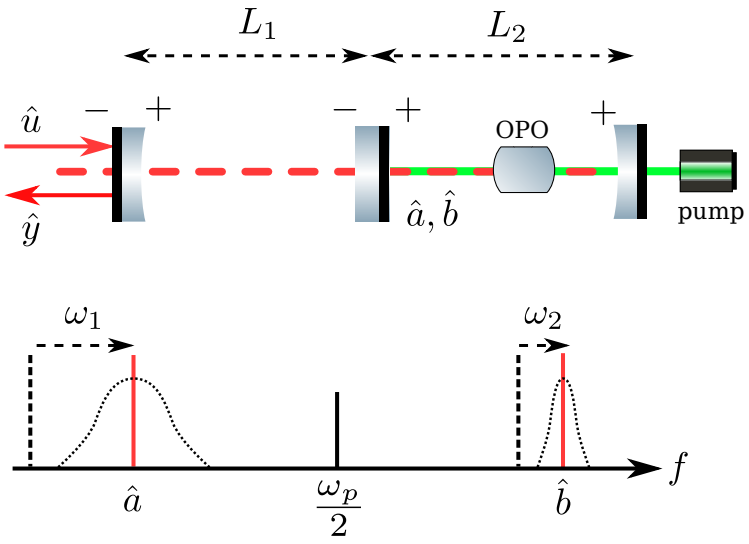

Figure C.1 Optical diagram and relevant frequencies of the alternative topology, consisting of a non-linear crystal and two linear cavities with the crystal in only one cavity.

Appendix D

$J - J$ unitary condition for quadrature operators

In this section we will derive the equivalent to Eq. (5.13) for the quadrature picture. The transformation for the transfer matrix is given by Eq. (A.6), so that the sideband picture transfer matrix is $\mathbf{G}(s) = \mathbf{U}^\dagger \mathbf{G}_q(s)\mathbf{U}$ where $\mathbf{U} = \mathrm{diag}(U_1, \ldots, U_1)$ is a block-diagonal matrix with,

$$U_1 = \frac{1}{\sqrt{2}} \begin{bmatrix} 1 & 1 \\ -i & i \end{bmatrix}, \tag{D.1}$$

and $\mathbf{G}_q(s)$ is the quadrature-picture transfer matrix.

The $J - J$ unitary condition then becomes,

$$\mathbf{G}^\dagger(s^*)J\mathbf{G}(-s) = J = \mathbf{U}^\dagger \mathbf{G}_q^\dagger(s^*)\mathbf{U}J\mathbf{U}^\dagger \mathbf{G}_q(-s)\mathbf{U}, \tag{D.2}$$

which we can write as,

$$\mathbf{G}_q^\dagger(s^*)\Theta\mathbf{G}_q(-s) = \Theta, \tag{D.3}$$

where $\Theta = \mathbf{U}J\mathbf{U}^\dagger$.

References

[1] P. Sikivie. "Experimental tests of the "invisible" axion". In: *Phys. Rev. Lett.* 51.16 (1983), pp. 1415–1417. ISSN: 00319007. URL: https://doi.org/10.1103/PhysRevLett.51.1415.

[2] William DeRocco and Anson Hook. "Axion interferometry". In: *Phys. Rev. D* 98.3 (2018), p. 35021. ISSN: 24700029. URL: https://doi.org/10.1103/PhysRevD.98.035021.

[3] LIGO Scientific Collaboration. "Advanced LIGO". In: *Class. Quantum Grav.* 32.7 (2015), p. 74001. URL: http://stacks.iop.org/0264-9381/32/i=7/a=074001.

[4] H. J. Kimble et al. "Conversion of conventional gravitational-wave interferometers into quantum nondemolition interferometers by modifying their input and/or output optics". In: *Phys. Rev. D* 65.2 (Dec. 2001), p. 022002. ISSN: 0556-2821. URL: http://dx.doi.org/10.1103/PhysRevD.65.022002.

[5] Haixing Miao et al. "Enhancing the Bandwidth of Gravitational-Wave Detectors with Unstable Optomechanical Filters". In: *Phys. Rev. Lett.* 115.21 (2015), p. 211104. ISSN: 10797114. URL: https://doi.org/10.1103/PhysRevLett.115.211104.

[6] Jocelyn S. Read et al. "Measuring the neutron star equation of state with gravitational wave observations". In: *Phys. Rev. D* 79.12 (2009), pp. 1–12. ISSN: 15507998. URL: https://doi.org/10.1103/PhysRevD.79.124033.

[7] A. Bauswein and H. T. Janka. "Measuring neutron-star properties via gravitational waves from neutron-star mergers". In: *Phys. Rev. Lett.* 108.1 (2012), pp. 1–5. ISSN: 00319007. URL: https://doi.org/10.1103/PhysRevLett.108.011101.

[8] Matthew R James, Hendra I Nurdin, and Ian R Petersen. "H^∞ control of linear quantum stochastic systems". In: *IEEE T. Automat. Contr.* 53.8 (2008), pp. 1787–1803. ISSN: 00189286. URL: https://ieeexplore.ieee.org/document/4625217.

[9] A. J. Shaiju and Ian R. Petersen. "A frequency domain condition for the physical realizability of linear quantum systems". In: *IEEE T. Automat. Contr.* 57.8 (2012), pp. 2033–2044. ISSN: 00189286. URL: https://doi.org/10.1109/TAC.2012.2195929.

[10] Hendra I. Nurdin, Matthew R. James, and Andrew C. Doherty. "Network Synthesis of Linear Dynamical Quantum Stochastic Systems". In: *SIAM J. Control. Optim.* 48.4 (Jan. 2009), pp. 2686–2718. ISSN: 0363-0129. URL: http://epubs.siam.org/doi/10.1137/080728652.

[11] D. F. Walls and Gerard J. Milburn. *Quantum Optics*. 2nd. Springer, 2008. ISBN: 9789004310087. URL: https://www.springer.com/gp/book/9783540285731.

[12] Franz Mandl and Graham Shaw. *Quantum Field Theory*. 2nd ed. Wiley, 2010.

[13] Haixing Miao. "Exploring Macroscoping Quantum Mechanics in Optomechanical Devices". PhD thesis. 2010.

[14] John Garrison and Raymond Chiao. *Quantum Optics*. Oxford: Oxford University Press, June 2008. ISBN: 9780198508861. URL: https://oxford.universitypressscholarship.com/view/10.1093/acprof:oso/9780198508861.001.0001/acprof-9780198508861.

[15] C. W. Gardiner and M. J. Collett. "Input and output in damped quantum systems: Quantum stochastic differential equations and the master equation". In: *Phys. Rev. A* 31.6 (1985), pp. 3761–3774. ISSN: 10502947. URL: https://doi.org/10.1103/PhysRevA.31.3761.

[16] K. R. Parthasarathy. *An Introduction to Quantum Stochastic Calculus*. Basel: Birkhäuser Basel, 1992. ISBN: 978-3-0348-9711-2. URL: http://link.springer.com/10.1007/978-3-0348-8641-3.

[17] Yanbei Chen. "Macroscopic quantum mechanics: Theory and experimental concepts of optomechanics". In: *J. Phys. B: At. Mol. Opt. Phys.*

46.10 (2013), p. 104001. ISSN: 09534075. URL: https://doi.org/10.1088/0953.

[18] K J Blow et al. "Continuum fields in quantum optics". In: *Phys. Rev. A* 42.7 (Oct. 1990), pp. 4102–4114. ISSN: 1050-2947. URL: https://link.aps.org/doi/10.1103/PhysRevA.42.4102.

[19] C. W. Gardiner and Peter Zoller. *Quantum Noise: A Handbook of Markovian and Non-Markovian Quantum Stochastic Methods with Applications to Quantum Optics*. Springer, 2004, p. 450. ISBN: 978-3-642-06094-6. URL: https://www.springer.com/gp/book/9783540223016.

[20] Alessandra Buonanno et al. "Laser-interferometer gravitational-wave optical-spring detectors". In: *Phys. Rev. D* 64.4 (2002), p. 42001. ISSN: 0556-2821. URL: https://arxiv.org/pdf/gr-qc/0201063.pdf.

[21] Alessandra Buonanno and Yanbei Chen. "Scaling law in signal recycled laser-interferometer gravitational-wave detectors". In: *Phys. Rev. D* 67.6 (2003). ISSN: 05562821. URL: https://journals.aps.org/prd/pdf/10.1103/PhysRevD.67.062002.

[22] Joe Bentley et al. "Converting the signal-recycling cavity into an unstable optomechanical filter to enhance the detection bandwidth of gravitational-wave detectors". In: *Phys. Rev. D* 99.10 (May 2019), p. 102001. ISSN: 2470-0010. URL: https://link.aps.org/doi/10.1103/PhysRevD.99.102001.

[23] J Mizuno. "Comparison of optical configurations for laser interferometric gravitational wave detectors". In: *Thesis* (1995). URL: http://www2.mpq.mpg.de/$%5Csim$ros/geo600_docu/text/theses/Jun_Mizuno.pdf.

[24] Mikhail Korobko et al. "Quantum expander for gravitational-wave observatories". In: *Light: Science and Applications* 8.1 (Dec. 2019), p. 118. ISSN: 2047-7538. URL: http://www.nature.com/articles/s41377-019-0230-2.

[25] B. P. Abbott, R. Abbott, T. D. Abbott, et al. "GWTC-1: A Gravitational-Wave Transient Catalog of Compact Binary Mergers Observed by LIGO and Virgo during the First and Second Observing Runs". In: *Physical Review X* 9.3 (Sept. 2019), p. 031040. ISSN: 2160-3308. URL: https://link.aps.org/doi/10.1103/PhysRevX.9.031040.

[26] A. Wicht et al. "White-light cavities, atomic phase coherence, and gravitational wave detectors". In: *Opt. Commun.* 134.1-6 (1997), pp. 431–439. ISSN: 00304018. URL: https://doi.org/10.1016/S0030-4018(96)00579-2.

[27] A. Wicht et al. "Experimental demonstration of negative dispersion without absorption". In: *Opt. Commun.* 179.1 (May 2000), pp. 107–115. ISSN: 00304018. URL: https://doi.org/10.1016/S0030-4018(99)00528-3.

[28] Stacy Wise et al. "Linewidth-broadened Fabry-Perot cavities within future gravitational wave detectors". In: *Class. Quantum Grav.* 21.5 (2004), S1031. ISSN: 02649381. URL: https://doi.org/10.1088/0264-9381/21/5/097.

[29] David Blair, Li Ju, Chun Nong Zhao, et al. *The next detectors for gravitational wave astronomy*. Dec. 2015. URL: https://doi.org/10.1007/s11433-015-5747-7.

[30] G S Pati et al. "Demonstration of a tunable-bandwidth white-light interferometer using anomalous dispersion in atomic vapor". In: *Phys. Rev. Lett.* 99.13 (2007), p. 133601. ISSN: 00319007. URL: https://doi.org/10.1103/PhysRevLett.99.133601.

[31] H N Yum et al. "Demonstration of white light cavity effect using stimulated Brillouin scattering in a fiber loop". In: *J. Lightwave Technol.* 31.23 (2013), p. 3865. URL: https://www.osapublishing.org/jlt/abstract.cfm?uri=jlt-31-23-3865.

[32] Minchuan Zhou, Zifan Zhou, and Selim M Shahriar. "Quantum noise limits in white-light-cavity-enhanced gravitational wave detectors". In: *Phys. Rev. D* 92.8 (Oct. 2015), p. 082002. ISSN: 1550-7998. URL: https://link.aps.org/doi/10.1103/PhysRevD.92.082002.

[33] Yiqiu Ma et al. "Quantum noise of a white-light cavity using a double-pumped gain medium". In: *Phys. Rev. A* 92.2 (Aug. 2015), p. 023807. ISSN: 10941622. URL: https://link.aps.org/doi/10.1103/PhysRevA.92.023807.

[34] Minchuan Zhou and Selim M Shahriar. "Optomechanical resonator as a negative dispersion medium for enhancing the sensitivity bandwidth in a gravitational-wave detector". In: *Phys. Rev. D* 98.2 (2018), p. 22003. ISSN: 2470-0029. URL: https://doi.org/10.1103/PhysRevD.98.022003.

[35] Robert W. Boyd. *Nonlinear Optics*. Third. Elsevier, 1992, p. 620. ISBN: 9780121216801. URL: http://www.fulviofrisone.com/attachments/article/404/Boyd.

[36] Haixing Miao. "General quantum constraints on detector noise in continuous linear measurement". In: (2017). URL: https://arxiv.org/pdf/1605.02312.pdf.

[37] André Thüring, Harald Lück, and Karsten Danzmann. "Analysis of a four-mirror-cavity enhanced Michelson interferometer". In: *Physical Review E - Statistical, Nonlinear, and Soft Matter Physics* 72.6 (2005). ISSN: 15393755. URL: https://journals.aps.org/pre/pdf/10.1103/PhysRevE.72.066615.

[38] André Thüring et al. "Detuned Twin-Signal-Recycling for ultrahigh-precision interferometers". In: *Optics Letters* 32.8 (2007), p. 985. ISSN: 0146-9592. URL: https://arxiv.org/pdf/0707.0413.pdf.

[39] C. M. Caves and B. L. Schumaker. "New formalism for two-photon quantum optics. I - Quadrature phases and squeezed states. II - Mathematical foundation and compact notation". In: *Phys. Rev. A* 31 (1985), pp. 3068–3111.

[40] A. A. Clerk et al. "Introduction to quantum noise, measurement, and amplification". In: *Rev. Mod. Phys.* 82.2 (2010), pp. 1155–1208. ISSN: 00346861. URL: https://doi.org/10.1103/RevModPhys.82.1155.

[41] Markus Aspelmeyer, Tobias J. Kippenberg, and Florian Marquardt. "Cavity optomechanics". In: *Rev. Mod. Phys.* 86.4 (2014), pp. 1391–1452. ISSN: 15390756. URL: https://doi.org/10.1103/RevModPhys.86.1391.

[42] V B Braginsky and F.Ya. Khalilli. *Quantum Measurement*. Cambridge University Press, 1992. URL: http://www.cambridge.org/us/academic/subjects/physics/quantum-physics-quantum-information-and-quantum-computation/quantum-measurement.

[43] Thomas Corbitt et al. "An all-optical trap for a gram-scale mirror". In: *Phys. Rev. Lett.* 98.15 (2007). ISSN: 00319007. URL: https://arxiv.org/pdf/quant-ph/0612188.pdf.

[44] D. E. Chang et al. "Ultrahigh-Q mechanical oscillators through optical trapping". In: *New Journal of Physics* 14 (2012). ISSN: 13672630. URL: http://www.njp.org/.

[45] K. K. Ni et al. "Enhancement of mechanical Q factors by optical trapping". In: *Phys. Rev. Lett.* 108.21 (May 2012), p. 214302. ISSN: 00319007. URL: https://doi.org/10.1103/PhysRevLett.108.214302.

[46] W. Zach Korth et al. "Suppression of quantum-radiation-pressure noise in an optical spring". In: *Phys. Rev. A* 88.3 (Sept. 2013), p. 033805. ISSN: 10502947. URL: https://doi.org/10.1103/PhysRevA.88.033805.

[47] Christoph Reinhardt et al. "Ultralow-noise SiN trampoline resonators for sensing and optomechanics". In: *Physical Review X* 6.2 (Apr. 2016), p. 021001. ISSN: 21603308. URL: https://doi.org/10.1103/PhysRevX.6.021001.

[48] Dongyu Chen et al. "On-Chip Ultra-High-Q Silicon Oxynitride Optical Resonators". In: *ACS Photonics* 4.9 (Sept. 2017), pp. 2376–2381. ISSN: 23304022. URL: https://doi.org/10.1021/acsphotonics.7b00752.

[49] Y. Tsaturyan et al. "Ultracoherent nanomechanical resonators via soft clamping and dissipation dilution". In: *Nature Nanotechnology* 12.8 (2017), pp. 776–783. ISSN: 17483395. URL: https://doi.org/10.1038/nnano.2017.101.

[50] Massimiliano Rossi et al. "Measurement-based quantum control of mechanical motion". In: *Nature* 563.7729 (2018), pp. 53–58. ISSN: 14764687. URL: http://dx.doi.org/10.1038/s41586-018-0643-8.

[51] Michael Page et al. "Ultra-low dissipation resonators for improving the sensitivity of gravitational wave detectors". In: *Physics Letters, Section A: General, Atomic and Solid State Physics* 382.33 (Aug. 2018), pp. 2174–2180. ISSN: 03759601. URL: https://doi.org/10.1016/j.physleta.2017.06.031.

[52] Michael Page et al. "Enhanced detection of high frequency gravitational waves using optically diluted optomechanical filters". In: *Phys. Rev. D* 97.12 (2018), p. 124060. ISSN: 24700029. URL: https://doi.org/10.1103/PhysRevD.97.124060.

[53] John Bechhoefer. "Feedback for physicists: A tutorial essay on control". In: *Rev. Mod. Phys.* 77.3 (Aug. 2005), pp. 783–836. ISSN: 00346861. URL: https://link.aps.org/doi/10.1103/RevModPhys.77.783.

[54] James Ward Brown and Ruel V. Churchill. *Complex variables and applications*. 9th ed. McGraw-Hill Education, 2013. ISBN: 0073383171.

[55] Henning Rehbein et al. "Double optical spring enhancement for gravitational-wave detectors". In: *Phys. Rev. D* 78.6 (2008), pp. 1–11. ISSN: 15507998. URL: https://doi.org/10.1103/PhysRevD.78.062003.

[56] Joe Bentley et al. "Direct approach to realizing quantum filters for high-precision measurements". In: *Phys. Rev. A* 103.1 (Jan. 2021), p. 013707. ISSN: 2469-9926. URL: https://link.aps.org/doi/10.1103/PhysRevA.103.013707.

[57] Vladimir B Braginsky and Farid Ya Khalili. *Quantum Measurement*. Ed. by Kip S. Thorne. Cambridge: Cambridge University Press, 1992. ISBN: 9780511622748. URL: http://ebooks.cambridge.org/ref/id/CBO9780511622748.

[58] Carlton M. Caves. "Quantum-Mechanical Radiation-Pressure Fluctuations in an Interferometer". In: *Phys. Rev. Lett.* 45.2 (July 1980), pp. 75–79. ISSN: 0031-9007. URL: https://link.aps.org/doi/10.1103/PhysRevLett.45.75.

[59] Rana X. Adhikari. "Gravitational radiation detection with laser interferometry". In: *Rev. Mod. Phys.* 86.1 (Feb. 2014), pp. 121–151. ISSN: 15390756. URL: https://link.aps.org/doi/10.1103/RevModPhys.86.121.

[60] Haixing Miao, Huan Yang, and Denis Martynov. "Towards the design of gravitational-wave detectors for probing neutron-star physics". In: *Phys. Rev. D* 98.4 (Aug. 2018), p. 044044. ISSN: 2470-0010. URL: https://link.aps.org/doi/10.1103/PhysRevD.98.044044.

[61] Hideo Mabuchi. "Coherent-feedback quantum control with a dynamic compensator". In: *Phys. Rev. A* 78.3 (Sept. 2008), p. 032323. ISSN: 10502947. URL: https://link.aps.org/doi/10.1103/PhysRevA.78.032323.

[62] Ryan Hamerly and Hideo Mabuchi. "Advantages of coherent feedback for cooling quantum oscillators". In: *Phys. Rev. Lett.* 109.17 (2012),

p. 173602. ISSN: 00319007. URL: https://doi.org/10.1103/PhysRevLett.109.173602.

[63] Kurt Jacobs, Xiaoting Wang, and Howard M. Wiseman. "Coherent feedback that beats all measurement-based feedback protocols". In: *New Journal of Physics* 16 (2014). ISSN: 13672630. URL: https://doi.org/10.1088/1367-2630/16/7/073036.

[64] Eric Oelker et al. "Audio-Band Frequency-Dependent Squeezing for Gravitational-Wave Detectors". In: *Phys. Rev. Lett.* 116.4 (Jan. 2016), p. 041102. ISSN: 10797114. URL: https://link.aps.org/doi/10.1103/PhysRevLett.116.041102.

[65] Roman Schnabel. *Squeezed states of light and their applications in laser interferometers*. 2017. URL: http://dx.doi.org/10.1016/j.physrep.2017.04.001.

[66] J. E. Gough, M. R. James, and H. I. Nurdin. "Squeezing components in linear quantum feedback networks". In: *Phys. Rev. A* 81.2 (June 2010), p. 023804. ISSN: 10502947. URL: http://dx.doi.org/10.1103/PhysRevA.81.023804.

[67] Hendra I Nurdin and Naoki Yamamoto. *Linear Dynamical Quantum Systems: Analysis, Synthesis, and Control*. Springer, 2017. ISBN: 978-3-319-55199-9. URL: http://link.springer.com/10.1007/978-3-319-55201-9.

[68] John Gough and Matthew R. James. "The series product and its application to quantum feedforward and feedback networks". In: *IEEE T. Automat. Contr.* 54.11 (June 2009), pp. 2530–2544. ISSN: 00189286. URL: http://arxiv.org/abs/0707.0048.

[69] J. Gough and M. R. James. "Quantum feedback networks: Hamiltonian formulation". In: *Comm. Math. Phys.* 287.3 (2009), pp. 1109–1132. ISSN: 00103616. URL: https://doi.org/10.1007/s00220-008-0698-8.

[70] Nikolas Tezak et al. "Specification of photonic circuits using quantum hardware description language". In: *Philos. T. R. Soc. A* 370.1979 (2012), pp. 5270–5290. ISSN: 1364503X. URL: https://doi.org/10.1098/rsta.2011.0526.

[71] Joshua Combes, Joseph Kerckhoff, and Mohan Sarovar. "The SLH framework for modeling quantum input-output networks". In: *Advances in Physics: X* 2.3 (May 2017), pp. 784–888. ISSN: 2374-6149. URL: http://dx.doi.org/10.1080/23746149.2017.1343097.

[72] Hendra Ishwara Nurdin. "On synthesis of linear quantum stochastic systems by pure cascading". In: *IEEE T. Automat. Contr.* 55.10 (2010), pp. 2439–2444. ISSN: 00189286. URL: https://doi.org/10.1109/TAC.2010.2062892.

[73] H.I. Nurdin. "Synthesis of Linear Quantum Stochastic Systems via Quantum Feedback Networks". In: *IEEE T. Automat. Contr.* 55.4 (Apr. 2010), pp. 1008–1013. ISSN: 0018-9286. URL: http://ieeexplore.ieee.org/document/5404766/.

[74] Hendra I. Nurdin, Symeon Grivopoulos, and Ian R. Petersen. "The transfer function of generic linear quantum stochastic systems has a pure cascade realization". In: *Automatica* 69 (2016), pp. 324–333. ISSN: 00051098. URL: https://doi.org/10.1016/j.automatica.2016.03.002.

[75] Symeon Grivopoulos, Hendra I. Nurdin, and Ian R. Petersen. "On transfer function realizations for Linear Quantum Stochastic Systems". In: *IEEE Decis. Contr. P.* 110100020.Cdc (2016), pp. 4552–4558. URL: https://doi.org/10.1109/CDC.2016.7798962.

[76] Symeon Grivopoulos and Ian Petersen. "Linear Quantum System Transfer Function Realization Using Static Networks for Input/Output Processing and Feedback". In: *SIAM J. Control. Optim.* 55.5 (Jan. 2017), pp. 3349–3369. ISSN: 0363-0129. URL: https://epubs.siam.org/doi/10.1137/15M104829X.

[77] Ian R. Petersen et al. "A Systems Theory Approach to the Synthesis of Minimum Noise Phase-Insensitive Quantum Amplifiers". In: *E. C. C.* Feb. 2018, pp. 3185–3190. ISBN: 9783952426982. URL: http://arxiv.org/abs/1802.03887.

[78] D. Luenberger. "Canonical forms for linear multivariable systems". In: *IEEE T. Automat. Contr.* 12.3 (June 1967), pp. 290–293. ISSN: 0018-9286. URL: http://ieeexplore.ieee.org/document/1098584/.

[79] J.E. Ackermann and R.S. Bucy. "Canonical minimal realization of a matrix of impulse response sequences". In: *Inform. Control* 19.3 (Oct.

1971), pp. 224–231. ISSN: 00199958. URL: https://linkinghub.elsevier.com/retrieve/pii/S0019995871901057.

[80] Thomas Kailath. *Linear Systems*. 1st ed. Prentice-Hall, Inc., 1980, p. 31. ISBN: 9780135369616. URL: https://books.google.co.uk/books/about/Linear_Systems.html?id=ggYqAQAAMAAJ.

[81] G. E. Antoniou, P. N. Paraskevopoulos, and S. J. Varoufakis. "Minimal State-Space Realization of Factorable 2-D Transfer Functions". In: *IEEE T. Circuits Syst.* 35.8 (1988), pp. 1055–1058. ISSN: 00984094. URL: https://doi.org/10.1109/31.1857.

[82] R L Hudson and K R Parthasarathy. "Quantum Ito's formula and stochastic evolutions". In: *Comm. Math. Phys.* 93.3 (1984), pp. 301–323. ISSN: 00103616. URL: https://projecteuclid.org/download/pdf_1/euclid.cmp/1103941122.

[83] Luc Bouten, Ramon Van Handel, and Matthew R. James. "An Introduction to Quantum Filtering". In: *SIAM J. Control. Optim.* 46.6 (Jan. 2007), pp. 2199–2241. ISSN: 0363-0129. URL: http://arxiv.org/abs/math/0601741.

[84] M. Müller et al. "Parametric dispersion in electromagnetically induced transparency". In: *Phys. Rev. A* 62.6 (2000), 060501(R). ISSN: 10502947. URL: https://doi.org/10.1103/PhysRevA.62.060501.

[85] Blair David, J U Li, Zhao Chunnong, et al. "The next detectors for gravitational wave astronomy". In: *Sci. China Phys. Mech.* 58.12 (2015), p. 120405. URL: http://engine.scichina.com/publisher/scp/journal/SCPMA/58/12/10.1007/s11433-015-5747-7?slug=abstract.

[86] Michael A Page et al. "Gravitational wave detectors with broadband high frequency sensitivity". In: *LIGO DCC* (2019).

[87] Rion Shimazu and Naoki Yamamoto. "Quantum functionalities via feedback amplification". In: *arXiv:1909.12822 [quant-ph]* (Sept. 2019). URL: http://arxiv.org/abs/1909.12822.

[88] R. de L. Kronig. "On the Theory of Dispersion of X-Rays". In: *J. Opt. Soc. Am.* 12.6 (June 1926), p. 547. ISSN: 0030-3941. URL: https://link.aps.org/doi/10.1103/PhysRev.49.332.

[89] John S. Toll. "Causality and the Dispersion Relation: Logical Foundations". In: *Physical Review* 104.6 (Dec. 1956), pp. 1760–1770. ISSN: 0031-899X. URL: https://link.aps.org/doi/10.1103/PhysRev.104.1760.

[90] John Doyle, Bruce Francis, and Allen Tannenbaum. *Feedback Control Theory*. 1st ed. Macmillan Publishing Co., 1990. Chap. 6. URL: http://link.springer.com/10.1007/978-3-319-07275-3_1.

[91] Bryan Hirschorn and Mark E. Orazem. "On the sensitivity of the kramers-kronig relations to nonlinear effects in impedance measurements". In: *J. Electrochem. Soc.* 156.10 (2009), pp. 345–351. ISSN: 00134651. URL: https://doi.org/10.1149/1.3190160.

[92] T. Isogai et al. "Loss in long-storage-time optical cavities". In: *Opt. Express* 21.24 (Dec. 2013), p. 30114. ISSN: 1094-4087. URL: https://www.osapublishing.org/oe/abstract.cfm?uri=oe-21-24-30114.

[93] Eric Oelker et al. "Audio-Band Frequency-Dependent Squeezing for Gravitational-Wave Detectors". In: *Phys. Rev. Lett.* 116.4 (Jan. 2016), p. 041102. ISSN: 0031-9007. URL: http://dx.doi.org/10.1103/PhysRevLett.116.041102.

[94] C.W. Helstrom. "Minimum mean-squared error of estimates in quantum statistics". In: *Physics Letters A* 25.2 (July 1967), pp. 101–102. ISSN: 0375-9601. URL: https://www.sciencedirect.com/science/article/pii/0375960167903660?via%3Dihub.

[95] Alexander Holevo. *Probabilistic and Statistical Aspects of quantum theory*. 2nd. Scuola Normale Superiore, 2011. ISBN: 9788876423758. URL: https://doi.org/10.1007/978-88-7642-378-9.

[96] Samuel L Braunstein, Carlton M Caves, and G J Milburn. "Generalized Uncertainty Relations: Theory, Examples, and Lorentz Invariance". In: *Annals of Physics* 247.0040 (1996), pp. 135–173. ISSN: 00034916. URL: http://linkinghub.elsevier.com/retrieve/pii/S0003491696900408.

[97] V Giovannetti, S Lloyd, and L Maccone. "Advances in quantum metrology". In: *Nat. Photonics* 5.4 (2011), pp. 222–229. ISSN: 1749-4885. URL: http://www.nature.com/doifinder/10.1038/nphoton.2011.35.

[98] Mankei Tsang, Howard M Wiseman, and Carlton M Caves. "Fundamental quantum limit to waveform estimation". In: *Phys. Rev. Lett.*

106 (2011), p. 90401. URL: http://journals.aps.org/prl/abstract/10.1103/PhysRevLett.106.090401.

[99] Haixing Miao et al. "Towards the Fundamental Quantum Limit of Linear Measurements of Classical Signals". In: *Phys. Rev. Lett.* 119.5 (2017), p. 050801. ISSN: 10797114. URL: https://arxiv.org/pdf/1608.00766.pdf.

[100] James P. Millan. *State-Space Canonical Forms*. URL: https://www.engr.mun.ca/$%5Csim$millan/Eng6825/canonicals.pdf.

[101] Vladimir B. Braginsky. "Energetic quantum limit in large-scale interferometers". In: *AIP Conference Proceedings*. Vol. 523. 10. AIP, 2000, pp. 180–190. ISBN: 0094-243X 1-56396-944-0. URL: https://doi.org/10.1063/1.1291855.

[102] Mankei Tsang, Howard M Wiseman, and Carlton M Caves. "Fundamental quantum limit to waveform estimation". In: *Phys. Rev. Lett.* 106.9 (2011). ISSN: 00319007. URL: https://journals.aps.org/prl/pdf/10.1103/PhysRevLett.106.090401.

[103] Haixing Miao, Nicolas D. Smith, and Matthew Evans. "Quantum Limit for Laser Interferometric Gravitational-Wave Detectors from Optical Dissipation". In: *Physical Review X* 9.2 (2019), p. 11053. ISSN: 21603308. URL: https://doi.org/10.1103/PhysRevX.9.011053.

[104] Marcin Zwierz, Carlos A. Pérez-Delgado, and Pieter Kok. "Ultimate limits to quantum metrology and the meaning of the Heisenberg limit". In: *Phys. Rev. A* 85.4 (2012), pp. 1–8. ISSN: 10502947. URL: https://doi.org/10.1103/PhysRevA.85.042112.

[105] Shakib Daryanoosh et al. "Experimental optical phase measurement approaching the exact Heisenberg limit". In: *Nature Communications* 9.1 (2018), pp. 1–6. ISSN: 20411723. URL: http://dx.doi.org/10.1038/s41467-018-06601-7.

[106] D. V. Tsarev et al. "Quantum metrology beyond Heisenberg limit with entangled matter wave solitons". In: *arXiv* 26.15 (2018), pp. 19583–19595. ISSN: 1094-4087. URL: https://doi.org/10.1364/oe.26.019583.

[107] Jiahao Huang et al. "Achieving Heisenberg-limited metrology with spin cat states via interaction-based readout". In: *Phys. Rev. A* 98.1 (2018),

pp. 1–11. ISSN: 24699934. URL: https://doi.org/10.1103/PhysRevA.98.012129.

[108] Sisi Zhou et al. "Achieving the Heisenberg limit in quantum metrology using quantum error correction". In: *Nature Communications* 9.1 (2018). ISSN: 20411723. URL: http://dx.doi.org/10.1038/s41467-017-02510-3.

[109] M Korobko et al. "Beating the Standard Sensitivity-Bandwidth Limit of Cavity-Enhanced Interferometers with Internal Squeezed-Light Generation". In: *Phys. Rev. Lett.* 118.14 (2017). ISSN: 10797114. URL: https://arxiv.org/pdf/1702.01044.pdf.

[110] Mikhail Korobko et al. "Quantum expander for gravitational-wave observatories". In: *Light: Science and Applications* 8.1 (2019), pp. 2047–7538. ISSN: 20477538. URL: www.nature.com/lsa.

[111] Carlton M. Caves and Bonny L. Schumaker. "New formalism for two-photon quantum optics. I. Quadrature phases and squeezed states". In: *Phys. Rev. A* 31.5 (1985), pp. 3068–3092. ISSN: 10502947. URL: https://doi.org/10.1103/PhysRevA.31.3068.

[112] Bonny L. Schumaker and Carlton M. Caves. "New formalism for two-photon quantum optics. II. Mathematical foundation and compact notation". In: *Phys. Rev. A* 31.5 (1985), pp. 3093–3111. ISSN: 10502947. URL: https://doi.org/10.1103/PhysRevA.31.3093.

[113] Xiang Li et al. "Broadband sensitivity improvement via coherent quantum feedback with PT symmetry". In: *In preparation* (Dec. 2020), pp. 1–6. URL: http://arxiv.org/abs/2012.00836.

[114] Mankei Tsang and Carlton M. Caves. "Evading quantum mechanics: Engineering a classical subsystem within a quantum environment". In: *Physical Review X* 2.3 (2012), pp. 1–7. ISSN: 21603308. URL: https://doi.org/10.1103/PhysRevX.2.031016.

[115] Naoki Yamamoto. "Decoherence-free linear quantum subsystems". In: *IEEE T. Automat. Contr.* 59.7 (2014), pp. 1845–1857. ISSN: 00189286. URL: https://doi.org/10.1109/TAC.2014.2313218.

[116] Carl M. Bender. "Introduction to PT-symmetric quantum theory". In: *Contemporary Physics* 46.4 (2005), pp. 277–292. ISSN: 00107514. URL: https://doi.org/10.1080/00107500072632.

[117] Joe Bentley et al. "Designing Heisenberg-limited linear detectors—a bottom-up approach". In: *In preparation* (2021).

[118] Christina E. Vollmer et al. "Quantum Up-Conversion of Squeezed Vacuum States from 1550 to 532 nm". In: *Phys. Rev. Lett.* 112.7 (Feb. 2014), p. 073602. ISSN: 0031-9007. URL: https://link.aps.org/doi/10.1103/PhysRevLett.112.073602.

[119] Chong Chen, Liang Jin, and Ren Bao Liu. "Sensitivity of parameter estimation near the exceptional point of a non-Hermitian system". In: *New Journal of Physics* 21.8 (2019). ISSN: 13672630. URL: https://doi.org/10.1088/1367-2630/ab32ab.

[120] J. E.S. César et al. "Extra phase noise from thermal fluctuations in nonlinear optical crystals". In: *Phys. Rev. A* 79.6 (2009), p. 063816. ISSN: 10502947. URL: https://doi.org/10.1103/PhysRevA.79.063816.